

UNIVERSITY OF OKLAHOMA

GRADUATE COLLEGE

DEVELOPMENT AND CHARACTERIZATION OF A LAYER BY  
LAYER ULTRASOUND ASSISTED SPRAY DEPOSITION PROCESS  
FOR THIN POLYMER FILMS

A DISSERTATION

SUBMITTED TO THE ADVISORY COMMITTEE

In partial fulfillment of the requirements for the

Degree of

Doctor of Philosophy

By

ANANDH BALAKRISHNAN

Norman, Oklahoma

2012

DEVELOPMENT AND CHARACTERIZATION OF A LAYER BY  
LAYER ULTRASOUND ASSISTED SPRAY DEPOSITION PROCESS  
FOR THIN POLYMER FILMS

A DISSERTATION APPROVED FOR THE SCHOOL OF AEROSPACE AND  
MECHANICAL ENGINEERING

BY

---

Chair, Dr. Mrinal C. Saha

---

Dr. M. Cengiz Altan

---

Dr. James D. Baldwin

---

Dr. Zahed Siddique

---

Dr. Brian P. Grady

© Copyright by ANANDH BALAKRISHNAN 2012

All Rights Reserved.

Dedicated

To

My parents, sister and her family, my lovely girl-friend Julia and her family and our loving pet animals: Rufus I, Rufus II (dogs), Orangie, Luna, Hermy, Mia, Niobe, Baby, Cuji and Herbert (cats), Clementine (Guinea Pig)

## ACKNOWLEDGEMENT

Throughout the course of this work, I have been inspired by a variety of people, some of them my superiors and some of them my own students in the various classes that I have helped teach. I sincerely thank all of these numerous people for giving me the chance to be involved in their educational pursuits. I thank all of the professors that I have come to know and admire during the course of my work including Dr. Baldwin, Dr. Altan, Dr. Grady, Dr. Madden and Dr. Siddique.

My major advisor Dr. Saha has touched my life in more ways than one. His message of doing innovative and useful work has always resonated with my own ambitions of contributing to the advancement of the scientific method. I appreciate his mode of functioning where he gave me sufficient freedom to pursue a research topic of interest. I also thank him for unrelenting financial support throughout my degree program.

Of special mention are Dr. Grady and his research group at the school of Chemical, Biological and Materials Engineering. His inspiring leadership during the latter stages of this work has improved the general quality of my work. His tireless help with the DSC, X-ray scattering measurements have added credibility to this work. Also to be mentioned is Dr. Madden from the school of geology and geophysics whose guidance/training with AFM measurements were critical for the successful imaging of all of my samples.

Last but not the least; I thank the A-team of the AME machine shop: Mr. Billy Mays and Mr. Gregory Williams for all their help and moral support throughout the course of my work. Special thanks are also due to Mr. Jim Cornell of the glass-shop for all help with the design and fabrication of my experimental set-up. I also express my gratitude to all

of my lab mates specifically Mr. Bipul Barua (senior Ph.D candidate with Dr.Saha) and Mr. Marcus Hart (now with Boeing, Seattle) for the periodic morale boosters and pep talks.

Finally, I couldn't have done any of this without the quiet moral support of my parents Mr and Mrs S. Balakrishnan, my sister and my brother-in-law Jayanthi and S. Narayanan and my girlfriend Julia and her family. My parents poured every drop of their hard earned savings into helping me become an accomplished engineer. My sister and her husband have both been model human beings and have done exceptionally well to help me with my work. Julia has given so much of moral input for me to work hard and be focused. She has looked after my mental wellbeing for the duration of the degree. She has proven to me that life exists outside of the lab and academic pursuits. To her I owe my sanity and cultural happiness. All those wonderful walks, hikes and nature pursuits have given me the chance to recharge my soul for improving the quality of my work. She has given me something to look forward to in life.

## Table of Contents

ACKNOWLEDGEMENT .....	iv
TABLE OF CONTENTS .....	vi
LIST OF TABLES .....	xi
LIST OF FIGURES .....	xii
ABSTRACT .....	xix
<b>1. INTRODUCTION</b> .....	<b>1</b>
1.1 Film Process Methods.....	1
1.2 Film Applications.....	6
1.3 Scope of the Work .....	13
<b>2. ULTRASONIC NOZZLES AND ULTRASONIC ATOMIZATION</b> .....	<b>15</b>
2.1 Motivation for Ultrasonic Atomization and its Recent Applications .....	15
2.2 Thin Polymer Film Fabrication via UA .....	19
2.3 Nozzle Fundamentals, Geometries and Parameters.....	23
2.4 Definitions, Mechanisms and Droplet Characteristics.....	31
2.5 Influence of Liquid Physicochemical Properties on Ultrasonic Atomization.....	39
2.6 Deposition Parameters of Interest as Applied to Thin Polymer Films .....	40

2.7 Practical Implementation of a Deposition System .....	41
2.8 Key Research Questions-I.....	42
2.8.1 How Do The Independent Variables Affect Droplet Formation and What Is The Relationship Between These Variables And The Final Droplet Diameter? .....	42
2.8.2 Was There A Distribution In The Droplets That Were Generated And If These Distributions Were Solution Weight Percent Dependent? .....	43
2.8.3 How Can One Obtain Uniform Thin Polyurethane Films Via an Efficient UA Whilst Also Reducing Process Time, Obtaining Energy/Material Savings? .....	43
2.8.4 Which Independent Variable/Sets of Independent Variables Affect The Microstructure/Properties The Most And Why/Why Not? .....	44
<b>3. THERMOPLASTIC POLYURETHANES (TPU) .....</b>	<b>45</b>
3.1 Basic Terminology, Definitions and Fundamental Chemical Structures.....	45
3.2 TPU Material Mechanical Behavior and Microstructural States of Hard/Soft Domains .....	47
3.3 Critical TPU Applications.....	50
3.4 Key Research Questions-II .....	51
3.4.1 Do The Capillary Waves Travelling Through The Polymer Solution Influence the Useful Final Mechanical Properties Of The Films? Why? / Why Not? .....	51



3.4.2 What Was The State Of The H/S Phases In The Material As F (Processing Conditions)? And Do These Trends Match With The Trends In The Mechanical Properties? Why? / Why Not? .....	52
--	----

**4. MATERIALS AND METHODS .....53**

4.1 Materials Used .....	53
--------------------------	----

4.1.1 Polymer System .....	53
----------------------------	----

4.1.2 Solvents Used.....	53
--------------------------	----

4.2 Polymer Solution Preparation and Solution Properties .....	53
--	----

4.2.1 Solution Preparation.....	53
---------------------------------	----

4.2.2 Solution Properties.....	54
--------------------------------	----

4.2.2.1 Density Measurement.....	54
----------------------------------	----

4.2.2.2 Viscosity Measurement .....	54
-------------------------------------	----

4.2.2.3 Surface Tension Measurement .....	55
---	----

4.3 Thin Film Fabrication.....	55
--------------------------------	----

4.3.1 Control Films .....	55
---------------------------	----

4.3.2 Ultrasound Atomized Films: Set-Up and Spray Characterization, Film Fabrication Protocols.....	58
--	----

4.3.2.1 Set-Up and Spray Characterization.....	58
--	----

4.3.2.2 Film Fabrication Protocols.....	63
---	----

4.4 Solvent Drying Measurements.....	64
4.5 Tensile Mechanical Testing.....	65
4.6 Optical Microstructure Characterization.....	66
4.7 Differential Scanning Calorimetry (DSC).....	66
4.8 Small Angle/ Wide Angle X-Ray Scattering (SAXS/WAXS).....	69
4.9 Atomic Force Microscopy (AFM).....	70
4.10 Rationale and Scope of Work: Design of Experiments.....	71
<b>5. THIN FILM PROCESS CHARACTERIZATION.....</b>	<b>76</b>
5.1 Film Deposition Optimization.....	76
5.1.1 Initial Results: THF Based Films.....	76
5.1.2 Transition to DMAC as Solvent.....	76
5.1.3 Regulated Flow with DMAC as Solvent.....	78
5.1.4 Air-Draft Attachment Implementation.....	78
5.1.5 Role of Air-Draft in Film Formation.....	81
5.2 Spray Droplet Data.....	84
5.2.1 Spray Patterns as f (flow rate, draft pressure).....	84
5.2.2 Effect of Varying the Liquid to Air Ratio.....	85
5.2.3 Apparent Droplet Diameter Distributions.....	88

5.2.4 Median Droplet Diameter Trends: Influence of Physicochemical Properties and Solution Flow Rate .....	93
5.3 Solution Volume Determination and Thickness Trends .....	98
5.4 Film Drying and Gravimetric Analysis.....	98
5.4.1 THF Films .....	98
5.4.2 DMAC Films .....	102
5.5 Optical Microstructures .....	102
<b>6. THIN FILM MATERIAL CHARACTERIZATION .....</b>	<b>111</b>
6.1 Mechanical Test Results .....	111
6.1.1 Cast THF Films.....	111
6.1.2 Cast and Atomized DMAC/Atomized THF Films .....	114
6.2 Differential Scanning Calorimetric Data .....	123
6.3 SAXS/WAXS Results.....	128
6.4 AFM Results .....	130
<b>7. CONCLUSIONS.....</b>	<b>166</b>
7.1 Inferences .....	166
7.2 Contributions.....	168
<b>8. REFERENCES .....</b>	<b>170</b>

## LIST OF TABLES

1. Film/Coating Process Mechanisms, Pros and Cons .....	4
2. R2R Coating and Film Formation Types .....	9
3. Independent Variables Affecting the Thin Film Deposition .....	74
4. Variables Dependent on the Polymer Weight Percent .....	74
5. Final Set of Independent Variables for Investigation .....	75
6. Output Response Variables .....	75
7. Energy and Material Usage for Samples Processed Under Different Conditions .....	83
8. Glass and Melt Transitions for all the DMAC Based Samples from this Work.....	125
9. Glass and Melt Transitions for all the THF based Samples from this Work.....	126
10. SAXS Datasets for All Samples Fabricated in this Work .....	136
11. AFM Datasets for All Samples Fabricated in this Work.....	165

## LIST OF FIGURES

1. a) Simplex single chamber system with valves. Only one primary chamber is present for the liquid to be atomized by the high pressure air, b) Dual chambered duplex system with: a larger primary chamber for higher atomization rates and a smaller secondary chamber for lower atomization rates, c) A fan spray system where high pressure atomizing air from a fan splits the liquid emanating from the nozzle into droplets. ....16
2. Ultrasonic nozzle system with a conical profiled tip. The liquid to be atomized is metered to the tip through a specially machined internal pathway. The nozzle vibrates along its axis with the maximum peak amplitude occurring at the tip. The metered liquid forms a thin film at the nozzle tip and is split into droplets by the longitudinal wave.....24
3. A generalized slice of a nozzle body has been shown here. At any particular section of the slice, the force equilibrium conditions have to be satisfied. The forces can be expressed in terms of the wave displacement  $Y(x,t)$  and nozzle material properties resulting in the wave equation (9).....24
4. a) the conical profiled, flat faced and wide dispersion atomizing probes are shown here. Different nozzle tip profiles provide for a way to control the shape/extent of the final spray pattern. b) The spray shapes possible with these probes are shown here. The last two spray patterns to the right are side and front views of the wide dispersion nozzle.....29
5. Typical two-phase microstructure of a TPU copolymer has been shown here. The soft (S) and the hard (H) segments are thermodynamically incompatible and form

aggregate domains of S and H segments. This results in the development of an S and H phase within the microstructure. The S phase is a matrix of S domains while the H phase acts as reinforcements. ....46

6. a) Falling ball viscometry measurements where the time taken by the falling ball in a liquid column to fall (between calibrated lines) is used to measure the viscosity b) Density measurements where the calibrated volume markings are used in conjunction with a 0.0001 g balance for computing density .....56

7. a) Surface tension measurement setup, b) Needle tip with no droplet, c) Needle tip with water droplet. The pendant droplet was allowed to develop over a period of 20-30 seconds.....57

8. a) Solution Preparation, b) Glass mold with flat bottom, c) Mold with covered petridish.....59

9. Schematic of an Ultrasound Assisted (UA) deposition system with substrate mounted on the chuck of the spin coater. A spin-coater essentially works on the principle of centrifugal forces spreading the solution onto the substrate at moderate to high speeds (600-6000 RPM). In our case, the spin-coater is used at a very low speed to just allow for the uniform deposition of the film. ....60

10. Ultrasound Assisted Deposition System with substrate mounted on the Chuck of the spin coater, b) heater temperature controller, c) glass chamber with heat pad, d) substrate on chuck of spin coater, e) Air-draft, f) Concentric draft attachment ..61

11. Step by step thin film test coupon preparation procedures .....67

12. Tensile thin film test protocol .....68

13. TPU film with dried out droplets evident. These droplets are in the form of polymer particulates yielding a grainy film surface. ....	77
14. Mechanisms of film formation and microstructures achieved a) without and b) with air-draft .....	80
15. Spray Patterns as a function of draft pressure. We see that as the air-draft pressure is increased from zero to 1 psi, the spray width changed .....	86
16. Effects of varying the liquid to air ratio. As the liquid to air ratio increases, a higher degree of coalescence is evident. As a result, the number of droplets collected increased together with an increase in their sizes.....	89
17. Apparent droplet diameter distributions for the 25 $\mu$ L/min.....	90
18. Apparent droplet diameter distributions for the 50 $\mu$ L/min.....	91
19. Apparent droplet diameter distributions for the 150 $\mu$ L/min.....	92
20. Median droplet diameter data as a f(solution density).....	94
21. Median droplet diameter data as a f(solution surface tension) .....	95
22. Median droplet diameter data as a f(solution viscosity) .....	96
23. Median droplet diameter data as a f (flow rate).....	97
24. Solution volume requirements as a f (solution wt%).....	99
25. Average polymer film thickness as a f(solution wt%).....	99
26. Solvent evaporation measurement set-up (inset) and data in a) normal and b) log scale.....	100
27. 40X image of the 0.2% film (23% energy, 45°C,150 $\mu$ L/min) .....	103
28. 40X image of the 0.2% film (29% energy, 45°C, 150 $\mu$ L/min) .....	103
29. 40X image of the 0.2% film (23% energy, 45°C, 150 $\mu$ L/min) .....	104

30. 40X image of the 2% film (29% energy, 45°C, 50μL/min) .....	104
31. 40X image of the 2% film (29% energy, 45°C, 150μL/min) .....	105
32. 40X image of the 2% film (29% energy, 80°C, 150μL/min) .....	105
33. 40X image of the 2% film (37% energy, 45°C, 150μL/min) .....	106
34. 40X image of the 2% film (46% energy, 45°C, 150μL/min) .....	106
35. 40X image of the 4% film (37% energy, 45°C, 50μL/min) .....	107
36. 40X image of the 4% film (37% energy, 45°C, 150μL/min) .....	107
37. 40X image of the 4% film (37% energy, 80°C, 150μL/min) .....	108
38. 40X image of the 4% film (46% energy, 45°C, 150μL/min) .....	108
39. Bath sonication dependent trends in the tensile response .....	112
40. Fracture strain as a f(sonication time).....	112
41. Fracture strength as a f(sonication time).....	113
42. Energy to fracture as a f(sonication time).....	113
43. Example stress-strain plots for the case of a 2% atomized film made at 45°C, 150μL/min and 29% energy .....	116
44. Example stress-strain plots for the case of a 2% atomized film made from THF at 45°C, 350μL/min and 23% energy .....	116
45. Computed fracture strains for all samples tested at 5mm/min.....	117
46. Computed fracture strengths for all samples tested at 5mm/min.....	118
47. Computed energies of fracture for all samples tested at 5mm/min .....	119
48. Computed fracture strains for all samples tested at 50mm/min.....	120
49. Computed fracture strengths for all samples tested at 50mm/min.....	121
50. Computed fracture toughness value for all samples tested at 50mm/min .....	122



51. Sample DSC Curve for a 45°C, 4%, 37% energy, 150µL/min film .....	123
52. SAXS intensities for 0.2% samples plotted as a function of scattering vector .....	133
53. SAXS intensities for 2% samples plotted as a function of scattering vector .....	133
54. SAXS intensities for 4% samples plotted as a function of scattering vector .....	134
55. Example plot of square of scattering vector times intensity as a f(scattering vector) used to calculate the invariant .....	135
56. Example plot of Porod law fit to the latter part of the SAXS profile corresponding to the H to S domain transitional region .....	136
57. a) Topographic and b) Phase images and c) RMS roughness's for unsonicated THF based cast TPU film .....	137
58. a), b), c) are three sample images of selected regions within the phase image in Figure 57 b .....	138
59. Topographic and b) Phase images and c) RMS roughness's for 30 minute sonicated THF based cast TPU film .....	139
60. a), b), c) are three sample images of selected regions within the phase image in Figure 59 b .....	140
61. Topographic and b) Phase images and c) RMS roughness's for 60 minute sonicated THF based cast TPU film .....	141
62. a), b), c) are three sample images of selected regions within the phase image in Figure 61 b .....	142
63. Topographic and b) Phase images and c) RMS roughness's for 90 minute sonicated THF based cast TPU film .....	143

64. a), b), c) are three sample images of selected regions within the phase image in Figure 63 b .....	144
65. Topographic and b) Phase images and c) RMS roughness's for a 2E1T2150S12 atomized DMAC based film .....	145
66. a), b), c) are three sample images of selected regions within the phase image in Figure 65 b .....	146
67. Topographic and b) Phase images and c) RMS roughness's for 2E1T250S11 atomized DMAC based film .....	147
68. a), b), c) are three sample images of selected regions within the phase image in Figure 67 b .....	148
69. Topographic and b) Phase images and c) RMS roughness's for 2E1T4150S10 atomized DMAC based film .....	149
70. a), b), c) are three sample images of selected regions within the phase image in Figure 69 b .....	150
71. Topographic and b) Phase images and c) RMS roughness's for 2E2T2150S10 atomized DMAC based film .....	151
72. a), b), c) are three sample images of selected regions within the phase image in Figure 71 b .....	152
73. Topographic and b) Phase images and c) RMS roughness's for 2 pct control cast DMAC film .....	153
74. a), b), c) are three sample images of selected regions within the phase image in Figure 73 b .....	154

75. Topographic and b) Phase images and c) RMS roughness's for 2E3T2150S10 atomized DMAC based film .....	155
76. a), b), c) are three sample images of selected regions within the phase image in Figure 75 b .....	156
77. Topographic and b) Phase images and c) RMS roughness's for 2E1T2350S7 atomized DMAC based film .....	157
78. a), b), c) are three sample images of selected regions within the phase image in Figure 77 b .....	158
79. Topographic and b) Phase images and c) RMS roughness's for 4E1T2150S4 atomized DMAC based film .....	159
80. a), b), c) are three sample images of selected regions within the phase image in Figure 79 b .....	160
81. Topographic and b) Phase images and c) RMS roughness's for 4E1T4150S4 atomized DMAC based film .....	161
82. a), b), c) are three sample images of selected regions within the phase image in Figure 81 b .....	162
83. Topographic and b) Phase images and c) RMS roughness's for 4E2T2150S4 atomized DMAC based film .....	163
84. a), b), c) are three sample images of selected regions within the phase image in Figure 83 b .....	164

## ABSTRACT

An Ultrasound assisted Atomization (UA) system has been developed and investigated to synthesize  $\sim 20\mu\text{m}$  polyurethane thin films with uniform, repeatable thickness and microstructure. The UA system comprised a 20 kHz atomizer probe mounted on  $750\text{ W/cm}^2$  transducer, a heated glass chamber and a rotating substrate. The rationale for the work has been built through a careful Design of Experiments (DoE) that sought to answer questions regarding the process-microstructure relationships from both the spray and material points of view. The independent variables chosen were the polymer solution weight percentage (0.2%, 2%, and 4%), power amplitude (energy) percentage supplied to the nozzle (23%, 29%, 37%, and 46%), the temperature of deposition ( $45^\circ\text{C}$ ,  $80^\circ\text{C}$ ) and flow rate ( $50\mu\text{L/min}$ ,  $150\mu\text{L/min}$ ).

The research questions focused on influence of the process parameters on the microstructure and properties of the film. One of the problems involved fixing the trajectory of the spray and also making use of the droplet surfaces created by the spray. To achieve this, a simple air-draft attachment was devised and the influence of the same was evaluated through process and film characterization experiments. A mechanism for the draft has been schematically provided. The use of such a draft to fabricate thin polymer films via ultrasound atomization has not been achieved before and represents a ‘first step’ in advancing this ultrasound technology.

The primary findings of the work were that the film microstructure and properties were heavily influenced by the flow rate, energy of atomization, and test temperature. In addition, the droplet diameters seemed to be readily amenable to change for the 0.2 and

2% solutions and the use of the air-draft made the process feasible, repeatable and accurate. For the 4% solutions, viscosity seemed to stabilize the liquid solution film at the tip requiring larger energies of atomization. In all, relative to the 0.2% films the fracture strengths, strains and toughness values had improved vastly for 4% and 2%.

Calorimetric, Small Angle X-ray scattering and Atomic Force Microscopy (AFM) measurements showed a largely phase mixed hard segment-soft segment morphology. Calorimetry showed that the 0.2% specimens showed higher melting points (between 110-130°C) indicative of greater hard domain ordering in these samples. This is not evident in the 2% and 4% samples. This trend is supported by the Small Angle X-ray scattering and AFM data. The X-ray data show larger domain sizes and greater invariants for the 0.2% samples relative to the 2% and 4% samples. The AFM phase image measurements provided hard domain widths in the same range as the X-ray measurements (10-11 nm). All of the topographical trends from AFM showed that surface morphology was affected by i) increasing atomization energies from 29%-46% of energy (decreased surface roughness from 3 nm to 2 nm for 2% films and 1 nm to 0.5 nm for 4% films) ; ii) increasing film fabrication temperature from 45°C-80°C (increased roughness from 3nm to 4-5nm in local spots for 2% films and from 0.5nm to 0.6 nm for 4% films), iii) decreasing flow rate of the pump from 150 $\mu$ L/min to 50 $\mu$ L/min (comparable roughness for the case of the 2% films from 3nm to 2nm). These could explain the trends in mechanical responses as a f( energy of atomization and temperature).

In order to examine sample crystallinity, we performed Wide Angle X-ray Scattering which showed a fully amorphous polymer structure. The lack of any reflections indicated

that the melting points observed from calorimetry were not due to long range order in the material but due to pseudo crystalline behavior. This behavior could be ascribed to the formation of urethane-urethane ordering with hydrogen bonds between them. In general, ultrasonic energy of the capillary wave causes phase mixing and the extent of phase mixing was dependent on the weight percentage of polymer solution and the type of solvent. It was highest for the 4% samples and lowest for the 0.2% samples.

# Chapter 1.

## INTRODUCTION

### 1.1 Film Process Methods

Much of the present day fascination with thin films began with the extremely successful electronics revolution. Sensor applications (commercial and scientific) rely on microelectronics with integrated chip (IC) fabrication technologies and work with semiconductors and ceramics. Typically, micron scale electronic component fabrication involves silicon epitaxy (crystal growth) followed by several stages of oxide layer formation, photolithography of a pattern on to a UV curable photoresist (polymer film that cures when exposed to UV), etching of the pattern onto the silicon surface (typically (110) or (100) planes) and dopant distribution via diffusion and ion-implantation procedures [1]. Controlled metallization of a *thin metal film* as an output lead is finally performed via sputtering.

Thus ceramics exhibit a distinct grain structure and porosity that can be tailored for particular applications requirements during the sintering process at high temperatures. Specifically, alumina and glass-ceramic multilayer substrates are used for hermetic packaging of sensorial elements. Typically these thick laminates/films are prepared by the mixing of an organic binder with the ceramic followed by compaction and sintering around 1000-1500°C. The sintering process contracts the specimen leaving a solid ceramic sample or lamina. The process allows for easy metallization of *thin metal film* contacts by first punching holes through the lamina and then filling the cavities with the chosen metal paste i.e. tungsten.

Essentially the fully packaged IC is a multilayer system composed of several thin layers and is usually a multicomponent system performing multiple functions [1]. As mentioned earlier, interest in films grew concurrently with the use and popularity of semiconductor and ceramic based electronics. The materials processing community specifically view structures between 10-50 $\mu\text{m}$  as *thick* films and structures between 10-200 nm as *thin* films [1,2]. The necessity for developing such thin/thick structures could be directly mapped to the ever growing demand for reducing the size of electronic components, thereby reducing energy consumption without compromising on performance.

Initial focus was on developing viable metal deposition techniques that could function as conducting leads on an IC developed on a silicon wafer. *Chemical vapor deposition (CVD)*, *electrochemical deposition/oxidation*, *thermal oxidation* and *current-less chemical deposition* are some chemical methods for synthesizing these films. Physical methods include *vacuum evaporation*, *cathode sputtering (including reactive sputtering)*, *RF (radio frequency) sputtering*, *magnetron sputtering* and *screen printing*. CVD, as the name suggests, utilizes chemical reactant vapors at high temperatures and used in vapor phase epitaxy, depositing conductive/insulating layers and more recently nanoparticles. It typically results in the replication of the substrate (crystal surface) texture producing films of a certain microstructure. Almost all of the other physical deposition methods mentioned here (except screen-printing) involve a high energy system used to either evaporate the film matrix from a melt state or just vaporize the metal particles by ion bombardment. Screen printing follows a lithography type concept where the screen or

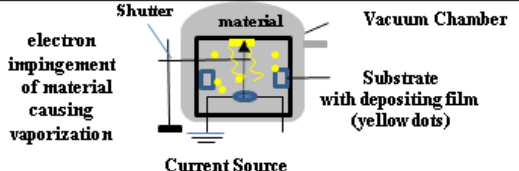
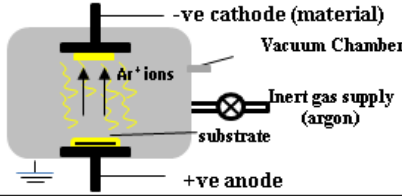
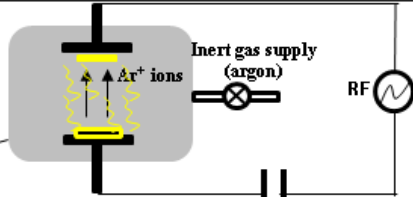
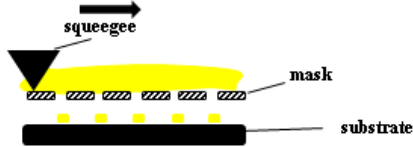



mesh is a circuit pattern and a squeegee is used to squeeze the film matrix onto a substrate.

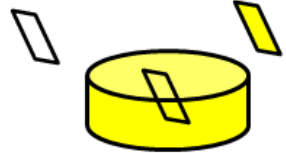
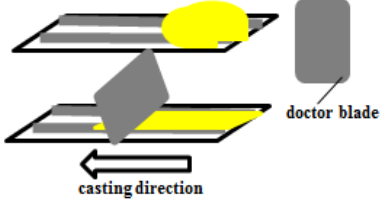
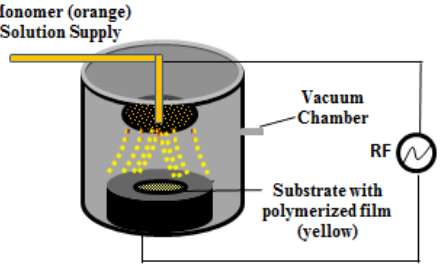
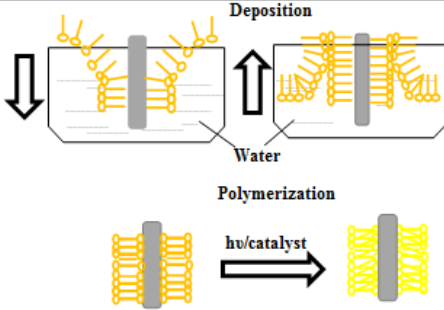
For polymer films, the process technology mirrors the vacuum methods that exist for depositing metals. The only difference is the state of the precursor material, which in the case of polymers is typically in the form of a monomer gas or a sol-gel where the polymer is dissolved in a carrier solvent. The energy source for polymerization is a high energy plasma (radio frequency) or just pyrolysis under vacuum [1]. Other conventional techniques include spin-coating, dipping, bath immersion, and casting using a doctor knife. While plasma assisted deposition demands significant capital investment and is energy intensive, it provides very repeatable microstructures and thickness control. The conventional techniques such as dipping, casting, and bath immersion have drawbacks that are related to productivity, amount of material used, and achievable film thicknesses. Spin coating can handle a wide array of thickness values ranging between nanometer thick to several microns thick. The disadvantages are the large amount of material needed to make nanometer thick films and that only flat surfaces can be coated.

Finally, the Langmuir-Blodgett technique makes use of the hydrophobicity of the substrate to selectively deposit several nanometers of polymer layers with hydrophobic heads and hydrophilic tails. The biggest advantage of this process is its adaptability to applying functional polymers onto device substrates as sensing elements. Obviously there are disadvantages with respect to mass production and sensor stability. Table 1 lists some of the important processes mentioned above and depicts the schematics of the mechanisms and lists relative merits and demerits.

**Table 1: Film/Coating Process Mechanisms, Pros and Cons [1]**

Process	Type	Mechanism & Schematic (yellow = depositing film material)	Comments	
			Pros	Cons
<i>Vacuum Evaporation</i>	<i>Physical</i>	<p>electron impingement of material causing vaporization</p>  <p>Vacuum Chamber Substrate with depositing film (yellow dots) Current Source</p>	<ul style="list-style-type: none"> <li>* Minimal contamination</li> <li>* Allows flexibility in types of materials used</li> </ul>	<ul style="list-style-type: none"> <li>* Need for ultrahigh vacuum for thermionic emission</li> <li>* Polymers degrade at high temperatures</li> </ul>
<i>Cathode Sputtering</i>	<i>Physical</i>	<p>Ar<sup>+</sup> ions in plasma sputter the cathode</p>  <p>-ve cathode (material) Vacuum Chamber Inert gas supply (argon) substrate +ve anode</p>	<ul style="list-style-type: none"> <li>* allows precise coating by varying DC voltage</li> </ul>	<ul style="list-style-type: none"> <li>* Process initiation takes more time</li> <li>* Insulating materials cannot be deposited</li> </ul>
<i>RF Sputtering</i>	<i>Physical</i>	<p>Ar<sup>+</sup> ions in plasma sputter the cathode whilst the anode is capacitively coupled to an RF source</p>  <p>Inert gas supply (argon) RF Vacuum</p>	<ul style="list-style-type: none"> <li>* allows polymer deposition as an RF source is utilized which permits the electrodes to charge</li> </ul>	<ul style="list-style-type: none"> <li>* RF sources are typically high voltage/high energy</li> <li>* RF sources are expensive</li> </ul>
<i>Screen Printing</i>	<i>Physical</i>	<p>A squeegee is used to 'squeeze' material through a 'mask' resulting in a desired pattern on a substrate</p>  <p>squeegee mask substrate</p>	<ul style="list-style-type: none"> <li>* LBL multilayer structures possible</li> <li>* Different materials can be applied to each layer</li> </ul>	<ul style="list-style-type: none"> <li>* Low productivity</li> <li>* Complicated features cannot be realized</li> </ul>
<i>Spin Coating</i>	<i>Physical</i>	<p>Centrifugal force acts on a syringe dispensed suspension causing spreading and drying</p>  <p>Syringe RPM Controller High Speed Spinning RPM Controller</p>	<ul style="list-style-type: none"> <li>* LBL multilayer structures possible</li> <li>* Different materials can be applied to each layer</li> </ul>	<ul style="list-style-type: none"> <li>* Material wastage is high</li> <li>* Coating non planar shapes is not possible</li> </ul>

**Table 1:** Film/Coating Process Mechanisms, Pros and Cons [1]

<p><i>Dip Coating</i></p>	<p><i>Physical</i></p>	<p>In its simplest form, the process involves dipping the film mold or substrate in a trough of the solution</p>		<ul style="list-style-type: none"> <li>* Easy to implement</li> <li>* Multilayer structures possible</li> </ul>	<ul style="list-style-type: none"> <li>* Thickness control is imprecise and any degree of precision is dependent on automation of the dipping step</li> </ul>
<p><i>Doctor Blade Casting</i></p>	<p><i>Physical</i></p>	<p>Solution or a suspension is poured between a pair of shims of a predetermined thickness and the solution spread using the edge of a polished doctor blade</p>		<ul style="list-style-type: none"> <li>* Easy to implement</li> <li>* Multilayer structures possible</li> <li>* Thickness control is precise</li> </ul>	<ul style="list-style-type: none"> <li>* Does not work effectively for dilute solutions</li> <li>* Does not work for non planar shapes</li> </ul>
<p><i>CVD/Plasma Assisted CVD</i></p>	<p><i>Chemical</i></p>	<p>Metered supply of the monomer solution is provided to an electrode subject to RF ac. RF energy polymerizes the monomer resulting in a thin film on the substrate</p>		<ul style="list-style-type: none"> <li>* Allows hybrid processing of materials</li> <li>* Multilayer structures possible</li> <li>* Thickness control is precise</li> </ul>	<ul style="list-style-type: none"> <li>* RF ac sources are expensive</li> <li>* Higher voltage/energy requirements</li> </ul>
<p><i>Langmuir-Blodgett</i></p>	<p><i>Chemical</i></p>	<p>Drops of the polymer/precursor monomer (orange) dissolved in a volatile solvent are dripped onto the surface of water. Hydrophobic tails of the dissolved molecules orient in direction opposite to that of water molecules. Films can be obtained this way by repeated dipping and subsequent polymerization</p>		<ul style="list-style-type: none"> <li>* Easy to implement</li> <li>* Multilayer structures possible</li> <li>* A method to carefully tailor/control physical and chemical properties</li> </ul>	<ul style="list-style-type: none"> <li>* Reported performance instabilities associated with polymer film devices made from this method</li> </ul>

## 1.2 Film Applications

Scientific interest in thin films is driven by applications such as sensors, actuators, and energy conversion devices (transducers). These structures require the ability to respond to physical/chemical stimuli which is converted to an electrical signal for further use/analysis. These “devices” are of engineering value that can be deployed in real-life situations. The stimuli could be gravimetric (mass absorption via swelling), resonance (change in fundamental vibration frequency of a coated quartz crystal), pressure or force, impedance or capacitance (resistance/capacitance change), calorimetric (heat change), piezoelectric (mechanical to electrical and vice versa), tactile (response to human touch), semiconducting/conducting (properties similar to traditional silicon/GaAs or Gallium Arsenide), and finally permselectivity which is the preferential permeation of one specific gas instead of another in gas separation [1,2].

Thus, research on developing innovative materials/processing techniques has been driven by the requirements/needs of specific applications. From a standpoint of science and understanding, this process-application relationship is a symbiotic one. Almost all of the following descriptions of key thin film research in this section exhibit this relationship. As a result, there is significant over-lap of published work involving innovative processes and new applications. For example, a Layer-By-Layer (LBL) type boron doped diamond film embedded with Pt particles (Pt loading of  $75.8\mu\text{g}/\text{cm}^2$ ) and recoated with diamond was fabricated via a unique *galvanostatic deposition* method with the intent of replacing commercial  $\text{sp}^2$  carbon electrodes used in fuel cells prone to corrosion and structural failure. The new composite electrodes had better corrosion resistance while the Pt particle size ranged between 10-300 nm [3]. Oxygen reduction capability of these

electrodes measured via cyclic voltammetry was comparable to that of Pt on carbon supports.

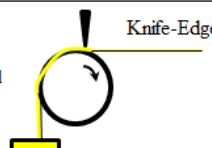
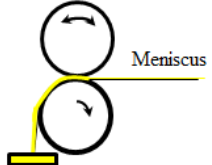
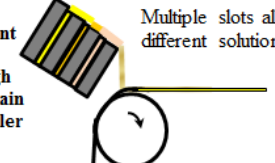
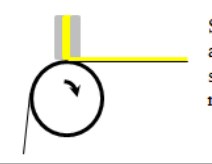
In another study, Chen et al. [4] developed a new processing technique in order to improve current switching properties of dielectrics. The hybrid procedure consisted of a spin coating and baking step coupled with a thermal evaporation process for pentacene onto the nanocomposite dielectric layer [4]. Flexible transistors were fabricated from nanocomposites doped with titanium dioxide. A LBL morphology was used to deposit 3,4 polyethylenedioxythiophene-polystyrene sulphonate (PEDOT-PSS) followed by the nanocomposite dielectric/titanium dioxide layer comprising of poly-4-vinylphenol, poly(melamine-co-formaldehyde) and titanium dioxide. Pentacene was then thermally deposited. Permittivity for the nanocomposite OTFT was improved. Relative to the undoped specimens, the measured current voltage characteristics were better as well.

Similarly, Sadaoka et al. [5] have developed thin films of Poly Acrylic Acid (PAA) and Poly Ethylene Oxide (PEO) with methyl calcein dye in them. The dye's fluorescence levels dominated when exposed to chemical species that were acidic and was deactivated in a basic solution. Films were formed on alumina substrates via coating with the solution of the polymer. A Y-type glass fiber was fixed just in front of the film [5]. Film moisture levels were measured via the optical fluorescence technique. Moisture measurements at several humidities showed a better resolution and detection using the PEO film than with the PAA film. The PAA film seemed to indicate sorption better and also humidity levels increased monotonically which they attributed to chemical reactions between calcein and the ammonia species being investigated [5]. Ammonia decreased dye fluorescence with increase in concentration.

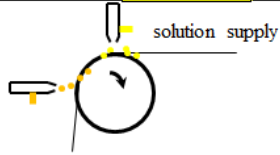
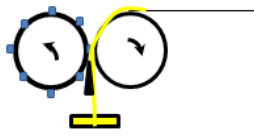
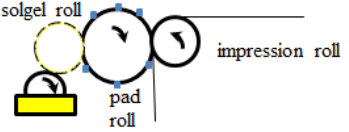
More recently, Deganns et al. [6,7] have developed a Droplet on Demand (DoD) type thin polymer micro/nanostructure processing technique that made use of a piezoelectric device to generate isolated droplets of a dilute polymer solution. This technique falls under inkjet printing and the intended applications were for displays, sustained drug release, polymer light emitting diodes (LEDs), and RC filters [6,7]. In a very comprehensively written review article, Krebbs [8] underscores the importance of new coating and film forming techniques but from a photovoltaic solar cell point of view. The range of film forming and coating methods available for sol-gel type methods are enormous. As mentioned in the previous section, film-forming methods include the traditional methods of coating such as dip coating, casting and spin-coating.

But these techniques do not offer a potential to scale-up and hence R2R or Roll-to-Roll processing has the most promise [8]. Typical R2R film manufacturing involves the use of a flexible substrate that rolls between two roller cylinders that coat the ink or polymer solution onto the substrate. R2R comes in the form of gravure (cylinders with patterns) processing, knife to edge coating (knife maintains constant wet film thickness at the roller edge), slotted die coating (allows coatings and films with different polymer formulations present in different slots), flexo coating (combination of gravure processing with a silicone pad processing) and curtain coating (where parallel curtains of polymer solution coat one on top of each other) [8]. Most of these techniques involve one process that is combined with the R2R mode of synthesis [8]. Interestingly, spray coating using aerosols to coat the substrates is amenable to R2R as well. These coating methods have been schematically shown in Table-2.

**Table 2:** R2R Coating and Film Formation Types [8]

R2R Coating Type	Film/Coating Pattern	Mechanism & Schematic (yellow = depositing film material)	Average Coating Speed ( $\mu\text{m s}^{-1}$ )	Liquid Film Thickness ( $\mu\text{m}$ )
<i>Knife-Over-Edge</i>	<i>0-Dimensional</i>	<p>Roller picks up material from a storage vessel and excess material is doctored off by the knife edge</p>  <p>Knife-Edge</p>	50	20-700
<i>Meniscus</i>	<i>0-Dimensional</i>	<p>Contact spacing between two rollers and hence fluid meniscus is controlled to get a film/coating</p>  <p>Meniscus at contact surface</p>	60	5-500
<i>Curtain</i>	<i>3-Dimensional</i>	<p>Solutions of potentially different types could be dispensed through slots to form a curtain at the tip of the roller edge</p>  <p>Multiple slots allow premixing of different solutions/dyes</p>	75	25-250
<i>Slotted Die</i>	<i>1-Dimensional</i>	<p>Slotted die feeds solution onto a roller mounted with the substrates to be coated</p>  <p>Slotted die size allows control of size of the coating material</p>	40	10-500

**Table 2: R2R Coating and Film Formation Types [8]**

R2R Coating Type	Film/Coating Pattern	Mechanism & Schematic (yellow = depositing film material)	Average Coating Speed ( $\mu\text{ms}^{-1}$ )	Liquid Film Thickness ( $\mu\text{m}$ )
<i>Ink-Jet</i>	<i>3-Dimensional</i>	<p>Solution jet fed via a nozzle onto the flexible substrate on the roller and the coating obtained via droplet deposition</p> 	30	1-500
<i>Gravure</i>	<i>2-Dimensional</i>	<p>A gravure drum with a special pattern or motif forms one roll while the second roll carries the substrate to be coated</p> 	70	5-80
<i>Flexo-Pad</i>	<i>2-Dimensional</i>	<p>Similar concept to gravure R2R but the patterns on the cylinder are made of flexible material</p> 	70	5-250



Also shown in Table-2 are the types of coating patterns possible, the coating speeds in  $\mu\text{m/s}$  and the wet or liquid film thickness in  $\mu\text{m}$  (prior to drying) for each technique. The coating pattern is specified by the dimensionality of the pattern. In a zero dimensional coating or film there is one flat surface (with no pattern) made of one type of material. A 1D coating or film may comprise of stripes of two different materials occurring in an alternating fashion. Similarly 2D coatings may have the same pattern repeated in mutually perpendicular directions. 3D coatings typically involve the creation of varying patterns layer by layer.

Digressing from the discussion on thin film applications, very little has been done to investigate the influence of process parameters on coating and film thicknesses via aerosol-assisted deposition. Titania ceramic thin films were fabricated by Krumdieck and Raj [9,10] for the purpose of developing thermal barrier coatings (TBC) for gas turbines. Their system called the pulsed metal oxide chemical vapor deposition (MOCVD) utilized a Sonotek pulsing ultrasonic atomizer delivering a precursor  $\text{TiO}_2$  solution to a pyrex glass chamber furnace. Their system was capable of fabricating  $45\mu\text{m}$  coatings between  $400\text{-}600^\circ\text{C}$  [9,10]. From an industry perspective, Sonotek's Berger [11] and Leiby [12] showed the earliest proof of concept for obtaining polymer coatings on stents using an ultrasonic atomizer.

Essentially the coatings obtained were conformable to substrate targets of any shape, involved the use of lower energy, had less material wastage, and were more attuned to the concept of bottom up layer-by-layer (LBL) manufacturing. Ye et al. were the first set of researchers to report the fabrication of ferroelectric thin Poly(Vinylidene Fluoride) (PVDF) films via ultrasonic atomization of a polymeric solution mist [13-15]. Their goal

was to develop polymeric piezoelectric coatings and films with a view to using them in sensors/actuators. Further significant information regarding atomization will be furnished in the next section that focuses on ultrasonic atomization.

Reverting back to the discussion on thin film applications, another area with a huge potential to bring about social, financial and technological change is DEA or dielectric actuators (DEA). They work on the simple principle of an accumulated charge causing mechanical actuation and vice versa; meaning that electricity can be generated from mechanical motion. Thin films of dielectric elastomers such as silicones, or interpenetrating networks (IPN) of elastomers with other materials such as acrylics, rubbers are drawing a lot of interest [16-20]. The enormous amount of energy or work density possible in such materials offers hope for futuristic robotic devices that might simulate human-like activity [17, 19, 20]. In fact, the flexibility of elastomers lend themselves to being used as sensory and transduction elements as well. In a newer area referred to as adaptive optics; elements such as lenses, mirrors and gratings have also been manufactured from elastomers [21]. A Poly Di Methyl Siloxane (PDMS) grating mirror lens has been manufactured via a LBL process where the two part PDMS is poured onto a grating mold and the sample replica removed. Optical properties were then found to be variable as a function of stretching at different strains [21].

Another set of workers used a combination of spin-coating and photo-grafting to manufacture 4-7 nm thick films on curved surfaces. The photo initiator was first coated onto the surface followed by exposure to EM radiation  $> 320$  nm wavelength to result in film formation. Thickness was varied by varying the MW or molecular weight of the polymer formulation [22]. From an end-use perspective, a great deal of attention has

been paid to developing functional polymer films/sol-gel nanoparticle coatings that cater to specific applications such as corrosion sensing and strain sensing [23], thermal management [24], optoelectronics [25-27], chemical sensors [28,29].

For semiconductor applications such as transistors for switching on/off applications, polymers offer ease of processing and savings in material costs compared to the traditional silicon based electronics [30]. An extensive review article in this field states that semiconductor electronics require sufficiently high field-effect mobility values. From a chemical synthesis stand point, researchers have improved the mobility values by an order of magnitude and have used solution (typically poly hexyl thiophene polymer), vacuum deposition (typically pentacene polymer) methods for their work [30]. Workers have documented that the solution processing route provides not only a) the flexibility to fabricate LBL but also b) help manipulate the crucial field mobility values as a function of solvent type [30].

### **1.3 Scope of the Work**

In summary, most of the aforementioned works have a common theme of application oriented research and for this; LBL processing has been attractive for generating new materials and device applications. Also, LBL processing is amenable and applicable to a variety of diverse fabrication methods.

In this dissertation, the main focus has been on experimentally investigating the applicability of this concept to Ultrasonic Atomization (UA) assisted deposition. In particular, thin Thermoplastic Poly Urethane (TPU) film fabrication has been carried out by UA assisted deposition. The influence of critical process parameters such as energy

supplied to the atomizer, polymer solution density, surface tension, viscosity on film processing have been studied using a Design of Experiment (DoE) approach. In addition to process characterization of UA via optical microscopy, the process-material microstructure relationships have been investigated via mechanical testing, X-ray scattering, Atomic Force Microscopy (AFM) and calorimetry. Pointed research questions have been posed at the end of chapters 2 (section 2.8) and 3 (section 3.4). All of the work has been performed to obtain specific answers to these questions. Further, a much more detailed scope of the work has been provided in chapter 4 (section 4.10).

## **Chapter 2.**

### **ULTRASONIC NOZZLES AND ULTRASONIC ATOMIZATION**

#### **2.1 Motivation for Ultrasonic Atomization and its Recent Applications**

Prior to describing the working mechanisms of Ultrasonic Atomization (UA), the context for the work has been built by reviewing the motivation and applications of this technology. UA offers some advantages as opposed to the conventional spray atomization (via pressure). This technique already exists in the industry and is applied in producing fuel sprays in gas turbines and engines, chemical processing, oil burners, paint spraying and in treating crops with agricultural grade pesticides. The most popular method of atomizing is via a pressure jet where a high speed air jet breaks the liquid film into droplets of spray.

There are several sub classes of atomizers depending on the type of nozzle geometry used: simplex or one chamber, duplex or two chambers, the mode of use of air: injection, swirl, and air-blast/air-assist, high pressure fan spray (where there is a primary liquid nozzle and a primary orifice for atomizing air [31]). These are shown in Figure 1 a-c. In simplex atomizers, there is one primary chamber capable of handling a large atomization rate. In duplex atomizers, there are two chambers: primary and secondary. The role of the primary chamber is the same as in a simplex design while the secondary smaller chamber is capable of handling smaller flow rates. A fan spray system on the other hand finds use in gas turbines and combustion chambers where a narrow spray is required.

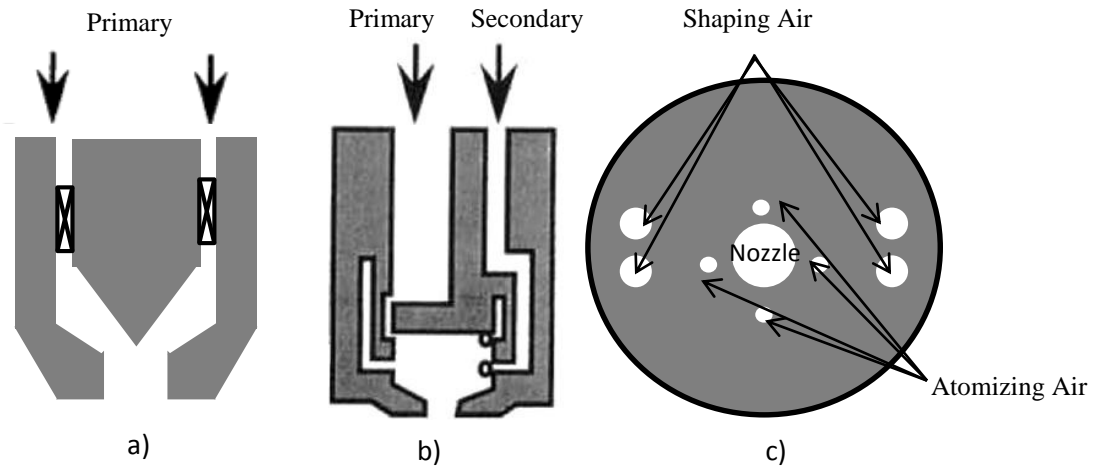


**Figure 1** a) Simplex single chamber system with valves. Only one primary chamber is present for the liquid to be atomized by the high pressure air, b) Dual chambered duplex system with: a larger primary chamber for higher atomization rates and a smaller secondary chamber for lower atomization rates, c) A fan spray system where high pressure atomizing air from a fan splits the liquid emanating from the nozzle into droplets.

This class of conventional atomizers is suitable for applications where droplet size and size distributions are not a major concern (100-1000 $\mu$ m range). However in newer applications like nebulizers, precision printed circuit board coating, controlled humidification and powder/particle production, the droplet size/size distribution become critical. Such applications also require minimal over-spray/splash and low spray velocity. The newer class of atomizers such as electrostatic (fluid-electrode potential breaks the fluid in to droplets), effervescent (injection of low pressure air to sustain bubble formation within liquid which then is “squeezed out by liquid layers in to fine droplets) and UA (capillary wave assisted) fall in this category.

With UA, one limitation as opposed to industry type equipment is the low spray angle [31]. However ultrasonic atomizers use much less energy to atomize liquids compared to the traditional atomizers. The droplet size distribution obtained is narrow (1-5 $\mu$ m with a 55 kHz nozzle) and low velocity. However atomization efficiency or the volume of liquid successfully atomized per unit supplied volume is heavily affected at flow rates larger than 1 L/min [31]. Unlike the conventional atomizers, the instabilities can be controlled very precisely (by varying frequency, energy, flow rate) assuming the solution or liquid properties stay constant. Design wise, the geometry/fluid pathways in an ultrasonic atomizer are very simple compared to the industry popular pressure atomizers. As a result, the chances of material clog issues during use are minimized. Also, the pressures required for atomization of the liquids in such cases is in the range of 50-100 MPa which forms a significant portion of the energy input into the system. UA on the other hand does not use air. Instead it uses an energy output system that varies to sustain a set displacement at the nozzle tip (depending on the properties of the liquid). Unlike

electrostatic atomization which requires an electrically conducting fluid, UA can handle any type of fluid as long as the surface tension/viscosity/density matches with the acoustic energy capability of the system.

Essentially varying fluid properties and the instability growth control (frequency, energy or amplitude) should throw open an arena of opportunities to innovate and produce interesting materials and new applications. Specifically, workers have synthesized copper micro/nanoparticles via ultrasonic atomization with a view to making use of the high aspect ratio and large surface area properties of the particle for mechanical property improvements [32]. Recently production of CNTs (carbon nanotubes) from ferrocene toluene/alcohols has been attempted using a nebulizer fitted with an ultrasonic transducer operating at 1.6 MHz. The ferrocene mist was essentially carried into a furnace operating at 900°C where the CNTs form on the catalyst bed [33].

In another application, titania ceramic thin films were fabricated by Krumdieck and Raj for the purpose of developing thermal barrier coatings (TBC) for gas turbines. Their system called the pulsed MOCVD utilized a pulsing ultrasonic atomizer delivering a precursor TiO<sub>2</sub> solution to a pyrex glass chamber furnace. Their system is capable of fabricating 45µm coatings between 400-600°C [9,10]. Leiby [11] and Berger [12] have both shown the use of ultrasonic atomizers to prepare biocompatible polymer coatings for cardiac stents. Ross and Gleason have used ultrasonic atomization in a plasma enhanced polymerization chamber with the ultrasonic probe acting as one electrode in the RF or radio frequency set-up [34]. They introduced polystyrene particles into a matrix of carbon doped silicon dioxide that forms during the plasma polymerization of Tetra EthOxy Silane (TEOS). The end product was a nanocomposite thin film intended for use



in optoelectronics, electrodes and other optical uses [34]. More recently, Barba et al. were able to successfully produce biopolymer microparticles that have applications in the pharmaceutical/nutraceutical science field. The particles were fabricated by atomizing alginate onto a copper sulfate solution that resulted in the reticulation or vitrification of the sprayed droplets to form the microparticles [35].

## **2.2 Thin Polymer Film Fabrication via UA**

Kimoto et al. were the first group of researchers that worked on ultrasonic atomization of polymer solutions. They atomized dilute solutions of rod shaped poly ethylene oxide (PEO), poly vinyl pyrrolidone (PVP) and a glycerin-water mixture. They characterized the atomization efficiency and the droplet diameter distributions as a function of volume flow rate of the polymer solutions. They observed that the atomization efficiency (a ratio of volume of liquid atomized to total volume supplied) was low for PEO. To investigate this phenomenon, they reduced the molecular weight (MW) of the PEO via sonication and then atomized these solutions again. They observed that the atomization efficiencies were now similar to the ones for PVP and the glycerin-water mixture. By measuring the critical acceleration of the surface wave using a camera, they concluded the higher MW PEO solutions were stabilizing the capillary surface wave and thus reducing the atomization efficiency [36].

These researchers were then followed by Tsai and Luu [37] who worked on a Sonotek nozzle developed by Berger [11,12] of 54 and 110 kHz with the intent of spray drying and pyrolysis to produce nanoparticles of polymer. Their work also involved the use of dilute solutions (0.1-0.2%) of an aqueous based xanthan gum polymer, the precursor

aqueous solution and a Newtonian liquid glycerol as a control [37]. Their work was focused on enhancing ultrasound assisted atomization by introducing co-flowing air hence aptly termed as the ultrasound modulated two fluid atomization (UMTF). The idea was to decrease the droplet size and also come up with a way to narrow down the droplet size distribution. Using a laser scattering-based Malvern particle/droplet analyzer they measured droplet diameters for both nozzles. They determined that for the same nozzle frequency, the non-Newtonian xantham gum solutions absorbed more input power than the Newtonian counterparts [37]. Relative to the Newtonian glycerol liquid, the flow conditions required for atomizing xantham gum were less severe. Also, lower air to liquid ratios was needed for this to occur. Further the droplet size distribution seemed to narrow down as well, which was attributed to the inherent elasticity of the xantham gum solution [37]. This led to an inference that the shape of polymer molecule and polymer molecular weight affects the type of spray generated. Specifically, the different polymer molecules/chains in the spray droplets tended to relax to different stiffness values and their corresponding times of relaxation were also different. They further surmised that even at one fundamental probe operating frequency, liquid capillary waves of other harmonics could be acting on a fluid.

As far as preparation of polymer films/coatings are concerned Ye et al. have been the first set of researchers to report the fabrication of ferroelectric thin Poly(Vinylidene Fluoride) (PVDF) films via ultrasonic atomization of a polymeric solution mist [13-15]. The ultrasonic probe had a column of polymer solution mounted on a ultrasonic water bath. They had an air inlet for supplying air to carry the polymer solution mist on to quartz substrates [13-15]. They have suggested that the frequency of operation of the ultrasonic

transducer affected the final morphology of their thin films. Film thickness increased with an increase in frequency up to 6 MHz beyond which the film thickness decreased. They suggest that at lower frequencies large polymer droplets coalesce with tiny droplets to influence the deposition rate and hence final film thickness. As frequency increases, the number of such large droplets available is almost zero and all available solution is in the form of a very fine mist. Thus the net deposition rate/final film thickness peaks at an optimum frequency where the entire spray is in the form of a homogenous mist.

In a more detailed attempt at understanding the UA coating process, Gaikwad et al. have performed studies on a tip/probe type nozzle utilizing a conveyor belt type substrate movement arrangement. Parameters varied were height of atomizer, the amplitude of atomization, the fluid flow rate, the linear speed of the substrate, the fluid viscosity [38]. The authors utilized filter paper to capture the spray and assuming the area of the isolated and coalesced droplets to be equivalent to the original droplet diameter, they backed out percentage of area covered and the final film thickness. Their observations suggested that film thicknesses on the atomizing tip increased as a function of flow rate to the point where not enough area was available for the fluid to 'hold' and surface tension dependent pinch-off occurred. Percent area covered on the substrate increased as flow rate changed and was also a function of vibration amplitude and height [38]. Knowing flow rate and area covered and assuming accurate full fluid delivery the fluid thickness of the coating was determined. They found that this thickness decreased as a function of increasing substrate to atomizing nozzle distance. Another observation was that with increased power, the atomizing surface did not wait for the liquid to evenly spread resulting in haphazard spray patterns. So if fluid flow was "insufficient", the coatings were of "bad"

quality with no thickness control. For good coatings, they needed to control the critical parameters of flow rate, the amplitude and height. Again they suppose that there is a reduction in thickness at higher vibration amplitudes but also show evidence of densification at the center but scattering at the edges which they think is due to non-uniform film thickness on the atomizing tip [38].

Another significant aspect that needs to be addressed is the nature of the microstructure i.e whether the film is mostly continuous, particulate, or a hybrid. For example, the initial PVDF films from Ye et al's work had had pores/ defects [13-15]. By increasing the polymer wt% or concentration, a more uniform surface was obtained. It could be that the increase in viscosity caused larger droplets that did not necessarily evaporate until it hit the substrate resulting in full coalescence. Leiby [11] in his work with biocompatible stent coatings of polyurethane (PU) in Tetra Hydro Furan (THF) had similar issues. He resolved this issue by placing his sample stents to be coated in a deposition chamber that had vacuum capability. Vacuum was first introduced at 760 mm of Hg and the system isolated from the surroundings. The nozzle in the system was automatically set to incorporate pulses of the PU solution. A THF rich environment was created to not allow THF to "boil" due to the large vapor pressure difference that could otherwise occur in the chamber. Leiby forcefully prevented the THF from "boiling" by very slowly introducing argon gas in to the system. This is he claimed resulted in nice smooth coatings.

This brings us to the question of droplet life time and the parameters controlling the evaporation of a single droplet. Ross and Gleason [34] discuss this issue in more detail in their work on using an UA assisted nanocomposite production where plasma enhanced polymerized polymer forms the matrix. They state that the volatility or non-volatility of

the solvent is also a factor controlling the frequency of dry/wet droplets that reaches the substrate. Their choice of an ideal solvent would be a liquid that is “non-volatile” enough to not evaporate even before atomization but yet “volatile” enough to evaporate just before the droplets hit the substrate to get them wet. Their choice of an ideal solvent would be a liquid that is “non-volatile” enough to not evaporate even before atomization but yet “volatile” enough to evaporate just before the droplets hit the substrate to get them wet. Intuitively with parameters such as temperature, air-flow conditions remaining the same, it is clear that the single variable driving the evaporation is the difference in the partial pressures of the droplet and its environment.

This section has outlined some significant contributions made within the field of UA spray coating of polymers and other liquids. It is thus clear that once the capillary type instabilities induce the fluid film break-up into droplets, a lot of other conditions such as substrate height, flow rate, solvent type, chamber environment, temperature and even substrate movement affects the nature of the deposit. Now that the overall direction of the work is clear, the following sections delve into the theory of ultrasound transducers with a focus on nozzles and UA mechanisms.

### **2.3 Nozzle Fundamentals, Geometries and Parameters**

Ultrasonic transducers fall under the category of energy conversion devices that transform high frequency electrical energy to specific high frequency sound waves. The characteristic wavelengths supported by the components of the transducer assembly depend critically on their dimensions. This ‘characteristic’ wavelength is usually termed

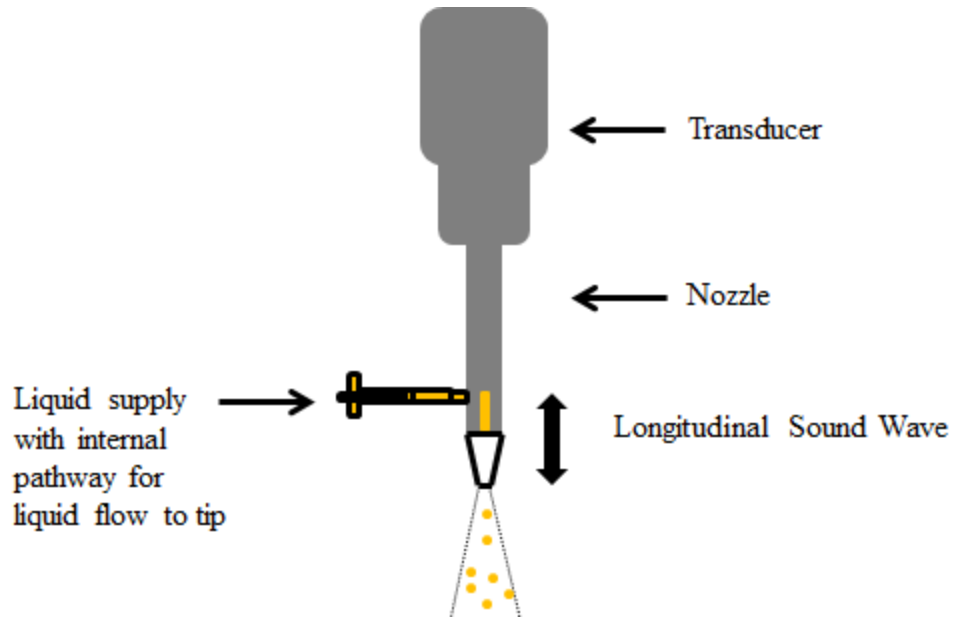


**Figure 2** Ultrasonic nozzle system with a conical profiled tip. The liquid to be atomized is metered to the tip through a specially machined internal pathway. The nozzle vibrates along its axis with the maximum peak amplitude occurring at the tip. The metered liquid forms a thin film at the nozzle tip and is split into droplets.

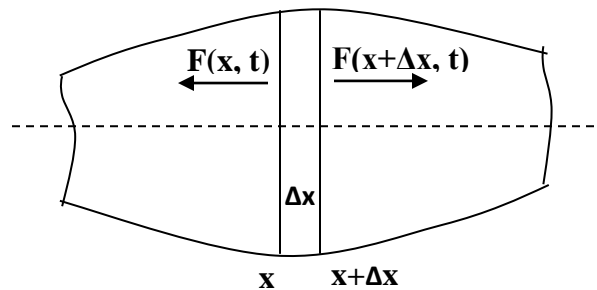


**Figure 3** A generalized slice of a nozzle body has been shown here. At any particular section of the slice, the force equilibrium conditions have to be satisfied. The forces can be expressed in terms of the wave displacement  $Y(x,t)$  and nozzle material properties resulting in the wave equation (9).

the fundamental wavelength. Harmonics of the fundamental might also exist in the field of waves generated. Depending upon the actual frequency values needed, practical horn or nozzle construction involves the use of one of the harmonics of the fundamental for generating these waveforms e.g  $\lambda/2$ ,  $\lambda/4$  etc. The transducer itself is typically built in the form of a ring-type piezo-electric element sandwiched between electrically conducting contact pads/areas [39]. This sub-assembly is mechanically coupled to other elements of interest such as horns or nozzles. Horns come in several geometries but in its simplest form for nozzles, the horn is partially hollow to allow a pathway for the liquid (shown in orange color) (see Figure 2). The type of waves generated in such systems can be both longitudinal and transverse; however the transducing elements are fabricated in such a way that they support purely longitudinal waves (parallel to the direction of motion of the piezoelectric ring element). Due to superposition of multiple waveforms, these longitudinal waves tend to appear as static standing waves. Figure 2 shows an ultrasonically vibrating nozzle system. The standing waves are generated throughout the body of the nozzle along its axis. The liquid is metered into the nozzle from the side and flows through the machined internal pathway reaching the nozzle tip where the maximum amplitude occurs. This amplitude maximum causes the formation/ejection of droplets by creating instabilities in the liquid film.

For a better understanding of the physics of the problem i.e. the boundary/end conditions of a nozzle type system, a simple derivation of the nozzle equation is presented here below [39]. Figure 3 depicts the force balance required at any point within the body of a nozzle type vibrating system. Assuming the Young's modulus of the material is  $E$ , density of the material system is  $\rho$ , that the area of the section is  $A$ , the force balance for

force  $F$  could be reduced to yield a one dimensional wave equation solvable for the displacement  $Y(x,t)$  as a function of position  $x$  and time  $t$ . In Figure 3, the slice  $\Delta x$  of an area of arbitrary cross section is considered. The net force acting on that slice and the resulting stresses  $\sigma(x, t)$  could then be computed as

$$F_{net} = F(x + \Delta x, t) - F(x, t) \quad (1)$$

$$\sigma(x, t) = \frac{F(x, t)}{A(x, t)} \quad (2)$$

$$\sigma(x + \Delta x, t) = \frac{F(x + \Delta x, t)}{A(x + \Delta x, t)} \quad (3)$$

The stresses can also be written in the form of the displacement gradient or the strain:

$$\sigma(x, t) = E \frac{\partial Y(x, t)}{\partial x} \quad (4)$$

$$\sigma(x + \Delta x, t) = E \frac{\partial Y(x + \Delta x, t)}{\partial x} \quad (5)$$

The forces can be rewritten in terms of the stresses and they are as follows

$$F(x, t) = E A(x) \frac{\partial Y(x, t)}{\partial x} \quad (6)$$

$$F(x + \Delta x, t) = E A(x + \Delta x) \frac{\partial Y(x + \Delta x, t)}{\partial x} \quad (7)$$

$$F_{net} = \rho \Delta x A_{av} \frac{\partial^2 Y(x, t)}{\partial t^2} \quad (8)$$



Equation 8 has the area as  $A_{av}$  or average cross sectional area representing the entire nozzle body under consideration. Substituting (6), (7) and (8) back into (1) setting the limits of the slice  $\Delta x$  to zero on both sides of the equation:

$$\frac{E \left( \frac{A(x+\Delta x) \partial Y(x+\Delta x, t)}{\partial x} - A(x) \frac{\partial Y(x, t)}{\partial x} \right)}{\Delta x} = \frac{\rho A_{av} \partial^2 Y(x, t)}{\partial t^2}$$

$$E \left( \frac{\partial}{\partial x} \left( \frac{A(x) \partial Y(x, t)}{\partial x} \right) \right) = \frac{\rho A(x) \partial^2 Y(x, t)}{\partial t^2} \quad (9)$$

Equation (9) is the 1D wave equation and it forms the basis for describing the longitudinal displacements generated in an ultrasonic nozzle. The standing waves generated in a nozzle travel through material and geometric discontinuities. The antinodes are at locations where neither one of the above mentioned discontinuities occur. The general solution describing the displacement of the longitudinal wave takes the form of:

$$Y(x, t) = Y(x) e^{-i\omega t} \quad (10)$$

Thus the problem is split in to a temporal and time-dependent part. The temporal part of the solution could be obtained by applying the 1D wave equation (10) to each portion of a nozzle system. Substituting (10) in (9) of the wave equation and differentiating:

$$\left( \frac{e^{-i\omega t} \partial}{\partial x} \left( \frac{A(x) \partial Y(x)}{\partial x} \right) \right) = \frac{\rho \omega^2}{E} A(x) Y(x) \quad (11)$$

The displacement solution for the nozzle will take a form depending on the area of the nozzle section. In general the solution for a constant cross section is a sum of cosines and sines as below.

$$Y(x) = A' \sin k_1 x + B' \cos k_2 x \quad (12)$$

Where  $A'$ ,  $k_1$  and  $B'$ ,  $k_2$  are arbitrary constants whose values depend on the boundary conditions. The boundary conditions of the problem are posed in the form of forces and displacements at the nozzle boundaries of interest. These conditions could also be expressed in the form of energies and displacement gradients. There are two specific conditions that are considered to be important. One where the areas are constant and the materials are different across the boundary. The second where the material across the boundary is the same but the areas are different. In such a case, the ratio of the wave displacements across a boundary for two nozzle sections will be equal to the reciprocal of the ratio of squares of their diameters. This yields the gain factor which seeks to amplify the displacement value at the end of the nozzle tip.

In addition to the above discussion, another critical point to keep in mind is that the length of the nozzle dictates the frequency of operation. They have an inverse relationship with longer nozzles operating at lower frequencies and vice versa. Also from a practical standpoint, even at one operating frequency, nozzles that produce full wavelength ( $\lambda$ ), half wavelength ( $\lambda/2$ ) and quarter wavelength ( $\lambda/4$ ) sound waves exist. In such cases, the overall length of the nozzle is  $\lambda$ ,  $\lambda/2$  or  $\lambda/4$ . The necessity or choice of one over the other typically involves issues related to through put, productivity and specific application based necessities. As far as atomization is concerned, the shape of

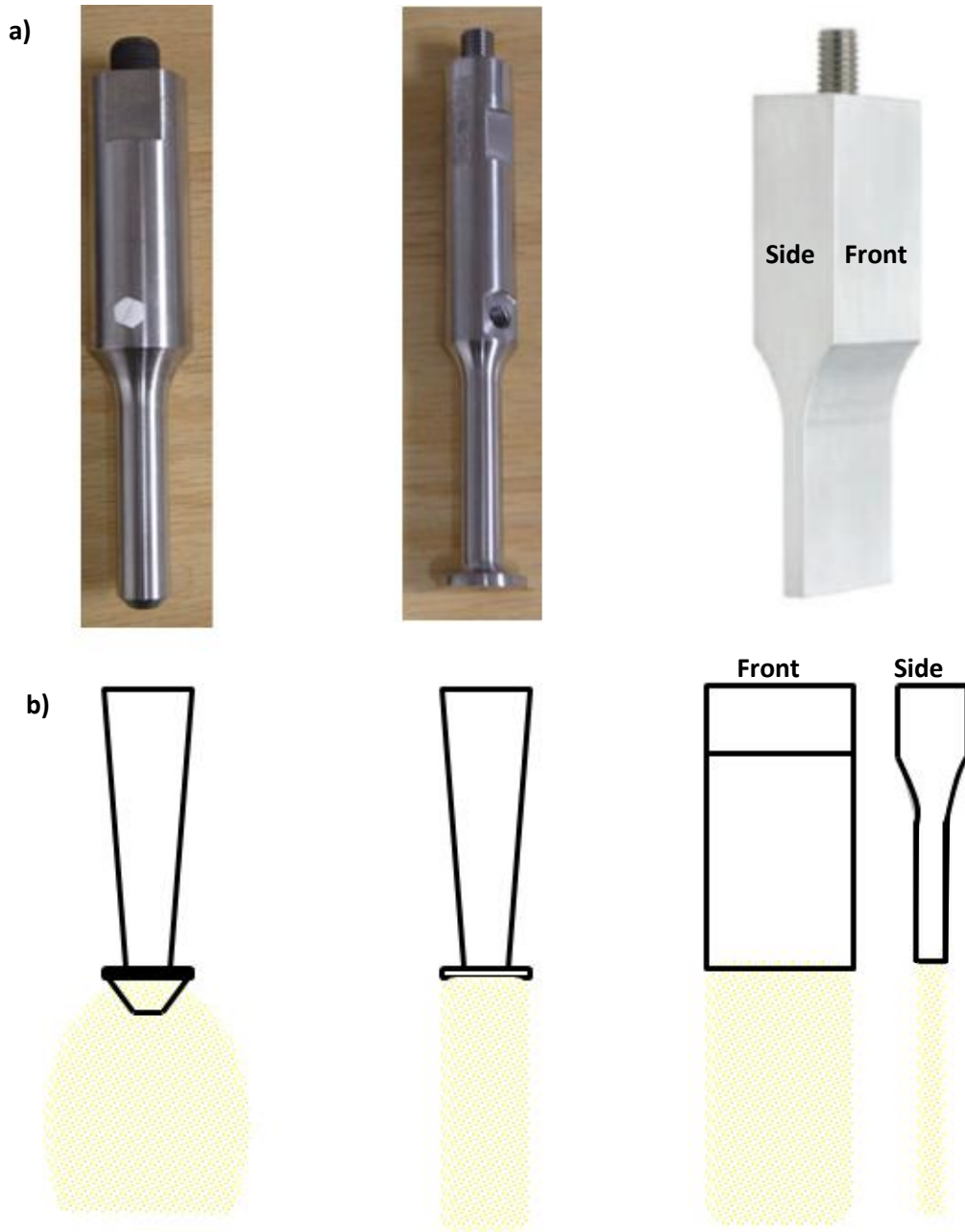


**Figure 4** a) the conical profiled, flat faced and wide dispersion atomizing probes are shown here. Different nozzle tip profiles provide for a way to control the shape/extent of the final spray pattern. b) The spray shapes possible with these probes are shown here. The last two spray patterns to the right are side and front views of the wide dispersion nozzle.

the spray generated can be easily tuned by changing the tip geometry. There are nozzles with a flat tips, wide dispersion tips [40] and 45° chamfered conical profiled tip. These spray shapes and example nozzle images have been shown in Figure 4. The shape of the spray determines the width/level of droplet-droplet interactions that occur prior to coalescence and deposition. The frequency of operation varies inversely with the droplet diameter. At a particular frequency for a specific nozzle geometry type, the flow rate of the liquid being supplied crucially determines the efficiency of the spray process. Spray efficiency can be viewed as the ratio of volume of liquid fully atomized by the nozzle to the total supplied volume. As a matter of fact, the type of pumping system used also influences the quality of atomization. Pumps that pulse heavily such as peristaltic pumps do not help the cause. Instead, linearly driven syringe pumps/gear pumps/manually operated syringe pumps produce a stable low velocity spray. However, manually operated pumps do not offer the precision that spray atomization studies demand. From our previous discussion on the displacement maxima that occurs at the nozzle tip, it is obvious that the physicochemical properties of the fluid would determine the critical displacement at which atomization occurs. These physicochemical properties include surface tension, viscosity and density. Most nozzles have a definite upper limit for these properties beyond which it becomes practically impossible to maintain stability of the driving piezo leading to overloading.

Maximum displacement or amplitude boundary conditions at the nozzle tip are typically achieved via the supply of a set amount of energy (power) to the nozzle. Because of this reason, the words ‘power amplitude’ and ‘amplitude’ are often interchangeably used in this field. Also one related issue is the topic of internal heat generation within the probe.

As the probe vibrates longitudinally, some of the energy is lost to viscous heat dissipation (liquid/probe contact, support bearings). So the rest of the energy over time manifests itself in the form of heating the material of the probe itself (usually Ti-6-Al-V alloy). In such cases, special cooling arrangements are required to reduce the chances of fracture of the probe material due to thermal stresses [39].

One other physical property of the liquid to be considered is its boiling point. If the internal heat generated by the nozzle approaches the energy required for volatilization of the solvent, the process will not function and the spray nozzle will clog with the material chemically dissolved or physically suspended in the solvent. Thus the parameters of frequency, amplitude (energy supplied at a set power), the spray tip geometry, the physicochemical properties of the liquid, temperature of the spray (in relation to solvent boiling point) and the liquid flow rate are all important discrete variables that control the spray characteristics.

#### **2.4 Definitions, Mechanisms and Droplet Characteristics**

The process of ultrasonic atomization simply refers to the disruption of a thin film of liquid by capillary waves set up within the liquid. Capillary waves are shear waves that travel on the surface of the liquid. The source of the capillary waves are the  $\geq 20$  kHz ultrasonic waves travelling parallel to the nozzle axis. The crests and troughs created on the surface of the liquid are due to these capillary waves. The creation of the spray is due to the capillary wave amplitude exceeding a threshold value. In other words, ultrasonic atomization works on the fundamental mechanism of instabilities created in a fluid by longitudinal acoustic standing waves. One view of this instability created in the fluid is

purely ascribed to the most dominant capillary wave destroying the sheet or liquid film stability [41]. The other view of the same instability is to consider the spray formation to be occurring due to high energy/high intensity cavitation bubbles.

In the case of the capillary wave hypothesis, a lot of the theoretical/experimental investigations are based on the initial work done by Lord Rayleigh [41] at the beginning of the industrial revolution. Rayleigh developed an understanding of the conditions necessary for a quiescent column of liquid (with diameter  $a$ ) to split into fine smaller droplets. As it is completely obvious from the previous discussion on wave motion in an ultrasonic transducer, there must exist a maximum of the wave displacement  $Y$  expressed as a function of sum of exponentials  $e^{qt}$ .

$$Y(x, t) = f(x)[f(e^{q_1 t}) + f(e^{q_2 t}) + \dots] \quad (13)$$

The derivative of this displacement function was equated to zero and the condition for the maxima obtained.

$$q^2 = \frac{T_1 (1 - k^2 a^2) \cdot ika \cdot J'_0(ika)}{\rho a^3 J_0(ika)} = 0 \quad (14)$$

Here  $T_1$  is the cohesive tension term,  $q$  is the generalized exponent of the successive terms in the displacement function  $Y$ .  $J_0$  is the Bessel's function and the primed term is the derivative,  $a$  is the jet diameter and  $k=2\pi/\lambda$  the wave-number and  $\rho$  the fluid density. For complete disruption, he showed that the wavelength of a perturbation  $\lambda$  should be at least 4.5 times the diameter of the quiescent column of liquid [41]. Taylor [42] followed up on this work and derived expressions for the upper and bottom surfaces of a horizontal

liquid sheet of thickness  $h$ . Assuming that the bottom surface is flat initially, the expression for the displacement was obtained and further he stated that the thickness of the sheet of liquid should be less than one third of the wavelength promoting the instability. This is generally known as the condition for Taylor's instability. The expressions are summarized as follows:

$$Y_U = \alpha_0 \left\{ \frac{\text{Cosh}nt - e^{-2kh} \cos nt}{1 - e^{-2kh}} \right\} \text{Cos } kx \quad (15)$$

$$Y_L = \alpha_0 \left\{ \frac{\text{Cosh}nt - \cos nt}{1 - e^{-2kh}} \right\} e^{-kh} \text{Cos } kx \quad (16)$$

$\alpha_0$  is the wave amplitude,  $n$  the count of the time instant  $t$ ,  $h$  the film thickness,  $k$  was the wavenumber and  $Y_U$  and  $Y_L$  the upper, lower displacements of the sheet. The validity of the expressions was experimentally verified by Lewis [43] with the help of an elaborate experimental set-up. The set-up was equipped with a drum type camera to observe the interface between different Newtonian test liquids via shadow photography. Lewis observed some interesting phenomena when the air generated downward acceleration was increased. The amplitude of the initial paddle induced wave disturbance was amplified by the air. "Rounded columns of liquid" (or cavities) separated by sheets (or ligaments) were photographically recorded by the drum camera. Thus there was a transition from a capillary wave to a full cavitation type behavior when certain wave amplitudes were exceeded. Mathematically, for a case where the fluid thickness  $h$  is small compared to the wavelength, the amplification factor  $Y/Y_0$  should be a function of fluid densities ( $\rho_1$ ,  $\rho_2$ ), wave number  $k$ , initial wave amplitude  $Y_0$ , time  $t$  and downward acceleration  $g_1$ .

$$\frac{Y}{Y_0} = \text{Cosh} \left( k (g - g_1) \frac{(\rho_2 - \rho_1)}{(\rho_2 + \rho_1)} \right)^{\frac{1}{2}} \quad (17)$$

Dombrowski and Fraser [44] applied some of the findings of Rayleigh in investigating pressure actuated swirl jet atomizers of several geometric types. They evaluated spray patterns and determined the influence of physicochemical properties on the formation of sprays. Whilst the source of the disturbance causing the liquid instabilities was air, their discussion of the amplified wave destabilizing the liquid sheets was very relevant to the current topic. Liquids with low surface tension, low viscosity and low density were the easiest to atomize. In contrast, liquids with high surface tension, high viscosity and low density resulted in the formation of docile sheets that did not disintegrate near the edge. With high surface tension, test liquids tended to move inward resulting in the formation of a fine jet completely impeding the formation of threads/ligaments/drops [44]. Typically in such a case, an increase in the supply pressure (energy) was required to cause the spray formation. The influence of viscosity could be seen more as a factor that stabilizes the edge of the spray while density seemed to have no appreciable effect in liquids with approximately similar surface tensions [44]. Also, there was evidence to indicate that air pressure actually caused the amplification of wave like disturbances that exist on the liquid sheet.

Around the same time, Antonevich [45] in his seminal work employed a 20 kHz ultrasound device showing that the cavitation (due to weak spots) and the resulting droplet formation phenomena occurred in three distinct phases. One was quite degassing (low amplitude), second was resonant bubble formation (due to coalesced bubbles reaching the resonant frequency of the applied sound field) and third was nonlinear



bubble growth (caused in a situation where the sound field amplitude is so high that the liquid vaporizes instantly and forms vapor filled cavities causing the cavity to push inward on the gas or vapor resulting in an implosion). The final spray produced to the naked eye however seemed like a continuous stream of fluid droplets forming with occasional ligaments or thread of fluid droplets. In reality, this is a case of cavitation caused by intense pressure drop in the bulk liquid resulting in implosions within the fluid [45]. However there are also non-collapsing bubbles formed that coalesce and form the larger bubbles that are visible to the naked eye. Further the effect of the supplied acoustic field frequency is such that the droplet diameters go down in dimension.

Willard [46] observed similar phenomena in his unique work with a spherically focusing ultrasonic radiator operating at 2.8 MHz. He asserted that the ‘plume’ of the droplet containing spray was a fine mist of “microcavities too close” and “too small” to make a distinction. Further, he measured the time scale of the entire process from beginning to end to be several 100 milliseconds long. He also stated that the whole process occurred due to a random movement of weak spots/nuclei within the fluid where the fluid perturbation would initiate and build-up leading to a final fluid break-up [46]. His experiments delineated the cavitation process into discrete steps of microcavity formation, catastrophic plume formation and in the case of aerated liquids, bubble formation. The formation of the bubbles was almost always followed by a downward liquid streaming.

Lang [47] carried the work forward to the next step where he experimentally arrived at a relationship between the wavelength of the capillary wave, the size of the droplets

produced, the operating probe frequency and the fundamental liquid properties. The basis for his work was the Kelvin's equation shown below

$$\lambda^3 = \left( \frac{2\pi\sigma}{\rho f^2} \right) \quad (18)$$

Where:  $\lambda$  is the capillary wave-length in m;  $\sigma$  is the surface tension in N/m;  $\rho$  is the fluid density in  $\text{Kgm}^{-3}$ ;  $f$  is the surface capillary wave frequency in Hz (1/s). Also  $f=F/2$  Hz where  $F$  is the probe operating frequency in Hz

Lang used castor oil, synthetic wax under low flow rate of 0.6 ml/min and probe frequencies ranging between 10-80 kHz to obtain his direct equation relating droplet median diameter shown below in [47]. At each operating frequencies, he used photomicrographs powered by a mercury flash lamp to measure surface capillary wavelengths and droplet diameters. He observed that there was a droplet diameter distribution prevalent at each frequency of operation and that 90% of the droplet diameters were below twice the median diameter in the distribution. His equation under such assumptions provided an empirical relationship between the median droplet diameter ( $d_{median}$ ), the probe frequency and the liquid properties [47].

$$d_{median} = 0.34 \lambda = 0.34 \sqrt[3]{\frac{8\pi\sigma}{\rho f^2}} \quad (19)$$

Charles and Mason [48] studied the nature of droplet formation, rupture/coalescence for the specific case of liquid-liquid interfaces. Experimental measurements of droplet formation and times of rupture were recorded using a high speed camera. They theoretically determined the relationship between the contact surface diameter  $c$  (assumed

to be a flat disc) initial droplet diameter  $b$  and fluid physicochemical properties. They have concluded that once the droplet lands on liquid phase-2, the full rupture (and hence stability) was dependent on the initial droplet diameter, the temperature, nature of the surface, surfactant presence, electrocapillarity and viscosity. Also the stability decreased with decreasing diameters of the droplets and rupture of the droplet and coalescence initiated at more than one point. An important expression derived for the droplet diameter by these authors has been shown in Equation (20). The term  $c$  in the equation refers to the diameter of the flat interface near the droplet plane (droplet impression diameter), while  $\Delta\rho$  is the difference in density between the liquid and air,  $\sigma$  is the surface tension and  $g$  is acceleration due to gravity.

$$c = 4d_{median}^2 \left( \frac{2\Delta\rho g}{3\sigma} \right)^{1/2} \quad (20)$$

Hinze [49] later organized much of this early literature on droplet rupture and posited on the types of deformation shapes, flow fields and relationships between various physicochemical properties. He proposed that fundamental droplet break-up could be either due to the influence of dynamic forces acting on the droplet or the viscous stresses acting on them. For this reason, he suggested the ratio of the Weber (ratio of inertial to surface tension forces) to viscous number (ratio of viscosity to surface tension forces) be used as a quantity for evaluating droplet break-up regimes. Specifically, he described droplet break-up in a viscous flow, in air and that under isotropic turbulence (as in emulsion manufacturing). In each case, not only were the droplet break-up mechanisms different but also showed different relationships between the ratio (of Weber to viscous numbers) and fluid properties. Specifically, Hinze stated that each droplet splitting or

spraying process had its own Weber to viscous number relationship uniquely defined by the mode of spraying or ‘dispersion’.

For ultrasonically atomized sprays, Peskin and Rako [50] examined these relations by performing a linear stability analysis of the problem. They incorporated the fluid film thickness, ultrasonic wave velocity terms at the transducer surface into the already existing droplet diameter relationship that Lang had developed. They defined a 2D plane with a film of liquid present on the surface subject to perturbations. Assuming viscosity to be negligent, and the amplitude to be low, they theorized that capillary wave disturbances produced had wavelengths that were of the same order of magnitude as the drops produced [50]. Further they also stated that multiple capillary waves of different wavelengths could exist at any point of time and the most dominant or “violent” of the waves create the spray in the form of a “projection”. This final equation is stated here below in (21). It is to be noted that for large amplitudes, this relationship approximates to Lang’s relationship.

$$\frac{d_{median}}{\pi a} = \left\{ \left( \frac{8\sigma}{\rho Y_0^3 f^2} \right)^2 \tanh \left( \frac{\pi Y_0}{d_{median}} \right) \left( \frac{h}{Y} \right) \right\}^{\frac{1}{3}} \quad (21)$$

Here  $h$  is the liquid film thickness on the vibrating surface. All other terms have been defined while describing other equations.

The sole focus of more recent works from researchers in this field has been on building empirical relationships between droplet diameter, frequency of operation, flow rate and viscosity for liquids of different types [51, 52]. Avaru et al. explored the cavitation phenomenon by using a potassium iodide (KI) solution and atomizing it over several

periods of time. They noticed via UV-visible spectroscopy that the amount of iodine released increased providing evidence of cavitation phenomena initiating a chemical reaction [51]. Rajan and Pandit [52] performed experiments on sodium chloride solutions of different weight percents to ultimately arrive at modified non dimensional Weber, Ohnserge or viscous numbers incorporating the ultrasonic probe frequency in to the terms. Their work showed that droplet diameter distributions tended to vary across specific ranges or values of these numbers.

Thus these significant contributions show a very delicate relationship between the fluid properties, frequency of operation and capillary surface wavelength. These factors can be controlled to obtain useful engineering applications of different types.

## **2.5 Influence of Liquid Physicochemical Properties on Ultrasonic Atomization**

All published research on ultrasonic atomization pointed to a direct relationship between spray droplet diameter and the surface tension, density and viscosity of the liquid being atomized. Thus for each test liquid, the amount of supply energy required for full atomization was influenced by these properties.

Generally, viscosity tends to stabilize the most frequent instability increasing the energy required for spray creation and leading to larger droplets. While capillary waves travelling through a Newtonian liquid do not have the capability to break bonds, the same is not true for Non-Newtonian liquids such as polymer solutions. With increasing viscosity, the dissolved phase (polymer in this case) can undergo sonic degradation [36, 51]. Such effects have not been investigated in a systematic fashion for ultrasonic sprays. This was especially true of block copolymer solutions as the properties/microstructures of

the resulting solid film could be controlled by varying the energies/times of exposure to the atomization energy source. One fundamental question is whether the ultrasonic energy causes degradation.

Almost all reported research have studied the nature of the sprays generated but did not investigate the use of the technology in aiding any relevant applications. Some of these applications as mentioned before in the introductory chapter are fields of high importance such as solar cells, dielectric thin film generators, and artificial muscle, lithium-ion battery coatings and carbon nanotube coatings on polymer composites. Almost always, the use of a new technology for a particular application generates certain specific requirements. These requirements together with discussion on a film deposition system are furnished in the following two sections.

## **2.6 Deposition Parameters of Interest as applied to Thin Polymer Films**

The initial state of the precursor solution such as polymer content and the solvent properties (surface tension, vapor pressure) used for preparing the solution plays a crucial role in shaping the physical properties of the solution. Cavitation and capillary wave phenomena are completely different for dilute, semi-dilute and concentrated solutions of polymers in the same solvent. In addition the mode of delivery of the solution to the nozzle tip, the air flow conditions surrounding the nozzle as the spray gets generated, the temperature of the environment and the state of the substrate (clean vs. dirty) all control the deposition. The nozzle frequency (hence nozzle dimensions), amplitude of vibrations and also the nozzle tip geometry control the state of the deposition. In particular the air-flow conditions as evident from the literature review play a critical role in

sustaining/amplifying the capillary wave activity; intuitively it can also be made to target the droplets in a specific direction.

Not all of these parameters have been controlled carefully in studies involving ultrasonic nozzles for thin polymer film processing. Some investigations have hoped to ‘blindly’ improve properties of their respective materials of interest without actually understanding what it is that ultrasound does. The uniqueness of ultrasonic sprays is its ability to create mono-disperse droplet diameter distributions with a comparatively low energy usage. If all other parameters are considered accurate and repeatable, the accuracy and precision of the droplet generation was only a function of the piezoelectric transducer vibrations. In other words, the state of the spray as it reached the substrate should reflect this precision. i.e. the collection of the spray should be done in a manner where the spray does not end-up becoming a ‘pool’ of liquid. Some precise guidance for the sprays to uniformly reach an intended target substrate is required for the success of the deposition. Obviously droplet drying should also be incorporated into this sequence. No thoughts on such aspects of deposition have been documented by researchers to my knowledge. Such insight would lead to a quicker application of this technique to other coating, film processing and material synthesis applications.

## **2.7 Practical Implementation of a Deposition System**

Very few researchers have reported the use of isolated chambers for investigations employing ultrasonic nozzles. While there could be a concern about viscous heat dissipation at the surface where the atomizing probe contacts the chamber, the positives of isolating the spray far outweigh the negatives. In fact almost all of the film deposition

systems outlined in the introductory chapter (see Table-1) have been achieved in isolated chambers.

The substrate temperature/temperature of the deposit has not been carefully maintained in any published works. While this might seem trivial for a spray technologist who examines the spray from a fluid mechanics point of view, the substrate temperature critically affects the properties of the deposit. Also, as mentioned in the previous section, reports into the uniform coverage of the substrate by the spray has been lacking in metrics. Conveyor belt and air-assisted mechanisms have been reported for uniform coverage/targeting, but the degree to which they were repeatable was not reported. Also not considered was the influence of the air pressure of the air-assist mechanisms and the distance between the nozzle-tip and the air pressure draft mechanisms on the state of the spray.

## **2.8 Key Research Questions I**

### **2.8.1 How Do The Independent Variables Affect Droplet Formation and What Is The Relationship Between These Variables And The Final Droplet Diameter?**

Physically, each and every droplet possessed a certain initial velocity and was acted upon by drag force, gravity and surface tension. The nature of the liquid's physical properties (density, surface tension and viscosity) controlled the minimum energy needed for atomization and hence its initial velocity. These physical properties together with the flow-rate, energy of atomization constitute the *independent variables* of the process. This in turn influenced the drag force and droplet-droplet interactions.



In order to answer the posed question, the *median droplet diameter* measurements have to be performed as a function of the independent variables. Droplets or collections of droplets would have to be collected and quantified via microstructural analysis. Finally, a relationship could then be shown between the process parameters and the median droplet diameter. This would theoretically provide the basis for varying properties of the spray to obtain droplet diameters of a required size for other viscoelastic systems.

### **2.8.2 Was There A Distribution In The Droplets That Were Generated And If These Distributions Were Solution Weight Percent Dependent?**

The amount of energy invested in creating a solution droplet is dependent on the amount of polymer dissolved in the solvent. If there was a distribution in the droplet sizes, it would imply droplet deformation/rupturing over several size scales. There could also be coalescence followed by droplet rupture. That being said, the question posed here could again be easily answered from the microstructural analysis of the collected droplets.

### **2.8.3 How Can One Obtain Uniform Thin Polyurethane Films Via an Efficient UA Whilst Also Reducing Process Time, Obtaining Energy/Material Savings?**

One of the primary requirements for spray generation was the development of a thin liquid film on the tip of the nozzle. As discussed earlier, spray formation then occurs due to the wave amplitude exceeding the threshold minimum. Once the spray was generated, depending on the liquid properties, there was a definite amount of disorder in the spray paths. This inconsistency in the path was due to the low flow rates being used and varying air flow conditions around the nozzle. Low flow rates in our process provided us with sufficient times for drying of the deposited solution. High flow rates typically

provided a solid spray but the times required for drying were large. For this reason, low flow rates were necessary to investigate UA. In this framework, in order to answer the question posed here, the spray generation and film formation processes could be coupled together using an *air-draft* at low pressure (approx. 7 kPa).

The air-draft would thus be introduced as a way to target the trajectory of the droplets and the spray in general in consistent directions. In order to understand the influence of the air-draft on the efficiency of UA, energy/material savings; specific experiments would be conducted with and without using the air-draft. Comparisons would be made with the popular spin coating method as well.

#### **2.8.4 Which Independent Variable/Sets of Independent Variables Affect The Microstructure/Properties The Most And Why/Why Not?**

Film microstructures generated at different flow rates (same temperature, energy of atomization), could potentially be different and also have varied properties. The same is true for deposition temperature. In essence, the drying of droplets (including presence of residual solvent) would be controlled by varying these parameters.

The answers to the question posed here would be obtained by a combination of *optical microstructural/mechanical property and physical property measurements* (such as material thermal transitions, X-ray scattering and Atomic Force Microscopy). For more details on these material properties, refer to the research questions at the end of chapter 3 (section 3.4). With the influences of these parameters interpreted, a *schematic of the mechanism of the deposition process and film formation* will then be suggested.

## Chapter 3.

### THERMOPLASTIC POLYURETHANES (TPU)

#### 3.1 Basic Terminology, Definitions and Fundamental Chemical Structures

Thermoplastic Poly Urethanes are block co-polymers with a -(H-H-H-S-S-S)- type microstructure. H stands for Hard and S stands for Soft. Specifically they possess the urethane group (-NHCO-O-) throughout their structure. The fundamental building blocks or the monomers are isocyanates (RNCO) and polyols (HO-----OH) along with chain extenders ROH where R is an alkyl/aromatic group. The reaction between the isocyanates and the polyols result in a prepolymer that is further reacted with the chain extender to get the polyurethane polymer. The structure of an elastomeric polyurethane material is given by: -(NHCO-O-R-NHCO)-. This chemical structure of the final polymer is made up of thermodynamically incompatible higher molecular weight H or Hard-Segment (isocyanate/chain extender part) and the lower molecular weight S or Soft-Segment (polyol part) [53]. Often times, the hard and soft segment phases tend to form different microphase separated domains within the material depending upon polymer synthesis method, ratio of isocyanate to polyols, sample fabrication and test conditions. The terms segment, domain and phase have very strict meanings and hence have to be defined carefully before the discussion on structure-property relationships. Segment may refer to a set of single chains of either the H or S types. Domain may refer to a continuous/discrete portion of several segments of the H or S type. The domains of the H or S type together constitute H or S phase of the material. A schematic has been shown in Figure 5. Because of this nature of the microstructure they are high strain materials and are a class of dielectric elastomers.

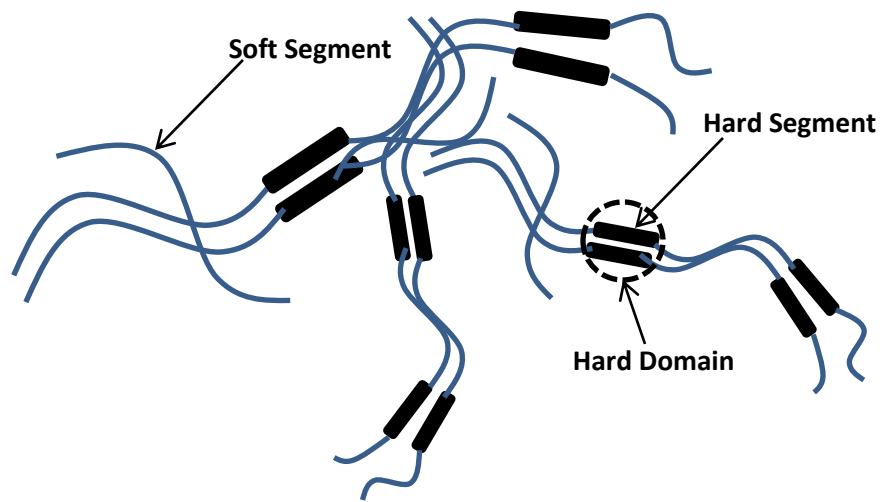


**Figure 5** Typical two-phase microstructure of a TPU copolymer has been shown here. The soft (S) and the hard (H) segments are thermodynamically incompatible and form aggregate domains of S and H segments. This results in the development of an S and H phase within the microstructure. The S phase is a matrix of S domains while the H phase acts as reinforcements.

### **3.2 TPU Material Mechanical Behavior and Microstructural States of Hard/Soft Domains**

Some of the earliest trend-setting works on this material date back to the late 1950s. Cooper and Tobolsky investigated two elastomeric estane polyurethanes with varying MDI or dimethyl diphenylisocyanate contents. While the MDI constituted the hard segment H part of the polymer, the polyester formed from a reaction of adipic acid and 1,4-butane diol was the S-part. The chain extender was 1,4-butanediol. Their significant contribution was to determine why or how post glass transition, the material showed high modulus values in the rubbery plateau region. They determined that these block copolymers have different responses (even curve shapes) as a function of temperature through Dynamic Mechanical Analysis (DMA) for different levels of one monomer [54].

Because of the unique structure the elastomeric estane polyurethanes were exhibiting, they determined that the modified William Landel Ferry (WLF) equation does not fit the responses in the rubbery plateau region. Finally they performed temperature sweep experiments on plasticized samples and came to the conclusion that different plasticizers preferentially solvated either the MDI or the polyester part of the polymer. They were the first to postulate that MDI units were acting as hard blocks in improving the post T<sub>g</sub> response near the rubbery plateau region. The first glass transition was between -50°C to 0°C while the second was at 120°C [54].

Clough and Schneider carried out studies on similar estane type polymers. In addition, they also considered a polyether-MDI block copolymer and a polybutyleneadipate (PBA)-MDI copolymer. They performed thermomechanical analysis, differential

scanning calorimetry (DSC) and polarized light scattering. They measured transitions T1 (sub-ambient  $T_g \sim -50^\circ\text{C}$ ), T2 ( $T_g$  above ambient  $\sim 20-45^\circ\text{C}$ ) T3 (High temperature  $T_g \sim 100-120^\circ\text{C}$ ) and T4 (melt transition  $\sim 200-210^\circ\text{C}$ ). They mention that the reversible elasticity mechanism was due to the post  $T_g$  onset of flexibility in the soft segment polyether or polyester segments [55]. The high modulus behavior in the rubbery plateau region was due to the presence of hydrogen-bonds linking the hard and soft segments. At higher temperatures close to T3, these bonds are very weak. These hydrogen-bonds are between ester molecules in a polyester PU and between urethane domains/urethane-ether in polyether urethane sample [55].

A large majority of workers have since then focused on understanding the H and S segment domain sizes and the way they behave during deformation. Wilkes and Yusek worked on studying small angle x-ray scattering (SAXS), wide angle x-ray scattering patterns and DSC. They found that H-segments continuously change their arrangements under stress resulting in oriented domains with large tensile strengths. [56]. Koberstein and Russell characterized block copolymers of MDI-oxyacetylene/end capped polypropylene. With increasing amounts of H-segment present, the transition temperatures T3 and T4 were higher which suggested mixing of the non-crystalline H and S segments [57].

Harrell in his work on segmented urethanes varied segment size distributions, sizes, and chain spacings. He stated that the narrower size distributions of hard segments caused the stress at a particular strain to increase. Similarly the narrowness of the soft segment size distribution increases the tensile strength and strain to failure. Narrow size distributions for both H and S segments provided the maximum extension set [58].

Recently, Lee et al have performed in situ stretch experiments of thin PU films in a SAXS machine. They determined that for such PU films stretched in such a fashion, the H segment domains follow the deflection of the film up to a point and then break up in to numerous other H domains. In the 90 degree direction, the domains break-up after undergoing shear compression [59].

Finnigan et al. made use of the thermodynamic incompatibility within a Poly(Tetra Methylene oxide)/MDI PU to disperse a clay nanoparticle [60]. The clay Cloisite 30B was dispersed via melt extrusion and through solvent casting. Only stiffness improvements were seen (with the softer PU), but the strength and failure strain decreased. Yamasaki et al. have suggested PU samples be annealed with a view on changing the H-segment domain content. With increase in temperature, the H-segment domain content increased as well. Further strain hardening at one particular temperature was much higher after the annealing step [60].

In a study more relevant to the research described in this thesis, Bisticic et al have manufactured calcium carbonate based TPU nanocomposites and have evaluated mechanical properties of the films in the directions parallel and perpendicular to the plane of the film [61]. Mechanical properties were determined for all samples and the samples were analyzed for evidence of phase separation via infrared spectroscopy. Final film thicknesses were 20-30 microns. The films were dried at room temperature and tested in tension over a gage length of 40 mm at 10mm/min strain rate as well as in a relaxation mode (In strain intervals of 25% to 200%) with the decay measurement being over 1300s. 20x10mm samples were used for infrared dichroism studies on a sample that was manually stretched using an extensor @ 5mm intervals. Spectra were obtained with the

infrared light oriented parallel and perpendicular to the stretch direction and were obtained prior to testing as a reference and once again during the initial part of the test followed by a final measurement after relaxation [61]. Using polarized optical microscope with cross polarizers, spherulites were observed in both neat and nano films but the nano films have smaller spherulitic sizes owing to the presence of a larger number of nucleation sites. A typical stress-strain curve showed a very small linear elastic region followed by yielding and then a cold drawing plateau region followed by a strain hardening region. The strain hardening was more with the neat samples was a direct consequence of spherulite sizes. Concurrent FT-IR data reveals N-H stretching/C=O stretching and other such peaks [61]. It shows H-segments in three populations: free, bonded to other H-segments via hydrogen bonds, bonded to soft segments via hydrogen bonds. Orientation analysis was carried out by determining the dichroism ratio of  $R=A_{\text{parallel}}/A_{\text{perpendicular}}$  in which A is the area of an FT-IR band. The addition of  $\text{CaCO}_3$  seems to not change any phase separation influenced alignment in the longitudinal or transverse samples. But there was a thickness dependence on the observed orientation [61].

### **3.3 Critical TPU Applications**

TPU block copolymer dielectric elastomers have interesting applications. As a dielectric elastomer, these materials have the capability to store charge and hence have applications in the sensor field [16-20]. Use of thin films of TPU by other workers under an electric field to document electrostriction was discussed earlier [16]. The softness of the material together with the biocompatible nature of some versions of the TPU has made researchers label these materials as ideal substitute for muscles [16, 17, 19]. In terms of work



density, strains, and continuous power operation, TPUs are more efficient than the muscle. Other similar applications include biomimetic robots, robotic arms, compliant electrodes, soft actuator tactile display to simulate human touch, dielectric loud speakers, electric power generators [16-20]. Polyurethane is also being used to provide biocompatible coatings to stents for use in the heart [11, 12].

### **3.4 Key Research Questions II**

#### **3.4.1 Do The Capillary Waves Travelling Through The Polymer Solution Influence the Useful Final Mechanical Properties Of The Films? Why? / Why Not?**

Ultrasonic energy manifests itself in the form of high energy cavitation and capillary waves. Typically, with the increase in solution viscosity more energy is invested in setting up the capillary wave motion to maintain the same amplitude. The implication is that while the wave tried to propagate, the viscous nature (due to the size/shape of the dissolved polymer chains) of the solution causes energy to be spent on forming a thin liquid film on the nozzle tip. This means that with different amounts of energies spent, the microstructure could probably change and influence the property responses.

Thus the answer to the question above could be qualitatively inferred by measuring the mechanical property responses of the thin films. Specifically, the mechanical responses of interest include the strength, the strain to failure and the fracture toughness values of the films. Since, the solution liquid properties play a significant role in deciding the capillary wave conditions, the answers to this question will be provided in tandem with the answers to the question posed in 2.8.4.

### **3.4.2 What Was The State Of The H/S Phases In The Material As F (Processing Conditions)? And Do These Trends Match With The Trends In The Mechanical Properties? Why? / Why Not?**

From the review of literature it was clear that the state of the H and the S phases in the microstructure were very delicately dependent on processing and test conditions. As seen in the literature, such studies involve interpretation of datasets from more than one type of measurement in conjunction with each other.

A similar approach will be followed here to attempt to answer this question. These include determination of thermal transitions, X-ray scattering and imaging of phases of the material via Atomic Force Microscopy (AFM). Selected datasets will be analyzed and examined with respect to results published by other workers. A discussion will then be developed to hypothesize how or what set of events during ultrasound atomization / sonication initiate any changes to the microstructure.

## **Chapter 4.**

### **MATERIALS AND METHODS**

#### **4.1 Materials Used**

##### **4.1.1 Polymer System**

A solution grade TPU classified as SG-60D based on the shore hardness was procured from Lubrizol Thermedics [62]. The material has a Hydrogenated Methylene Diphenyl Diisocyanate (HMDI) as the hard segment monomer and PolyTetraMethylene Ether Glycol (PTMEG) as the soft segment with 1,4-butanediol as the chain extender (CE). The material was in the form of pellets and subject to vacuum treatment at 40°C for 10-12 hours upon receipt. Following the treatment, the pellets were stored in an air-tight plastic container.

##### **4.1.2 Solvents Used**

99.5% pure DiMethyl ACetamide (DMAC) (boiling point 170°C) and TetraHydroFuran (THF) (boiling point 60°C) from Cole-Parmer Inc. were used as solvents. While most of the atomization experiments in the work were performed with DMAC, THF was primarily used to fabricate a few samples to check for volatility influences. THF based samples at 2% by weight were also manufactured via casting. For purposes of cleaning the nozzle, syringes and glassware, acetone/isopropyl alcohol was used.

#### **4.2 Polymer Solution Preparation, Solution Properties**

##### **4.2.1 Solution Preparation**

Polymer solutions were prepared at 0.2, 2 and 4 % by weight of solvent. A Cole-Parmer magnetic stirrer/hot-plate was used for this purpose. The dissolution was carried out at 45°C and the times of dissolution varied between 20 minutes to 60 minutes for the three weight percentages. Magnetic stirring was carried out at between 150-170 RPM. Once the solution was prepared, it was allowed to cool down to ambient temperature. Solutions for each set of thin film fabrication trials were consistently maintained between 0-1 day old. Any solution past 1 day was discarded for experimentation because of solvent evaporation. Solutions were stored at temperatures of  $20^{\circ}\text{C} \pm 2^{\circ}\text{C}$

## **4.2.2 Solution Properties**

### **4.2.2.1 Density Measurement**

Solution densities were measured using a graduated 10mL measuring cylinder shown in Figure 6b. For the solutions, the liquids were carefully poured through the sides of the cylinder without causing any bubble formation. Knowing the mass poured into the vial and the vial volume, the solution density was computed. These experiments were also carried out at  $20 \pm 2^{\circ}\text{C}$  on a 0.0001g mass balance.

### **4.2.2.2 Viscosity Measurement**

A falling ball viscometer employing glass and stainless steel balls were used for measurement (Figure 6a) at  $20 \pm 2^{\circ}\text{C}$ . Knowing the density of the test liquids and the density of the ball and the measured time of travel for the precisely machined ball to fall between two reference points, the viscosity could be determined. The equations used for calculating the viscosity were:

$$\mu = Kt(\rho_{ball} - \rho_{fluid}) \quad (22)$$

K was the viscometer constant equal to 0.3, t was the time of travel in minutes and  $\rho_{ball}$  was 8.03 g/cc for steel and 2.5 g/cc for glass. The viscosity was measured in centipoise.

#### 4.2.2.3 Surface Tension Measurement

The surface tension was computed by the pendant drop method (Figure 7a). The contact angle was measured by capturing an image of the drop using a digital camera. An example image has been shown in Figure 7c. Mass of the droplet suspended was measured using the mass balance in the set-up shown in Figure 7a. Knowing the angle of contact, the diameter of the tip D (0.72 mm), the surface tension was determined using the following equation. By substituting for D,  $\pi$  and acceleration due to gravity g, we get the constant 4.33.

$$\gamma = mg/\pi D \sin \alpha = (4.33 m 10^3)/\sin \alpha \quad (23)$$

where m was the mass of the pendant drop in kg.  $\alpha$  was the contact angle in degrees and  $\gamma$  was the surface tension in  $\text{Nm}^{-1}$ .

### 4.3 Thin Film Fabrication

#### 4.3.1 Control Films

DMAC based films of 20 $\mu\text{m}$  target thickness were synthesized on a custom made glass mold about 40mm diameter and heat treated to prevent breakage. The molds had geometrically flat substrates as bottoms with minimal curvature on the surface and near the edges (Figure 8 b-c). A specific amount of solution was poured into the mold.

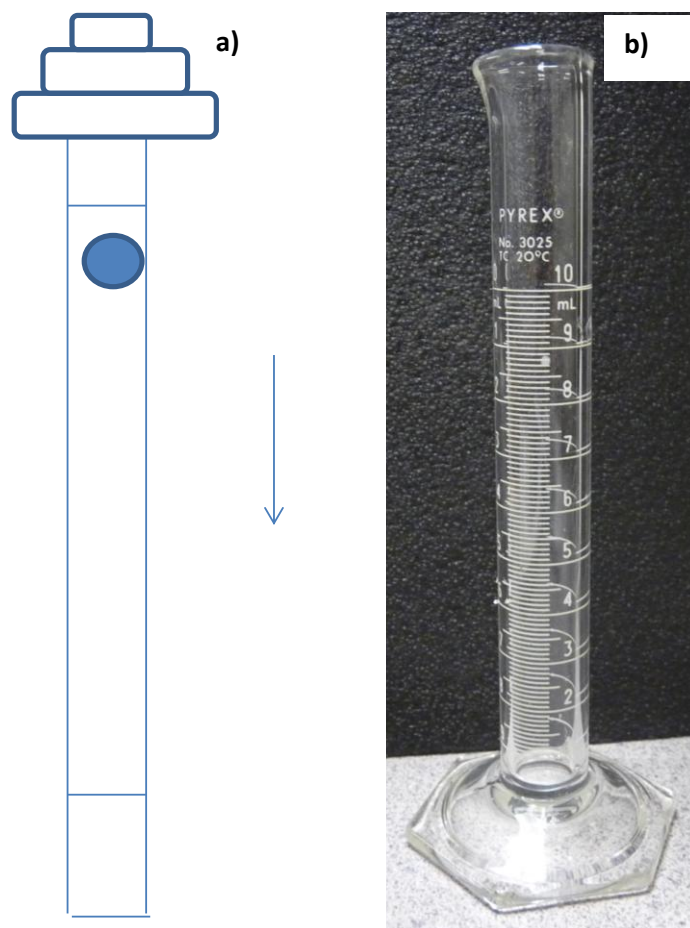


**Figure 6** a) Falling ball viscometry measurements where the time taken by the falling ball in a liquid column to fall (between calibrated lines) is used to measure the viscosity b) Density measurements where the calibrated volume markings are used in conjunction with a 0.0001 g balance for computing density.

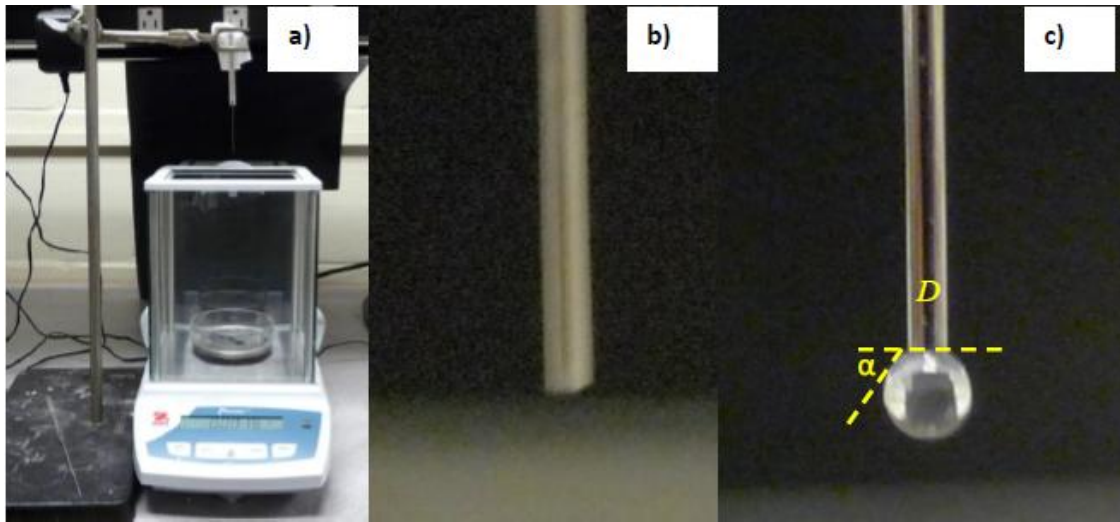


**Figure 7** a) Surface tension measurement set-up, b) Needle tip with no droplet c) Needle tip with water droplet.

THF based films were also fabricated at 2% by weight of TPU and about 2.1g of the solution was required for a 20 $\mu$ m film thickness. Also, this THF solution was subject to ultrasound via bath sonication at time intervals of 30, 60 and 90 minute. This sub study was incorporated on the basis of the observed mechanical properties of atomized THF based TPU films. We were curious if the type of ultrasound energy source (flat bottomed in case of a bath sonicator vs the nozzle tip) affected the properties of the film

### **4.3.2 Ultrasound Atomized Films: Set-Up and Spray Characterization, Film Fabrication Protocols**

#### **4.3.2.1 Set-Up and Spray Characterization**

Figure 9 displays the schematic of the thin film deposition system used in this work for fabricating all atomized films. Figure 10 shows the practical implementation of the concept. A 20 kHz dual inlet atomizing probe interfaced with a 750W CV 033 piezoelectric transducer was mounted onto the top half of a custom made deposition chamber (about 100 mm diameter and 200 mm long) via an especially bored rubber stop.

The chamber temperature was regulated by means of a blanket heater wrapped along the outside walls of the chamber. The thermocouple tracking the temperature of the chamber was placed at the same height as that of the substrate and connected to a Digisense advanced temperature controller which controlled the heater in an AUTO PID mode. The bottom half was the chuck of a spin coater on top of which the substrate was mounted using scotch tape having a maximum temperature rating of about 120°C. The onboard electronics of the spin-coater (maximum speed of 6000 RPM) located below the chuck



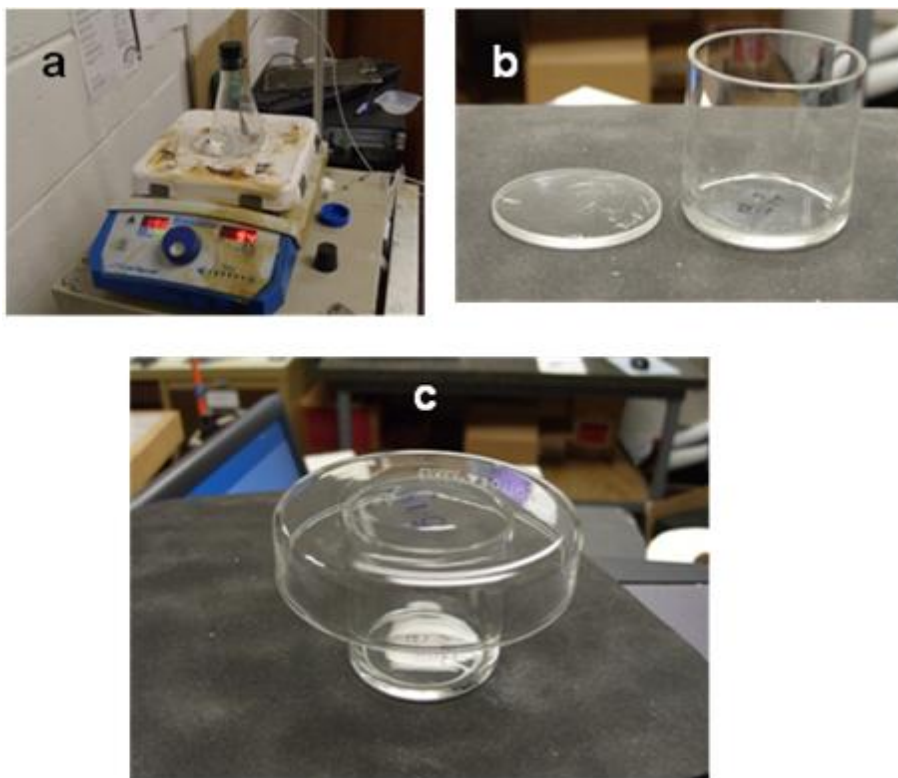


**Figure 8** a) Solution Preparation, b) Glass mold with flat bottom, c) Mold with covered petridish.

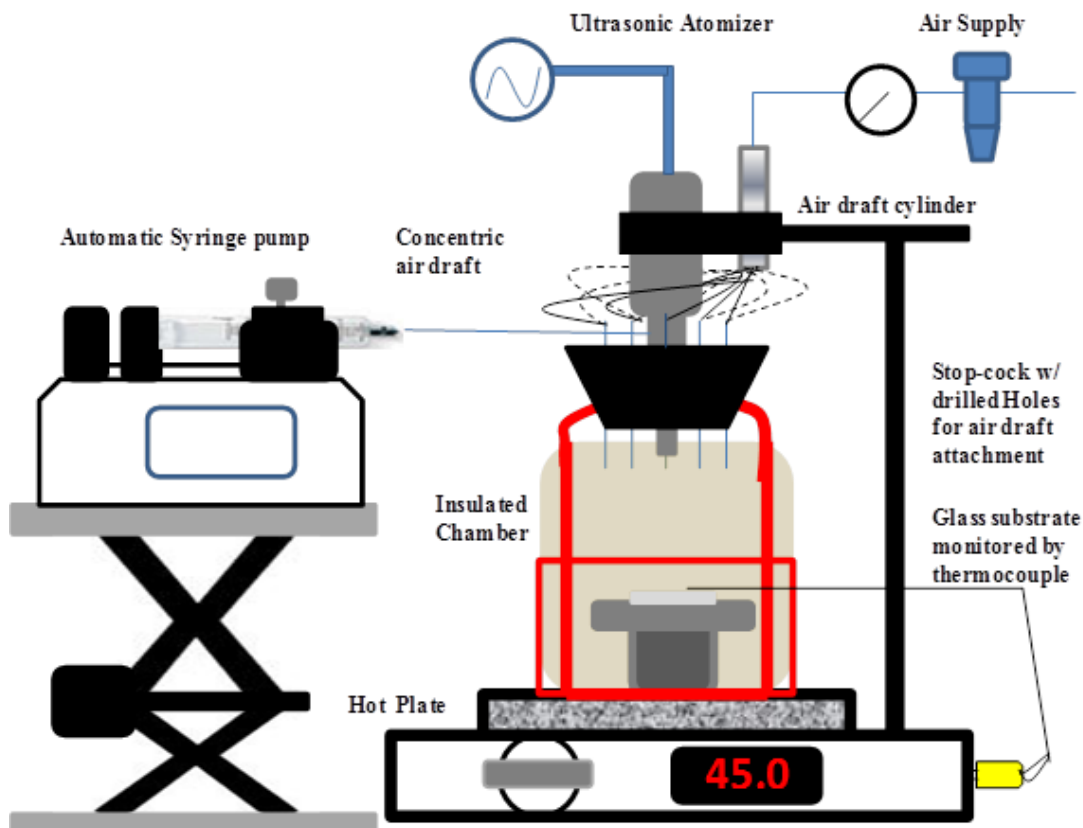


**Figure 9** Schematic of an Ultrasound Assisted (UA) deposition system with substrate mounted on the chuck of the spin coater. A spin-coater essentially works on the principle of centrifugal forces spreading the solution onto the substrate at moderate to high speeds (600-6000 RPM). In our case, the spin-coater is used at a very low speed to just allow for the uniform deposition of the film.

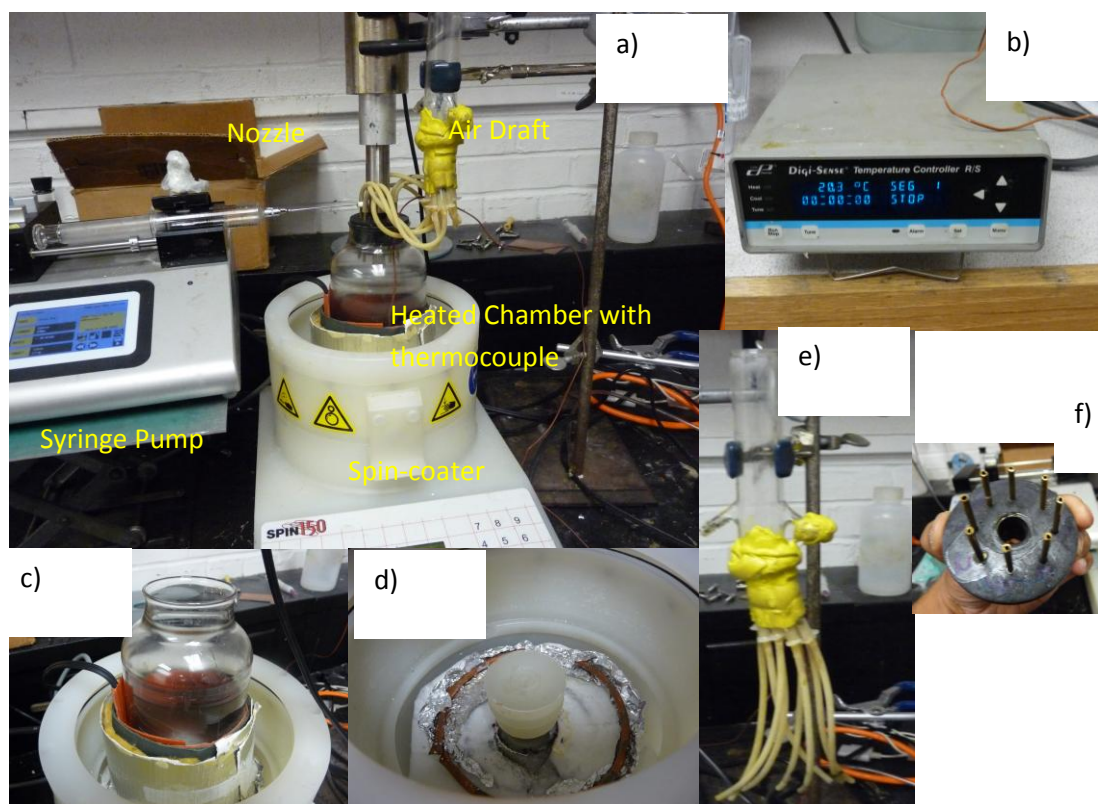


**Figure 10** a) Ultrasound Assisted (UA) deposition system with substrate mounted on the chuck of the spin coater, b) heater temperature controller, c) glass chamber with heat pad, d) substrate on cuck of spin coater, e) air-draft, f) concentric draft attachment.

was protected from the any over-heating of the chamber using up to 12.25 mm of insulation. During the deposition, the chuck carrying a 50 mm x 50 mm square glass substrate spun at 100 RPM continuously. The distance between the nozzle and the substrate was fixed at 110 mm. One of the inlets of the nozzle was sealed using a threaded nylon plug. A stainless steel gage 17 needle with a luer lock was sealed to a threaded nylon luer. This assembly was screwed onto the other inlet of the atomizer. The male-luer of a glass syringe (20 mL/50 mL) containing the solution was then connected to the female luer of the needle.

The pumping mechanism for the deposition was using a KD Scientific syringe pump equipped with a glass syringe capable of precise flow rates of 0.1 nL/min. Continuous low pressure air-draft was supplied to the deposition chamber via glass( later replaced with brass) tubes snug fit onto holes drilled into the rubber stop. The holes were drilled concentrically around the nozzle at eight symmetric points (Figure 10f). The draft tubes were into the chamber at a distance of  $16 \pm 0.1$ mm from the bottom plane of the rubber stop. The dotted connection lines in Figure 9 are indicative of the symmetric points on the diametrically opposite side.

Prior to characterizing the sprays, a power amplitude sweep (16-46% of the adjustable amplitude controls) was performed at each solution weight percent (0.2, 2, 4%) to determine the critical amplitude at which a gentle spray formed at 50 $\mu$ L/min. In order to make sure that this was not solution flow rate dependent, the flow rate was also varied between 50 $\mu$ L/min to 2000 $\mu$ L/min. The flow rates used were 50 $\mu$ L/min, 100 $\mu$ L/min, 200 $\mu$ L/min, 500  $\mu$ L/min, 1000  $\mu$ L/min and 2000  $\mu$ L/min. Since the deposition of the atomized droplets was taking place with the aid of an air-draft, the spray patterns could

change as a function of air-draft pressure. For testing the dependence of the spray on the air draft pressure, only the 0.2 and 4% solutions were tested. The system was thus operated at the aforementioned flow rates and at different air-draft pressures of 0 psi, 0.25 psi, 0.5 psi and 1 psi.

The spray itself was illuminated at the tip using a medium-high power lamp and the events visually observed and noted down. Qualitative features of interest were the nature of the spray core, the spray widths, the spray-wall interactions and any dependence of the energy supplied on the flow rate.

The quantitative characterization of the spray was performed by collecting droplets at all solution weight percents at an air-draft pressure of  $0.9 \pm 0.1$  psi. The droplets were collected in a 50 mm x 50 mm square glass substrate acquired from McMaster-Carr. Flow rates investigated were 25  $\mu\text{L}/\text{min}$ , 50 $\mu\text{L}/\text{min}$  and 150 $\mu\text{L}/\text{min}$ . Only 500-600 $\mu\text{L}$  of solution was supplied in each case. Depending on the flow rate the duration of the experiment varied between nearly 20 minutes for the 25 $\mu\text{L}/\text{min}$  sample to about three minutes for the 150 $\mu\text{L}/\text{min}$  sample.

#### **4.3.2.2 Film Fabrication Protocols**

The deposition process was carried out in several ‘passes’. Each pass was fixed to 1450 $\mu\text{L}$  supply volume followed by a post deposition ‘dry time’ of five minutes. Films were fabricated at each solution weigh percent (0.2, 2, 4) as a function of:(1) sonic energy supplied (minimum energy for that weight % solution to 46%), (2) temperature (45°C/85°C), (3) flow rates (50 $\mu\text{L}/\text{min}$  (except for 0.2%) ;150 $\mu\text{L}/\text{min}$ ). For (1), the flow rate was maintained at 150 $\mu\text{L}/\text{min}$  and temperature at 45°C and minimum spray energy

was used. For (2), the flow rate was maintained at 150 $\mu$ L/min and minimum spray energy used. For (3) the temperature was maintained at 45°C and minimum spray energy used.

Finally, the films were peeled off in two discrete steps. In the first step, the substrate was carefully removed from the chamber and thin scotch tape was applied to its edge for providing integrity and support to the film. The physical peel off itself was performed utilizing soft flat tipped tweezers. All thickness measurements were made using a micrometer. Once the films were peeled off, they were promptly placed in a zip lock bag.

#### **4.4 Solvent Drying Measurements**

Solvent drying was measured as a function of time for only the THF ( b.p=60°C) based cast film samples. These measurements were carried out on a 0.0001 g analytical balance that was configured to acquire data at 2 Hz. The set-up basically consisted of a covered glass mold with the solution placed on the balance at room temperature of 20°C. Such measurements could not be performed for the DMAC based cast films as the boiling point of DMAC was higher at 170°C and room temperature drying was time consuming for sample preparation.

For all the other films including the above THF cast films, measurements were carried out to monitor the residual solvent evaporation from the films. In order to make sure that there was no residual solvent present; all specimens were subject to vacuum treatment at 35  $\pm$  5 °C. Mass measurements were obtained at intervals of one to two days until the mass curve flattened out.

#### **4.5 Tensile Mechanical Testing**

All thin film samples were tested on an Instron test system equipped with a 100 N load cell according to the ASTM D882 at 5mm/min and 50 mm/min. The strain measurements were obtained by monitoring the cross-head displacement of the test machine. Sample dimensions were fixed in such a way that the sample widths varied between 2.3-2.7 mm to maintain a width to thickness ratio of greater than 8. All tests were performed at  $20 \pm 2^\circ\text{C}$ . The coupons were prepared by placing the films on a printed grid sheet spaced 2.5 mm wide. Initially the roughly 45x 45 mm film sample was cut into two halves before being placed on the printed grid sheets for coupon preparation. Carbon steel razor blades were utilized and care was taken to prevent any edge associated defects. The sample preparation procedure and test set-up has been shown in Figures 11 and 12. In order to achieve failure in the gauge section and also to reduce the errors associated with sample handling, a sample placement protocol was formulated.

In Figure 11 we see a slotted mica sheet with adhesive magnetic strips glued to either end of the slot for sample gripping. The slot itself is about 10 mm wide allowing a sample gage length of 8-9 mm. The full length of the sample was about 15-16 mm allowing sufficient amount of sample was gripping on both sides. Samples were placed between adhesive coated magnetic tabs (approx. 5mm x 5 mm) very carefully so that no pleats are formed on the film during mounting. The slotted mica rig with sample was then mounted on the screw actuated grips (Figure 12). The mica rig not only eases the sample mounting of thin and flexible film, but also it helps to align the sample by adjusting the screw on both sides of the grip during testing. Constant screw thread revolutions on each end of the grips were maintained for uniform gripping pressure. Prior to testing, the

slotted mica rig was cut using a sharp scissor on the edges. Care was taken to not pre-stress or strain the films during the sample mounting stage.

#### **4.6 Optical Microstructure Characterization**

A Meiji optical microscope was used in the transmission mode to obtain micrographs of the deposited samples as a function of solution wt%, flow rate, temperature and sonic energies used. The influence of the use of the air-draft and the effect of varying the liquid to air ratio on sample microstructure have been reported using these measurements. The microscope was outfitted with a DCM 310 10X digital camera and the resolution of the microscope was calibrated at all magnifications using 25LPI (lines per inch) and 300LPI Ronchi gratings. All microstructure analysis was performed using the open source imageJ [63] software. Macros were written to resolve the images as per the calibration images and also to threshold and create binary images. The images were then automatically analyzed for circular shapes with circularities between 0-0.4, 0.4-0.8 and 0.8-1. Circularity defined as  $4\pi*(Area)/(Perimeter)^2$  measured the roundness of the feature .

#### **4.7 Differential Scanning Calorimetry (DSC)**

Glass and melt transitions of all the samples have been measured via differential scanning calorimetry (DSC) using a TA Instruments Q1000 DSC. The difference in the heat energy required to maintain a reference empty pan and a sample pan at the same temperature were measured as a function of temperature between -85°C-200°C at 10°C/min.



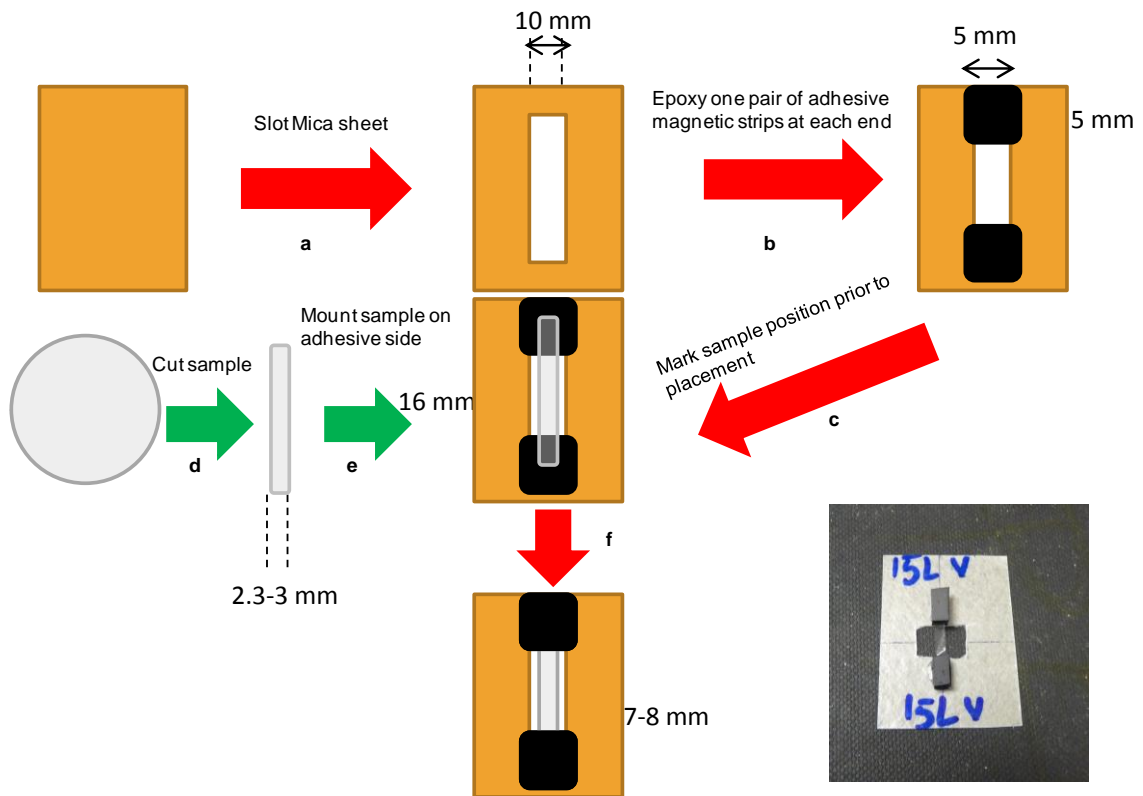


**Figure 11** Step by step thin film test coupon preparation procedures.

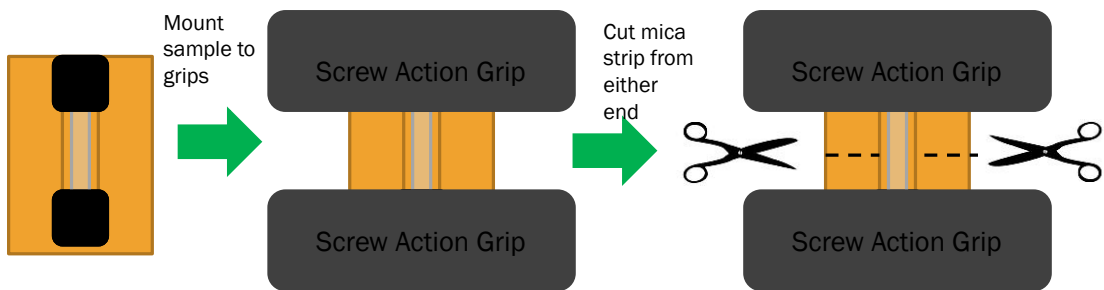


**Figure 12** Tensile thin film test protocols.

Any energy absorption by the sample would reduce the energy going to the sample pan relative to the reference pan and drive the electronics to maintain the same temperature. On the other hand, an exotherm would increase sample pan temperature and cause the electronics to reduce energy to the sample pan relative to the reference pan.

Samples were prepared by cutting pieces of the film using a razor blade. The pieces of the film were carefully placed in aluminum pans and the lid placed on the pans followed by crimping. The sample masses were measured using a high precision microbalance and were always at least 2.0 mg. Care was taken to always handle these films with gloves.

#### **4.8 Small Angle/ Wide Angle X-Ray Scattering (SAXS/WAXS)**

Control-TPU and atomized-TPU samples were all measured using SAXS/WAXS to characterize the amount of phase mixing, extent of phase separation and relative amounts of hard and soft segments. The instrument utilized for the measurements was a Rigaku pinhole collimation SAXS system with scattering vector range between 0.07-1.59 nm<sup>-1</sup>. All the samples were initially mounted on rectangular plate sample holders with round holes in the center. The sample itself was held on the sample holder using scotch tape (the scotch tape was placed so as not to contact the x-ray beam) so that the sample went across the opening. The transmittance for each sample was manually recorded and sample positions calibrated. Scattering data depends on the spatial dependence of varying electron densities within the specimen. The scattered radiation was then detected by a two-dimensional wire detector at a distance of about 1.5 meters from the sample. Data was gathered for a period of 12 hours for each sample. The scattering intensity (I) plot as a function of scattering vector (q) was generated for all the samples. Data was

corrected for detector sensitivity, absorption and converted to scattering vector using silver behenate standards. Absolute intensities were determined using a calibrated highly annealed polyethylene sample.

WAXS measurements used the same set-up but data was gathered on a Kodak film placed at a distance of about 5 mm from the sample; the largest scattering angle collected was  $\sim 40^\circ$ . These measurements were carried out to check for any crystalline ordering within the macromolecules of the TPU. Sample data collection times were roughly 6-8 hours per film.

#### **4.9 Atomic Force Microscopy (AFM)**

A Pacific Nano Technology Atomic Force Microscope (AFM) NanoR2 was utilized to perform tapping mode images of all samples. The instrument was operated on the EZMODE. The instrument was checked for connections and the piezo checked for linearity. Typically, sample preparation involved placing a small square (about 5mm x5mm) on a double sided tape mounted on a glass cover slip. The glass cover slip was then placed on a magnetic tape to be loaded onto the magnetic sample holder.

Pre-mounted Agilent U 3120A AFM tips were used. The tips had a nominal force constant of 40 N/m, a resonant frequency of 300 kHz and a tip diameter of 10 nm. After the tips were mounted on to the tip holder, the laser dot was carefully moved on to the edge of the cantilever (as close as possible). The laser dot was then aligned in such a way that the laser detector measured a signal way above the threshold requirements for a good image. The tip was tuned to check to see if the resonant frequency matched with its

specifications of 300 kHz. The tuning conditions were typically at a set phase difference of  $-20^\circ$  and free oscillation amplitude of  $-1500$  mV.

Using an optical microscope providing live feedback onto a TV monitor, care was taken to set the exact positions of the sample and the tip on the machine's control interface followed by a coarse contact. Following these steps, the tip was brought 'in contact' with the sample surface. Obviously for non-contact imaging the tip was very close to the sample but not touching it.

Imaging was done under moderately hard to hard tapping conditions. This was done by adjusting the ratio of set point to free oscillating amplitude. Lower the ratio, harder the tapping force on the sample. In conjunction with these parameters, the proportional/gain settings were also carefully controlled to obtain forward and backward tip movement signals that matched. Two  $1\mu\text{m} \times 1\mu\text{m}$  images were scanned for each sample and all data analysis/smoothing performed using an open source software called Gwyddion [64] and imageJ.

#### **4. 10 Rationale and Scope of Work: Design of Experiments**

With the sole purpose of answering the research questions mentioned under 2.8 and 3.4, a broad list of independent and response variables were built with the aim of fabricating  $20\mu\text{m}$  films.  $20\mu\text{m}$  was the chosen thickness as this was the least thickness at which handling of the film was manageable. All of the variables have been listed in Table-3. The table depicts the refinement procedure that was undertaken to effectively test only the most important independent variables that were affecting the problem at hand.

While all of the independent variables were fully ‘independent’ of the response variables, there were three variables with potential of a possible dependency on the weight percentage of polymer in the solvent. The flow rate, energy delivered to nozzle and air-draft pressure has been listed as optimization variables instead. These variables have been shown in Table-4.

In-order to understand the significance of the optimization variables, trial experiments were performed as a function of flow rate, air-draft pressure and energy delivered to nozzle. At low flow rates like 20 $\mu$ L/min, it takes nearly 30 minutes for the flow to even develop. Above 150 $\mu$ L/min, the system was incapable of handling the throughput in a continual spray mode. Varying the air-draft pressure varied the spray width and beyond 2 psi, there was evidence of back-flow.

In order to maintain the influence of the air-draft pressure on the spray trajectory at least 0.9 psi was necessary. Each polymer weight percent solution had a certain minimum energy at which the spray was formed. Initially, it was planned to operate the nozzle at 25, 50, 100% energy relative to this minimum. Later this was simplified to four discrete energy levels 23%, 29%, 37% and 46%. Later in the chapter on results and discussion, we would see that 23%, 29% and 37% were the minimum energy required for the atomization of the 0.2%, 2% and 4% solutions.

We see that performing a full scale investigation incorporating all variables would result in approx. 6000 individual experiments with-out repeats. A simple refinement has also been shown in the same table. The numbers of levels of the variables that have been struck through have been fixed to one. We see that the number of experiments trickle

down to 18. Tables-5 and 6 show the final sets of independent and response variables after considering the influence of t.

In part, the rationale for doing so has been to introduce multiple levels only in variables expected to produce different responses. Another important reason was to simplify the problem so that not too many factors influence the responses which would make interpretation difficult. For instance, changing the nozzle type or the substrate type was not going to help answer critical process- microstructure related questions that have been posed in the previous chapters.

**Table 3: Independent Variables Affecting the Thin Film Deposition**

Independent Variables	# of levels		Qualitative	Quantitative	Detail
	Full	Reduced			
Nozzle profile	2	2			Flat/ <b>conical</b>
Frequency	2	1			<b>20 kHz</b> , 40 kHz
Solvent <sup>i</sup>	3	1			<b>DMAC</b> , THF, MC, DMSO, DMF
Substrate Type	2	1			Silicon, <b>Glass</b>
Tip-Substrate Distance	3	1			approx <b>110 mm</b> , 75 mm, 50 mm
Substrate Temperature	3	3			<b>25°C</b> , <b>45°C</b> , <b>85°C</b>
Draft Type	2	1			<b>8 concentric holes</b> or new ones with 16 holes
Draft Position	3	1			along tip, below tip, <b>Above tip</b>
Wt% Polymer <sup>ii</sup>	3	3			0.2, 2, 4
% Energy delivered wrt minimum <sup>iii</sup>	4	1			0, 25, 50, 100
Flow Rate	1	1			150 $\mu$ L/min
Draft Pressure	1	1			0.9 +/- 0.1 psi
Substrate Spin Speed	1	1			100 RPM
	5724	18			

**Table 4: Variables Dependent on the Polymer Weight Percent**

Optimization Variables	Qualitative	Quantitative
Flow rate range		
Atomization amplitude (Energy Delivered)		
Draft pressure range		

i-**DMAC**=Di-Methyl Acetamide , **THF**=Tetra Hydro Furan, **DMSO**= DiMethylsulfoxide, **DMF**= DiMethylFormamide

ii-wt% stands for weight percentage of polymer dissolved in the solvent

iii-wrt stands for with respect to and minimum energy was the least energy required for a spray to form



**Table 5:** Final Set of Independent Variables for Investigation

Independent Variables	# of levels		Qualitative	Quantitative	Detail
	Full	Reduced			
Nozzle profile	2	2			Flat/ <b>conical</b>
Frequency	2	1			<b>20 kHz</b> , 40 kHz
Solvent <sup>i</sup>	3	1			<b>DMAC</b> , THF, MC, DMSO, DMF
Substrate Type	2	1			Silicon, <b>Glass</b>
Tip-Substrate Distance	3	1			approx <b>110 mm</b> , 75 mm, 50 mm
Substrate Temperature	3	2			<b>25°C</b> , 45°C, <b>85°C</b>
Draft Type	2	1			<b>8 concentric holes</b> or new ones with 16 holes
Draft Position	3	1			along tip, below tip, <b>Above tip</b>
Wt% Polymer <sup>ii</sup>	3	3			0.2 ,2,4
% Energy delivered <sup>iv</sup>	4	2(4), 3 (2) , 4 (0.2)			23, 29, 37, 46
Flow Rate	2	2			50 $\mu$ L/min, 150 $\mu$ L/min
Draft Pressure	1	1			0.9 +/- 0.1 psi
Substrate Spin Speed	1	1			100 RPM
	5724	8,24,16 = 48			

**Table 6:** Output Response Variables

Output Response Variables	Qualitative	Quantitative
Thickness		
Degree of smoothness/Roughness		
Droplet diameter distributions (Optical Microscopy)		
Tensile Mechanical (ASTM-D882-09)		
Thermal Calorimetric characterization		
Atomic Force Microscopy (AFM)		
Small Angle/Wide Angle X-Ray Scattering (SAXS/WAXS)		

iv- Number in bracket denotes weight percentage of polymer, the number outside the bracket denotes the number of energy levels

## Chapter 5.

### THIN FILM PROCESS CHARACTERIZATION

#### 5.1 Film Deposition Optimization

##### 5.1.1 Initial Results: THF Based Films

The premise for the bulk of this work lies in the results that were published by Balakrishnan and Saha [65] for THF based TPU films. Using a manually operated syringe, a 20 kHz atomizer was used to atomize and fabricate thin TPU films between 20-25 $\mu$ m. The optical microstructures obtained have been shown below in Figure 13. It was observed that the microstructure had dried out droplets of polymer forming a solid phase together with polymer particulates forming a grainy surface. These results formed the basis for the application of the layer-by-layer processing method in this dissertation. However, there were critical issues in the work that needed to be addressed before a detailed investigation of the process could be carried out. These issues were a) Repeatability of the process (due to manual pumping), b) defined thickness-solution required relationships, c) Uniformity of thickness from point to point on the substrate, d) Control of surface morphology and roughness.

##### 5.1.2 Transition to DMAC as Solvent

One of the issues with THF was that its boiling point was low at 60°C. At such temperatures, during atomization at 23% of supplied power (1-3 W) it was observed that

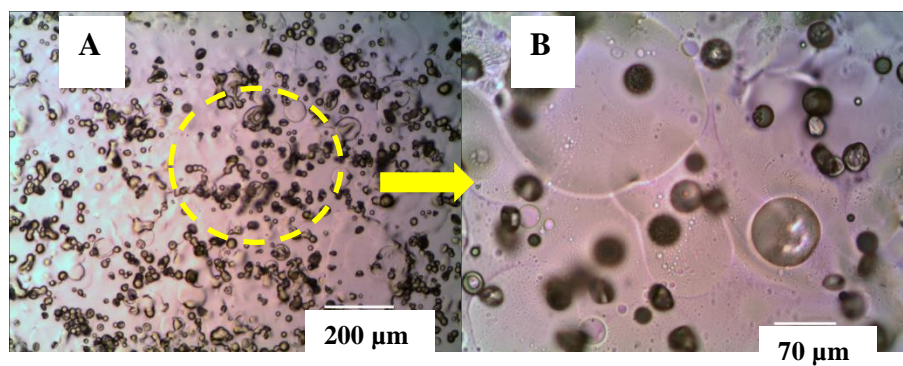


**Figure 13** TPU film with dried out droplets evident. These droplets are in the form of polymer particulates yielding a grainy film surface.

the solvent tended to evaporate quickly resulting in a spray that was a combination of solution droplets and dried out polymer particulates [65]. In other words, the solvent changed phase into vapor during the course of atomization. This meant that a higher boiling solvent needed to be used to maintain the liquid state of the solution during atomization. For this reason, a higher boiling DMAC with a b.p of 170°C was chosen as the solvent. This allowed the expansion of the DoE to cover film manufacturing at higher temperatures ( $\ll 170^{\circ}\text{C}$ ) and higher atomizer energies.

### **5.1.3 Regulated Flow with DMAC as a Solvent**

Based on the results achieved with THF via a manually operated syringe, it was immediately realized that the precision of the flow affected the film surface morphology, and the uniformity of the film thickness. For this reason, a computer controlled syringe pump was used for regulating the flow. Obviously even with flow regulation, uniform film formation seemed to depend on the minimization of the randomness of the spray and allowance of adequate time for solvent evaporation. The randomness of the spray happened due to the low to medium flow rates that were used (50-200 $\mu\text{L}/\text{min}$ ). These flow rates were the best choice as any higher flow rate used would immediately flood the 50mm x50mm substrate landing too many drops that would prevent film drying and film formation. Even with a low to medium flow rate, times needed to be set aside for solvent evaporation during the deposition process. Basically, the spray had to have a definite path from time to time and also had to have the capability to operate semi-continuously without flooding the substrate.

### **5.1.4 Air-Draft Attachment Implementation and Role in Film Formation**

As shown in Figure 10 e and f, an air-draft attachment was devised to solve the issue related to the randomness of the spray and film drying. The attachment itself was in the form of a volume bottle with eight outlets. The eight outlets were then connected to brass tubes that were inserted concentric to the nozzle [66].

For the same solvent, the ejection of droplets was dependent on key factors like the viscosity of the solution, age of the solution, the amount of energy supplied and the state of the nozzle (fully clean vs slightly clogged with several microns of material). For different solvents with different boiling points, the ejection of the droplets also depends on the flow rate used. The mechanism of the spray shown in Figure 14 depicts only the final stage of a sequence of events that lead to the deposition. Initially, the spray droplets periodically move in the direction of the eight outlets of the air draft. Then, the low pressure air carries the droplets initiating their controlled coalescence. Finally, the droplets dried on the substrate with the aid of the air draft. . The initial event is just the ejection of a multitude of droplets that then coalesce almost immediately. The droplets produced evolve from the nozzle in the form of a smooth mist forming a spray core. The mist was ‘shaped’ and ‘directed’ by the air emerging from the draft tubes [66].

We hypothesize that the air draft tends to size separate the droplets and also accelerate them towards the heated substrate. During this step, the droplets do tend to lose solvent and also try to minimize their surface area at the same instant. But once the spray droplets hit the substrate, they start spreading and begin forming the final film morphology.

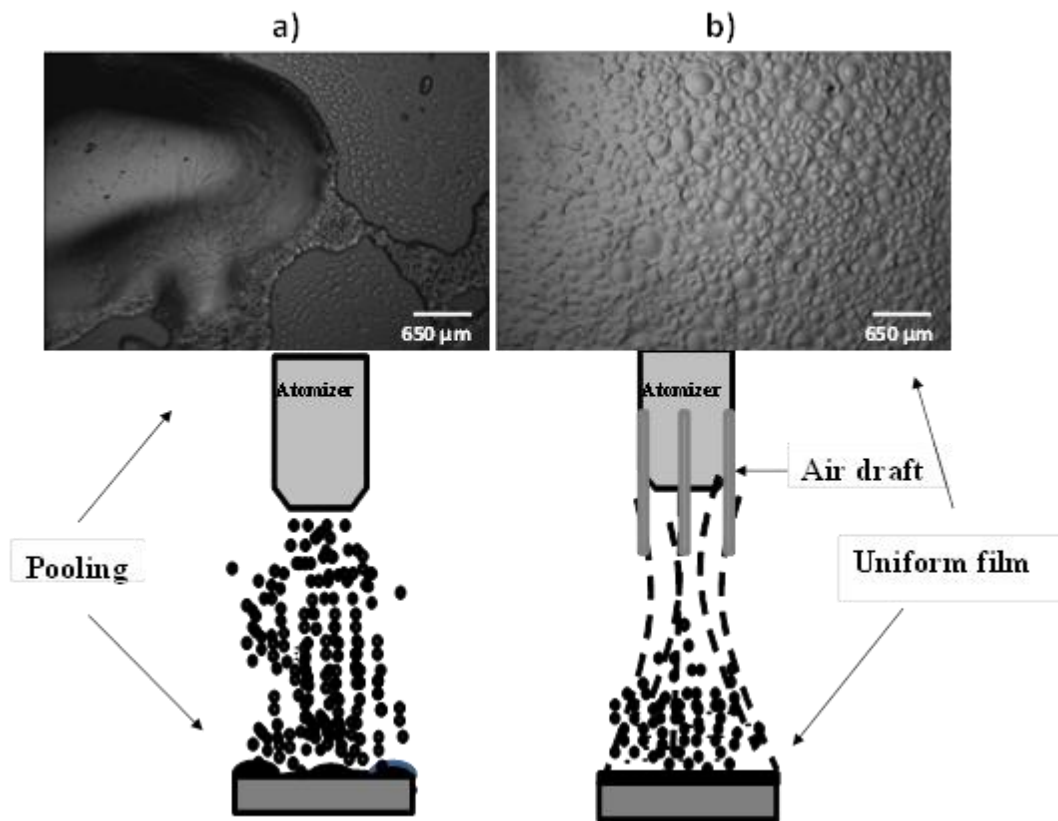


**Figure 14** Mechanisms of film formation and microstructures achieved a) without and b) with air-draft for DMAC based films.

We are not aware of the spray widths and the extent of this size separation. But we do know that the air-draft controls the spray path and shape very precisely [66].

### **5.1.5 Effect of Air Draft on Material Wastage and Energy Consumption**

In order to illustrate the effect of the draft, we have listed our samples in Table 7. Without an air-draft, the spray developed for samples I and II were imprecise for producing uniform films. With pulsing for sample I, an imprecise film ( $>10\mu\text{m}$ ) could still be obtained after a long process time. Pulsing here refers to turning the nozzle on/off every one minute. At  $100\ \mu\text{L}/\text{min}$ , we pulsed the pump 29 times at 60 second intervals to a total volume of  $2900\ \mu\text{L}$ . This specified the total spray/fabrication time to 29 minutes. Once the spray developed and the deposition began, we noticed that after each pulsed spray phase, the deposited spray was not drying for up to 10 minutes. For the 29 pulse phases, this amounted to 290 minutes. But for sample II, there was pooling and an unusable deposit of material was obtained making continuous deposition infeasible without a long drying time (Figure 13a). As expected, with an air-draft continual deposition was possible for sample III. Thickness variations  $> 5\mu\text{m}$  for this sample demanded substrate revolution periodically (30 minute intervals) to produce sample IV with uniform microstructure and thickness  $<0.5\mu\text{m}$  variation (Figure 13b). Finally, relative to a spin coated control sample V, we see that material usage was reduced in this process. This wastage claim has been made for a corresponding film that manufactured using a spin coater.

Our observation was that with a 2% solution like ours, the amount of material needed for fully coating the substrate was 1.9 g. But our process takes 2.9 g instead. There was a

observed wastage of 1g. This was because over time, the nozzle also coated the chamber itself. Now when we poured about 1.9g of solution inside of a casting vessel, the thin film had to be compulsorily formed inside of a vacuum oven at 45°C for about 30-36 hours. The final resulting film showed meniscus effects (edge to center thickness variations) which resulted in thickness variations of up to 8 $\mu$ m for a 20  $\mu$ m film. The net amount of usable film was reduced due to such thickness inconsistencies.

With a spin coater, at sufficiently low RPMs of 450 RPM, our observation was that 2.9 g of solution poured onto the substrate (45°C) resulted in a 4 $\mu$ m film after about 60 mins. This implied that about 14.5 g was needed for a 20 $\mu$ m film in 600 minutes. For a constant weight percent solution, reducing the spin coater speed would minimize the wastage, but increase the amount of time needed for evaporation. Increase in the spin speed increases the wastage and reduces the evaporation time. 450 RPM was chosen as the working speed as it was at a sufficiently lower end of the spin coater (maximum being 6000 RPM) and would intuitively minimize wastage. A 2% by weight solution is in the dilute regime of concentration and typically an increase in the concentration does minimize wastage in spin coating. But for our samples, the data presented simply does state the observed fact that for a 2% solution, the spin coater does use more material to coat. It is noted however that this stated value of 14.5 g may change depending on the machine/dispensing system.

From the table we see that time of deposition and energy involved in the process were reduced. The atomizer energy was only 2% of the total energy provided (~1-3 W) at 29% of power amplitude. A lot of the existing processes for thin polymer film development rely on high energy sources such as RF sputtering, Plasma Enhanced Chemical Vapor



**Table 7** Energy And Material Usage for Samples Processed under Different Conditions

Sample #/Spray Mode	Air-Draft/Revolution	Total Energy (kJ)		Total Time (minute)		Solution Usage (mL)
		Sonic	Heater*	Fabrication	Dry	
I/Pulsed on & off	No/No	7	62	58	290	2.9
II/Continuous	No/No	7	5.4	58	10	2.9
III/Continuous	Yes/No	7	5.4	58	10	2.9
IV/Continuous	Yes/Yes	7	5.4	58	10	2.9
V/Control Spin Coat	Yes/Yes	-	5.4	60		14.5

\* Heater power of 1-2 W to maintain substrate at 45°C

Deposition (PECVD), magnetron sputtering, melt extrusion. As an example, a plasma enhanced CVD process utilizes an RF or radio frequency generator. The energy associated with such a process is typically 400-500 W for the plasma to be created [65]. In contrast, ultrasonic deposition is a piezoelectrically driven process and consumes lower energy for the creation of the film. The energy consumption is crucial when the process is to be considered for scale-up. These high energy sources are not always amenable for large scale industrial manufacturing especially for niche applications like polymer solar cells, organic electronics etc.

## **5.2 Spray Droplet Data**

### **5.2.1 Spray Patterns as f (flow rate, draft pressure)**

From the power amplitude sweep of the nozzle, the minimum power amplitude required to atomize all three weight percents ( 0.2, 2, 4) of the polymer solution were determined. They were 23% of the total power (approx. 2 W delivered at the tip) for 0.2 %; 29% of the total power (approx. 4 W delivered at the tip) for 2% and 37% of the total power (approx. 6W delivered at the tip) for the 4% solution. These power amplitude values had a delicate relationship with the flow rate of the fluid. For purposes of analysis, we term 50, 100 $\mu$ L/min as low flow rates, 200, 500 $\mu$ L/min as medium flow rates and 1000, 2000 $\mu$ L/min as high flow rate. For low and medium flow rates, the measured minimum power amplitudes were sufficient for full atomization. For higher flow rates, the power amplitude had to be nominally raised by 2-3 percent for successful spray formation. The spray patterns that were generated as a function of flow rate and air-draft pressure has been depicted schematically in Figure 15. The spray patterns could be split into two

broad categories: that corresponding to the low/medium and that corresponding to the high flow rates.

With minimized air disturbances, at zero air-draft pressure the spray initiated at the tip and more or less followed a vertically straight path. At low flow rates, there was no visible detection of a solid spray core (as in the presence of multiple falling droplets) and hence the spray path could easily be disturbed. The spray initiation for the same flow rate took more time for the 4% solution (about 1-2 minutes longer) compared to the 0.2% solution. For both 0.2 and 4% solutions, at medium and high flow rates, the spray tended to have a perceptible core and seemed less amenable to being disturbed.

As the draft pressure was increased from 0.25 psi to 1 psi, the spray width increased. In addition to the spray width increasing, there were several sub-“spray-cores” visible. This implied that the spray itself was being dragged continually in the direction of the eight air-draft tubes. Also this oscillation of the spray was similar for both weight percents tested and generally had a tendency to increase as the air-draft pressure was increased. As the flow rate was increased beyond 500 $\mu$ L/min, the spray violently hit the walls. Beyond 1 psi upto 3 psi, there was spray backflow observed in the nozzle tip.

### **5.2.2 Effect of Varying the Liquid to Air-Ratio**

The velocity of the air at the outlet was 73 m/s and the liquid to air ratio for our film fabrication was  $3.5 \times 10^{-6}$ . Each specific air pressure operating point maps to a specific air velocity. For an ideal gas, the air pressure velocity relationship can be derived by considering Bernoulli's equation and solving for the pressure [66].

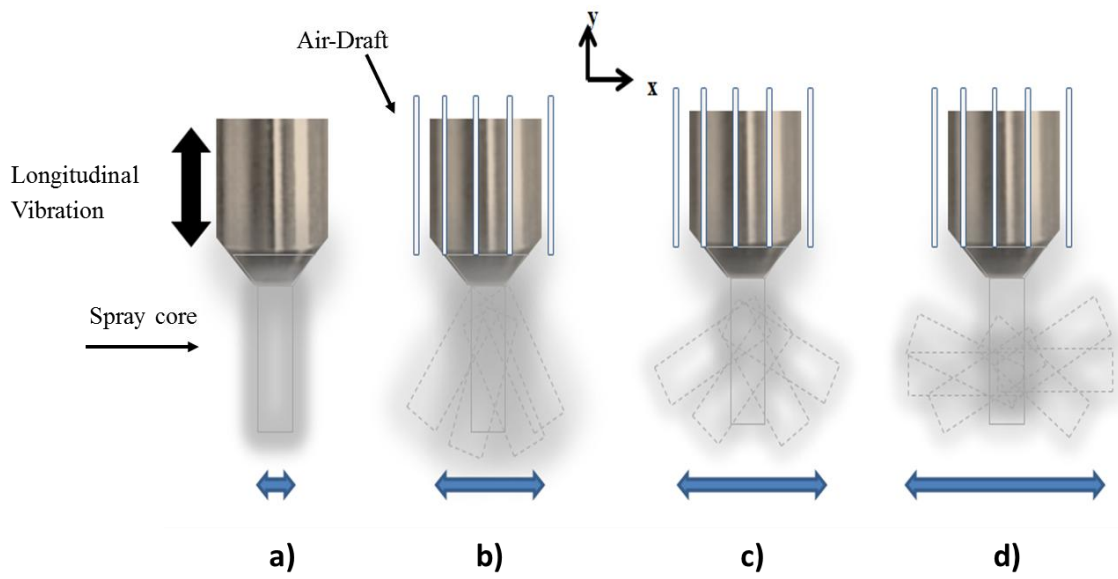


**Figure 15** Spray Patterns as a function of draft pressure. We see that as the air-draft pressure is increased from zero to 1 psi, the spray width changed.

$$p = \frac{1}{2} \rho v^2 \quad (24)$$

For 0.9 psi of air or 6204.6 Pa of air and knowing air density at 45°C (from  $p = \rho RT$ , where  $R = 8.314 \text{ Nm/mol.K}$ ) ; the velocity was 73 m/s. For computing the liquid to air ratio, we have first calculated the air-flow rate which is the air velocity times the area of the draft tube ( $3.28 \times 10^{-6} \text{ m}^2$ ). The flow rate is  $2.4 \times 10^{-4} \text{ m}^3 \text{ s}^{-1}$ . The flow rate of the solution was  $50 \mu\text{L/min}$  or  $8.3 \times 10^{-10} \text{ m}^3 \text{ s}^{-1}$  and  $150 \mu\text{L/min}$  or  $24.9 \text{ m}^3 \text{ s}^{-1}$ . At any particular time instant of 1 second, the liquid to air ratio was  $3.5 \times 10^{-6}$  ( $50 \mu\text{L/min}$ ) and  $1.16 \times 10^{-6}$  ( $150 \mu\text{L/min}$ ) which would imply a situation where a column of air carries microscopic volumes of droplets down to the substrate [66].

In order to determine the effect of varying the liquid to air ratio on droplet coalescence and aggregation, spray experiments were performed at flow rates  $25 \mu\text{L/min}$ ,  $50 \mu\text{L/min}$  and  $150 \mu\text{L/min}$ . For avoiding coalescence over several orders of magnitude, the total volume sprayed in such cases was restricted to  $500 \mu\text{L}$ . The liquid to air ratio at any time instant is directly dependent on weight percent of the polymer in a given solvent (keeping the air pressure fixed). For a fixed weight percent polymer solution, the air to liquid ratio depends on i) the flow rate used, ii) air pressure used. Changing the liquid to air ratio changes the volume of droplets delivered to the substrate. This in turn controls the droplet –droplet interactions and solvent evaporation. The results of our experiments have been shown in Figure 16. Some of the droplets have been circled to show the typical minimum, maximum droplet diameters and coalescence.

At the lower flow rate of  $25 \mu\text{L/min}$ , the droplet diameter range seems to be much larger than in the case of  $50 \mu\text{L/min}$  (between  $130\text{-}325 \mu\text{m}$ ). It is interesting to note that with the

50 $\mu$ L/min sample, most of the droplets seem to be having diameters in-between the maximum and minimum values that exist for the 25 $\mu$ L/min sample (roughly 195 $\mu$ m and barely any droplets in the 300 $\mu$ m range). With the 150 $\mu$ L/min sample, a number of droplets seem to lose shape owing to coalescence as well (diameters range between 200 $\mu$ m to values >650 $\mu$ m based on extent of coalescence) [66].

We also see that at a flow rate of 25 $\mu$ L/min, the number of droplets obtained for the same total supplied volume is far less than that for 50 $\mu$ L/min and 150 $\mu$ L/min. This could mean that at 25 $\mu$ L/min, the majority of the solution is lost to depositing the chamber (instead of the substrate). The droplets created at that flow rate are smaller in diameter when they are exposed to a tremendous amount of air pressure and are barely acted on by gravity. They probably just directly hit the walls without depositing the substrate. This obviously means that a directed spray towards the substrate (especially for coating or film applications) necessitates the presence of a larger population of droplets prior to being acted upon by an air draft. Again, one needs to keep in mind these results are but for one solvent DMAC. The trends will differ based on the boiling point, atomizer frequency and atomizer vibration amplitude.

### **5.2.3 Apparent Droplet Diameter Distributions**

The spray droplet diameters reported were the final dry diameters of the polymer deposited on the glass substrate (hence the term apparent as this diameter was not the actual spray diameter emerging out of the nozzles). Figure 17 indicates the sequential steps followed in the analysis. Figure 12 displays these values for the 25 $\mu$ L/min case.

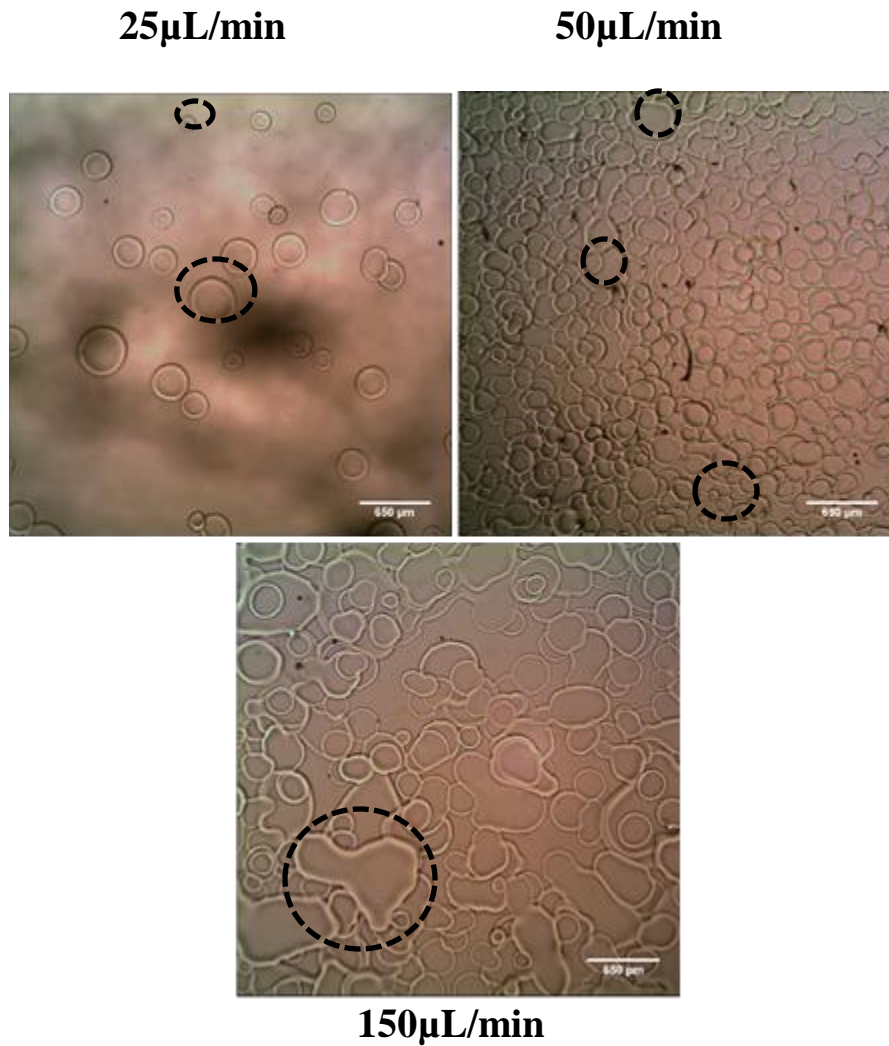


**Figure 16** Effects of varying the liquid to air ratio. As the liquid to air ratio increases, a higher degree of coalescence is evident. As a result, the number of droplets collected increased together with an increase in their sizes.

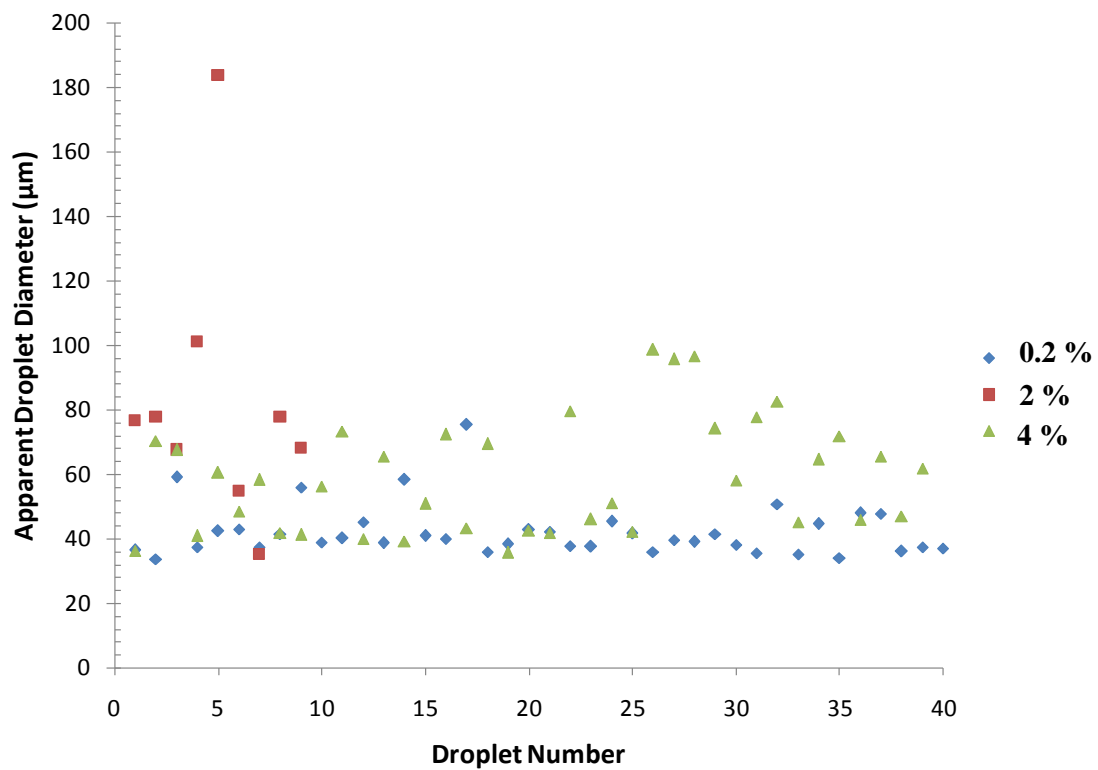


**Figure 17** Apparent droplet diameter distributions for the 25µL/min



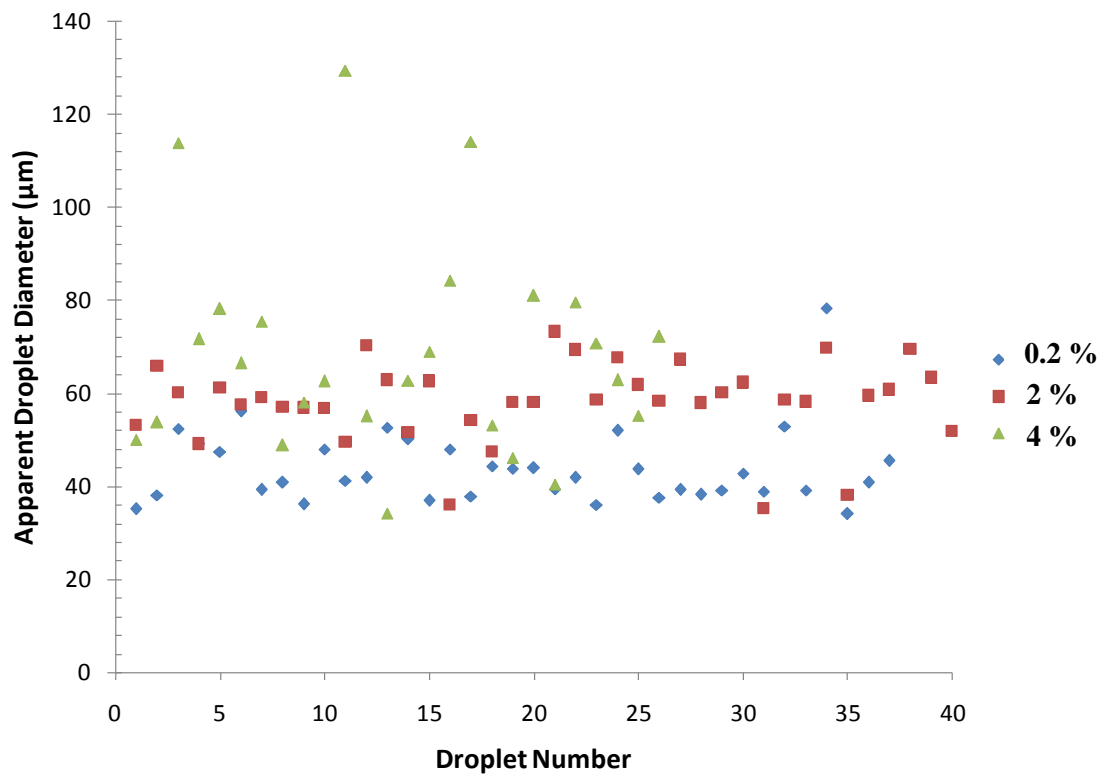


**Figure 18** Apparent droplet diameter distributions for the 50 µL/min

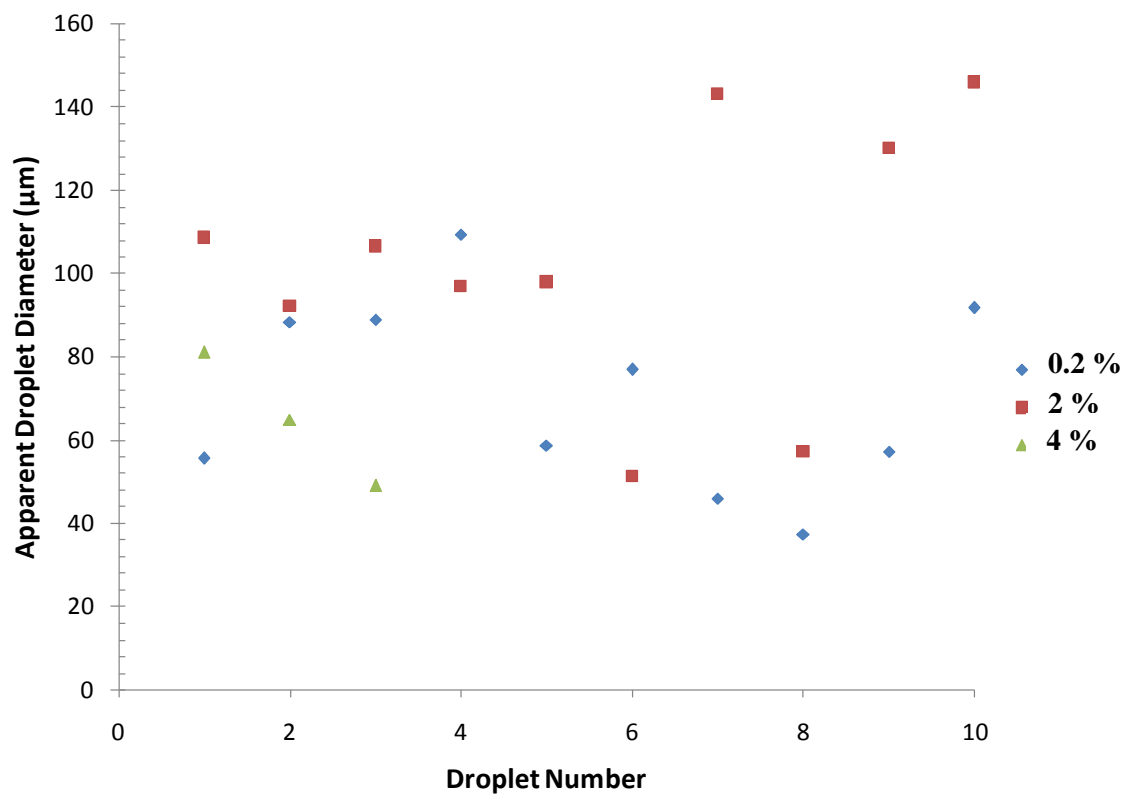


**Figure 19** Apparent droplet diameter distributions for the 150 µL/min

The droplet diameter varies roughly between 40 $\mu$ m for the 0.2% solution to about 100 $\mu$ m for the 4% solution. Interestingly however, the droplet diameters for the 2% case, show higher values than the 4% solution. Figure 18 shows a similar set of measurements for 50 $\mu$ L/min. We see that in this case, the droplet diameters increase gradually as a function of weight percentage from 40 $\mu$ m to 120 $\mu$ m. Figure 19 shows the final case of 150 $\mu$ L/min where very few droplets exist in a circular form. In fact the droplet diameters being reported for this last case were most probably results of multiple coalescence events. The droplet diameters for this flow rate were almost 3-4 times more than their corresponding values for the other two flow rates. Obviously, the number of droplets measured for each case was also affected by the extent of coalescence occurring on the substrate. Even at the same flow rate, this number seems to go down indicative of a definite weight percentage dependent coalescence. Also to be noticed here is that in all three cases, in spite of a few larger droplet diameters (coalesced drops), the overall distribution is pretty uniform at each weight percent and flow rate.

#### **5.2.4 Median Droplet Diameter: Influence of Physicochemical Properties and Solution Flow Rate**

Figures 20 through 23 indicate the influence of the physicochemical properties of the three polymer solutions (0.2, 2, 4%) on the resulting median droplet diameter. In Figure 20 droplet diameters are plotted as a function of solution density. With increasing density and at increasing flow rates, the measured median droplet diameter was always higher except at the highest density (4% solution). This result was evidence of more number of smaller droplets forming and coalescing that with the 0.2% and 2% solutions. With the 4% solution, the difference in the droplet diameters at the three flow rates were

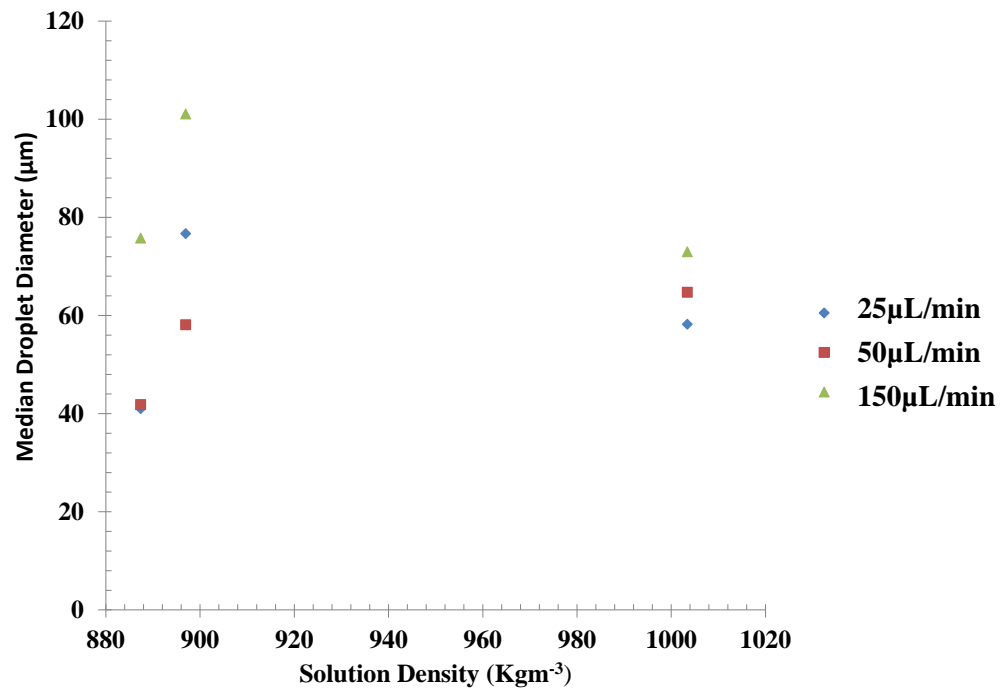


**Figure 20** Median droplet diameter data as a f(solution density)

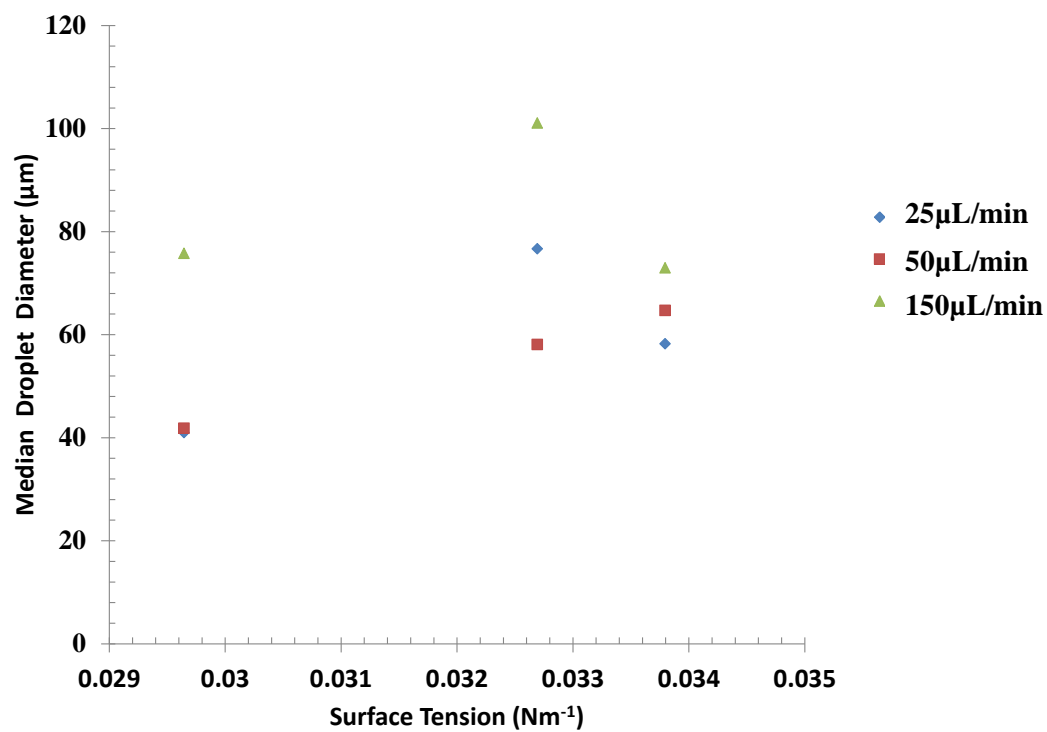


**Figure 21** Median droplet diameter data as a f(solution surface tension)

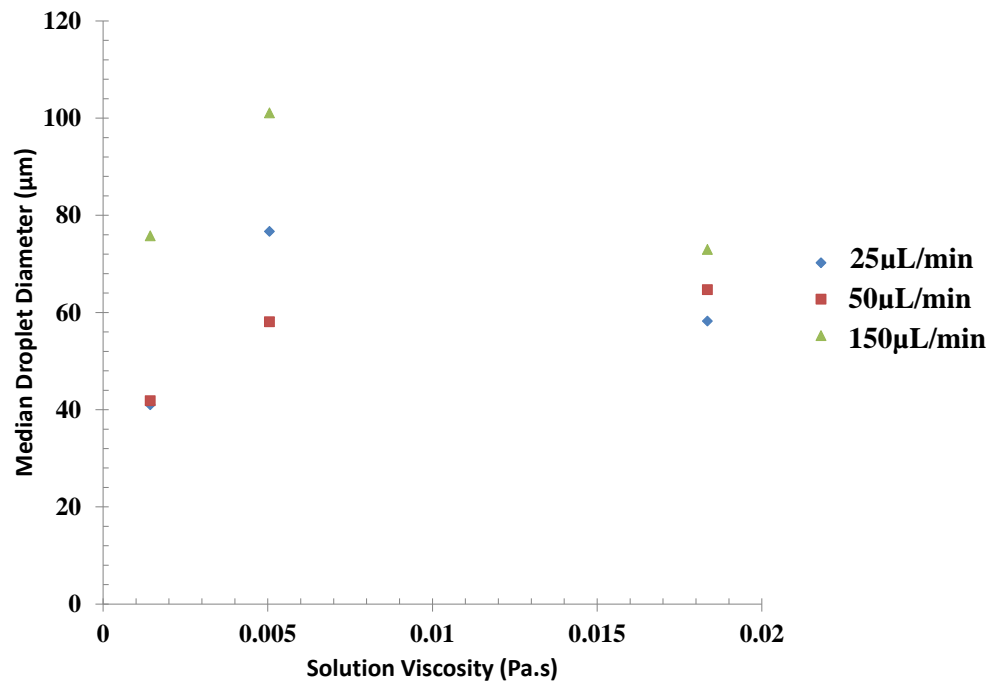


**Figure 22** Median droplet diameter data as a f(solution viscosity)

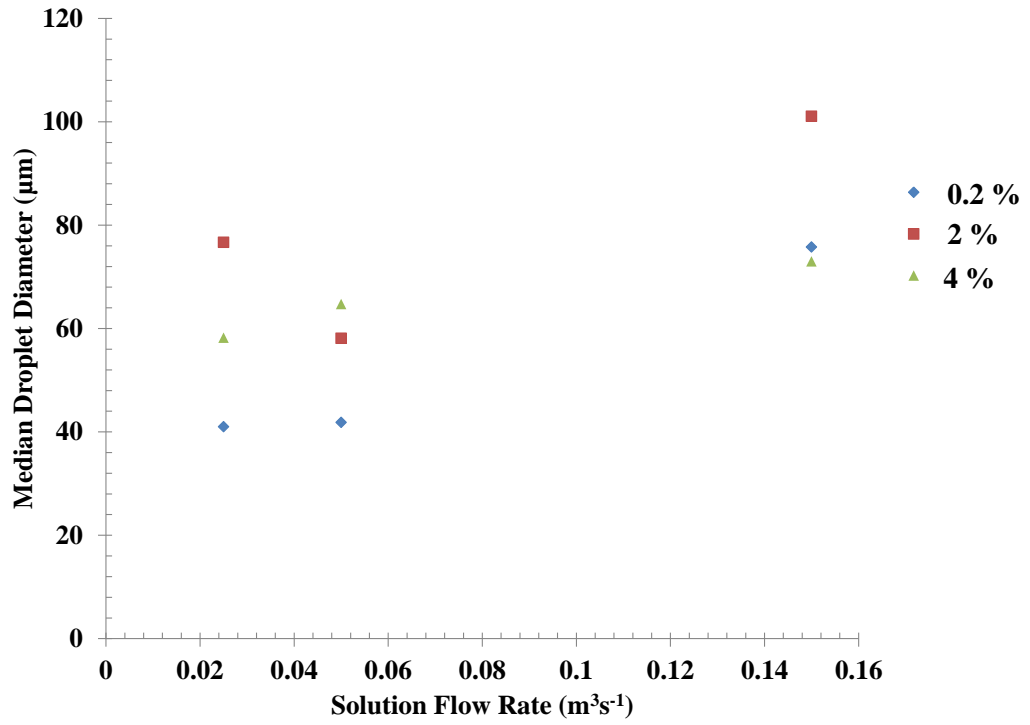


**Figure 23** Median droplet diameter data as a f (flow rate)

only about 10-15 $\mu\text{m}$ . The difference was much larger with the 0.2 and 2% samples. Data in Figure 21 was indicative of the ease with which new surfaces were formed for the 0.2 and 2% solutions. This made sense as surface tension was a direct function of the solution concentration. Also Figures 22 and 23 showed the dependence of the droplet diameter on viscosity and flow rate. We see that with increase in viscosity, the droplet diameter tends to plateau out to a constant value. While with increase in flow rate, the droplet diameter actually increases to higher values.

### **5.3 Solution Volume Determination and Thickness Trends**

In Figure 24, the solution volume required for a given dried thickness got exponentially higher as the solution weight percentages decreased. For example, at 150 $\mu\text{L}/\text{min}$  the 4% films were fabricated in over an hour, the 2% samples took over 2.5 hours and the 0.2% samples took over 28 hours to fabricate. In Figure 25, the average polymer film thickness has been plotted with standard error bars calculated from 30 samples. The standard deviations in the thicknesses were 2.8 $\mu\text{m}$  for the 4% films, 3.7 $\mu\text{m}$  for the 2% films and 2.8 $\mu\text{m}$  for the 0.2% films. Based on the droplet diameter variations, it was ostensible that larger droplet diameter events could result in slightly larger deviations from the average. At the same time, the process did show system integrity issues when running long term samples such as the 0.2% films. Leaks in the syringe luer lock assembly, variations in the draft pressure by about 0.05-0.1 psi, the changing concentration of the solution all played part in the manifestation of these deviations.

### **5.4 Film Drying and Gravimetric Analysis**

#### **5.4.1 THF Based Films**



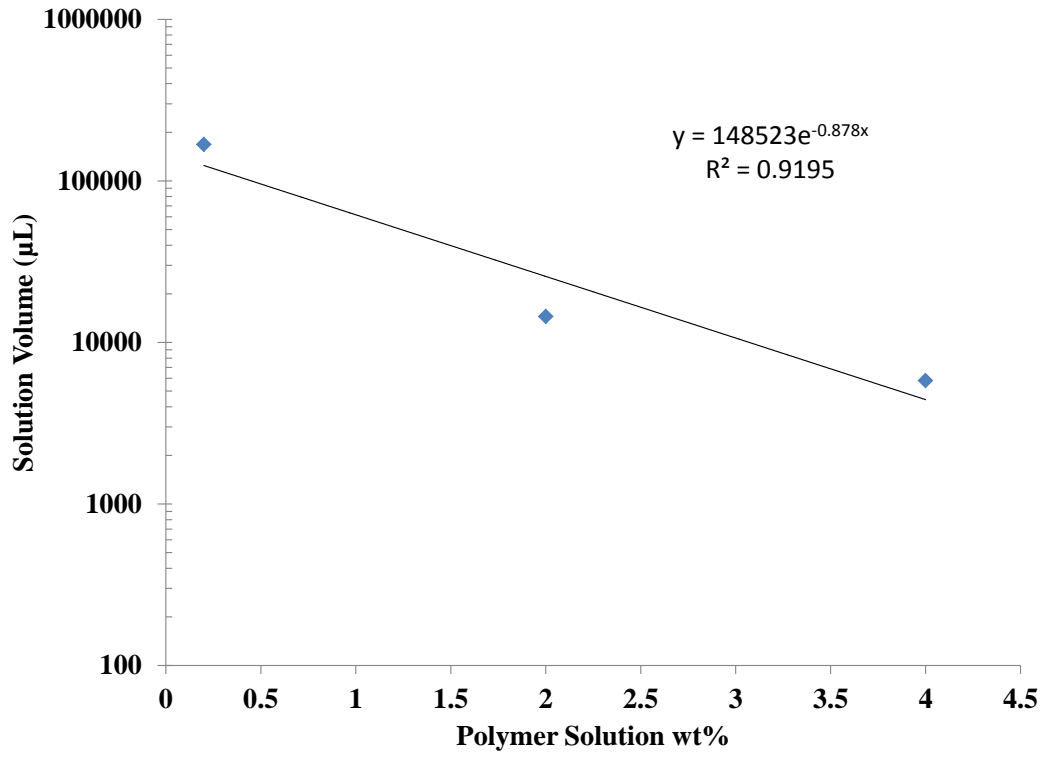


**Figure 24** Solution volume requirements as a f (solution wt%)

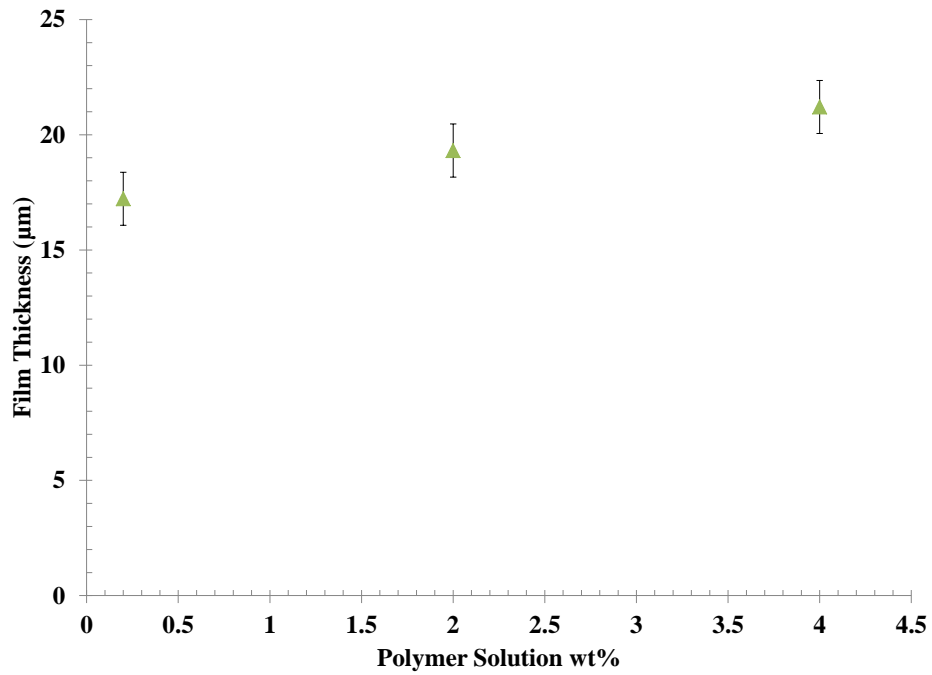


**Figure 25** Average polymer film thickness as a f(solution wt%)

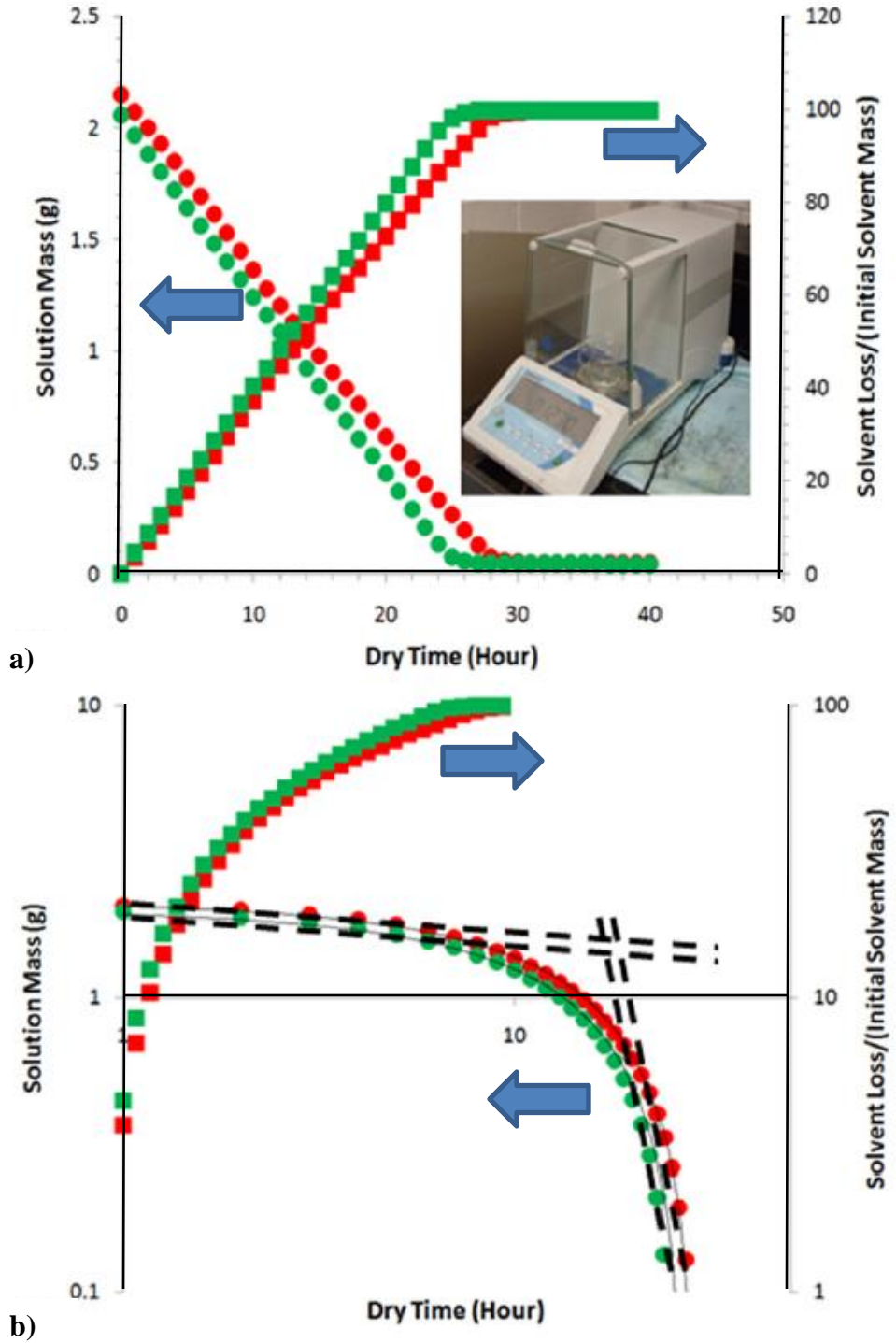


**Figure 26** Solvent evaporation measurement set-up (inset) and data in a) normal and b) log scale

The set-up for the gravimetric testing has been shown below in Figure 26. The set-up shown was specifically designed to capture the solvent evaporation dynamics in situ during drying. The mass loss plot shown here presents the data from two viewpoints. The left-y axis depicts the realtime solution loss data and it is essentially very clear that the slope of the curve is about 0.06g/hour. The right y-axis on the other hand shows the solvent loss normalized wrt initial solvent mass. Also shown is a log scale plot of the dataset and we see that the film takes between 30-34 hours to completely dry out.

The drying process occurs at a constant temperature of  $20 \pm 5^\circ\text{C}$ . The fundamental mechanism behind the drying could be explained from a standpoint of the thermodynamic equilibrium between THF vapor and liquid solution phases. The literature reported vapor pressure of tetrahydrofuran vapor as it evaporates at room temperature is 19.7 kPa [67]. With our sample, the vapor /solution equilibrium exists only as much as 10-12 hours. This is better understood if we consider Raoult's law of partial pressures for an ideal solution where the net vapor pressure is a simple summation of the component vapor pressures. At room temperature, the contribution to the vapor pressure term for a pure solvent is only due to the solvent molecules. With a solute like a polymer, the solution vapor pressure will be lowered.

For our case, the vapor pressure of the solution changes as a function of evaporative loss to the ambient. This is because as the solvent evaporates from the solution, the solution increases in viscosity and the polymer prevents some of the solvent from evaporating through sorption. At a constant temperature and fixed solvent loss rate, this solvent content increases with the increase in the amount of solution poured in to the mold. Further, the net mass of the film samples were examined prior to and after exposure to

vacuum at room temperature for almost 20 hours after peel off. The film weight loss was zero indicating that almost 100% of the solvent was driven out during the ambient drying.

#### **5.4.2 DMAC Films**

For the entire set of cast DMAC/THF and all other atomized films, the residual solvent present in the films evaporated over a period of 7 days. After this time period of 7 days, the film mass did not change in the third decimal 0.001g.

#### **5.5 Optical Microstructure Results**

Representative 40X optical images of the thin films are shown in Figures 27-39. Figures 27-29 refer to the 0.2% films that have been respectively synthesized at 23%, 29% and 37% energies of atomization but at 45°C and 150 $\mu$ L/min. From our droplet diameter datasets, we already know that at low flow rates of 50 $\mu$ L/min the droplets tend to maintain their shape very distinctly on the substrate. Due to the lower surface tension of the solution, large number of droplets participated in collisions, coalescence, splitting, deposition and drying. The net result was that for all three cases, there were droplet type impressions on the film surface. To the naked eye these films had a subtle difference with typically the larger energy value films appearing to have a fine stained glass like appearance.

Figures 30-34 depict 2% film images processed under several conditions. The only difference between Figures 30 and 31 was the flow rate used for fabrication. All other variables such as energy of atomization (29%) and temperature (45°C) were the same. The differences between the two images were hard to detect but what was evident was the presence of larger droplets in both cases, adding credence to the earlier finding that

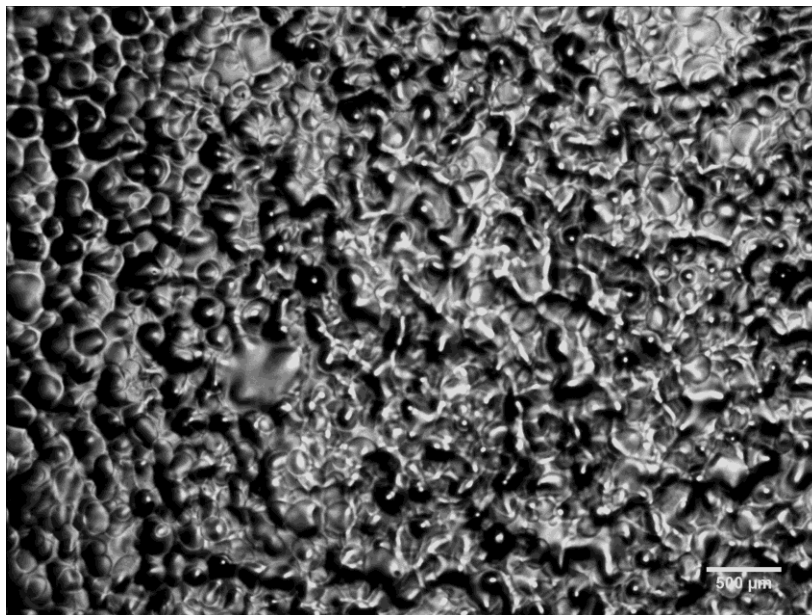


**Figure 27** 40X image of the 0.2% film (23% energy, 45°C, 150 $\mu$ L/min).

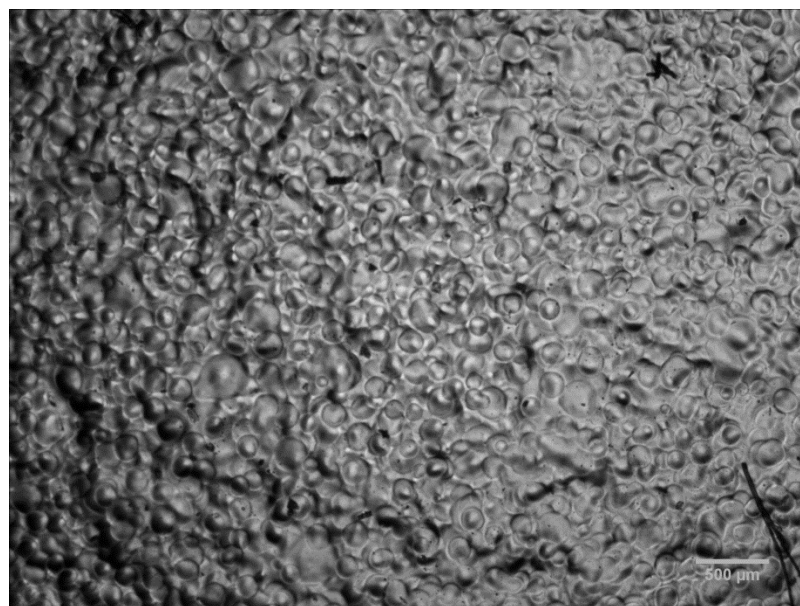


**Figure 28** 40X image of the 0.2% film (29% energy, 45°C, 150 $\mu$ L/min)

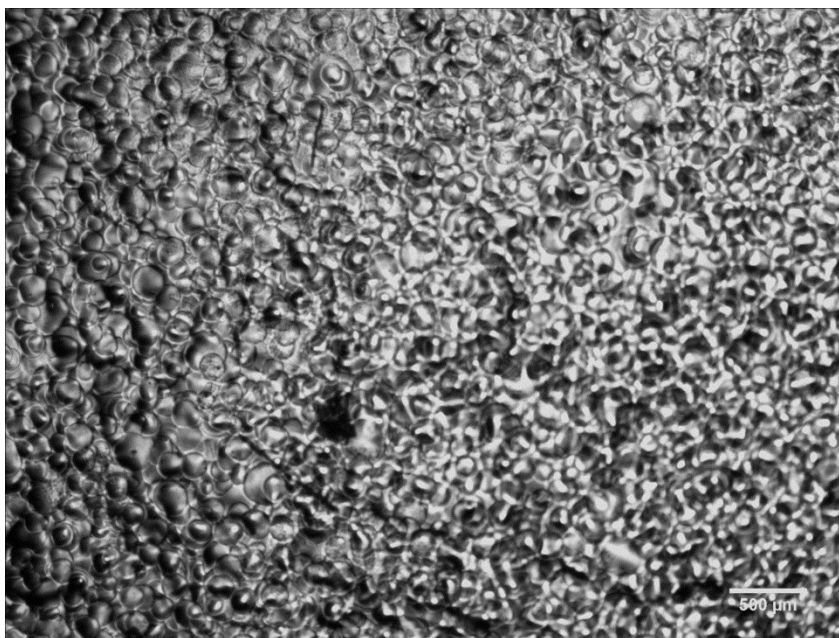


**Figure 29** 40X image of the 0.2% film (37% energy, 45°C, 150μL/min)

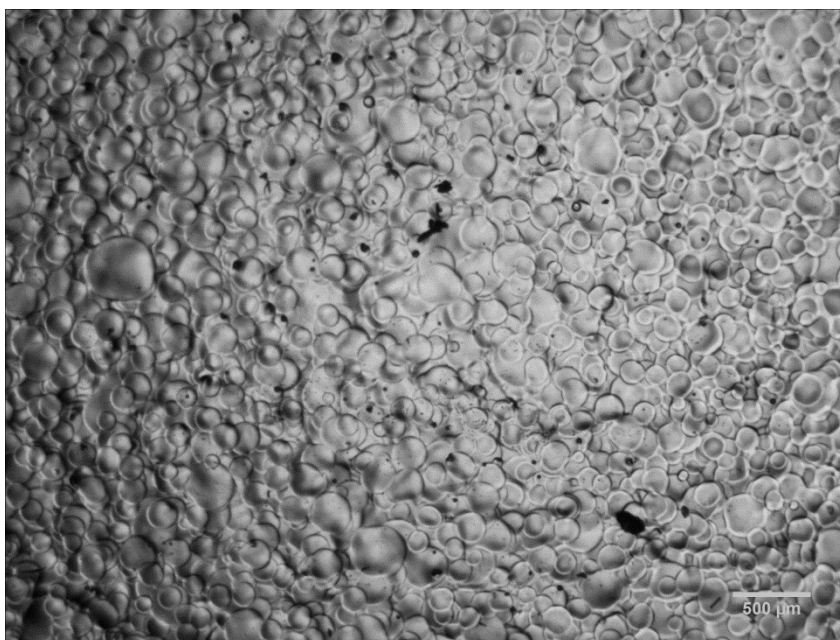


**Figure 30** 40X image of the 2% film (29% energy, 45°C, 50μL/min)

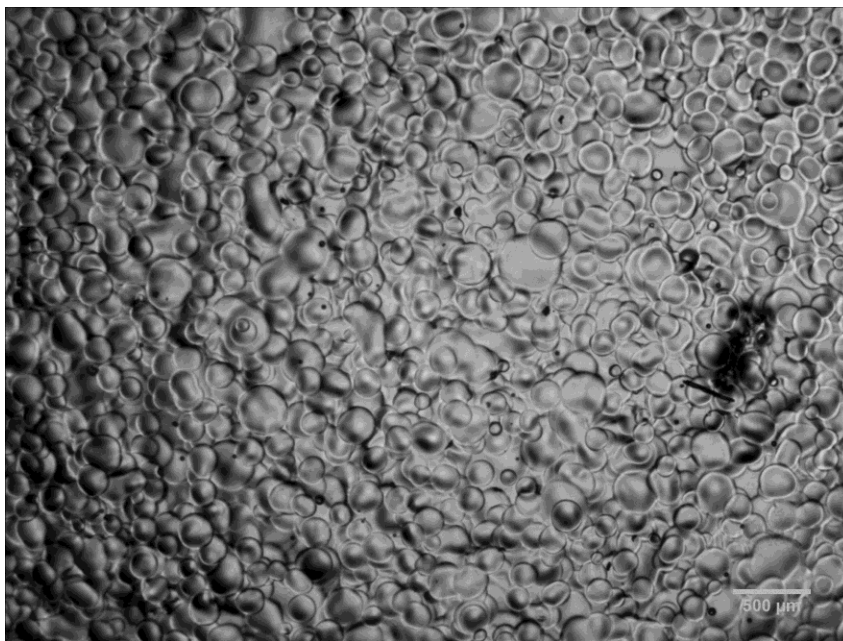


**Figure 31** 40X image of the 2% film (29% energy, 45°C, 150μL/min)



**Figure 32** 40X image of the 2% film (29% energy, 80°C, 150μL/min)

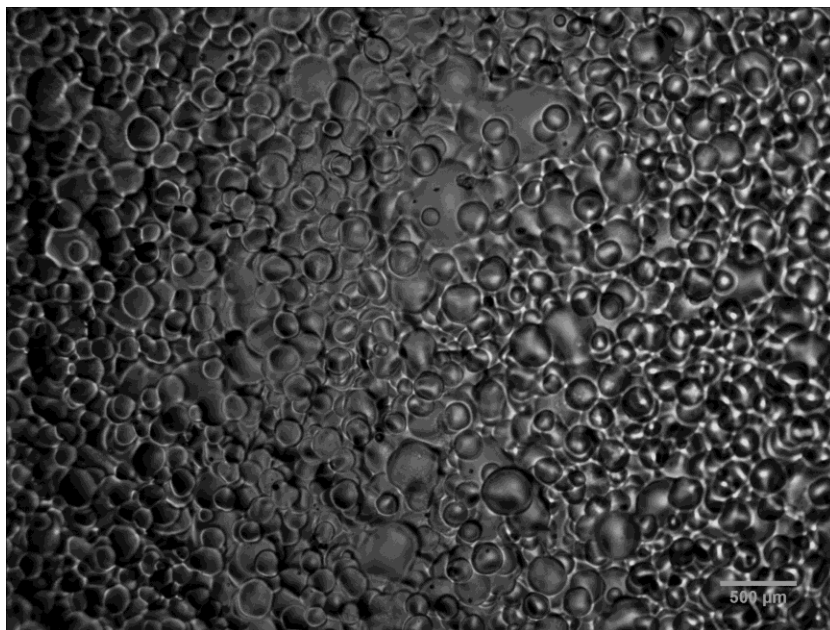


**Figure 33** 40X image of the 2% film (37% energy, 45°C, 150μL/min)

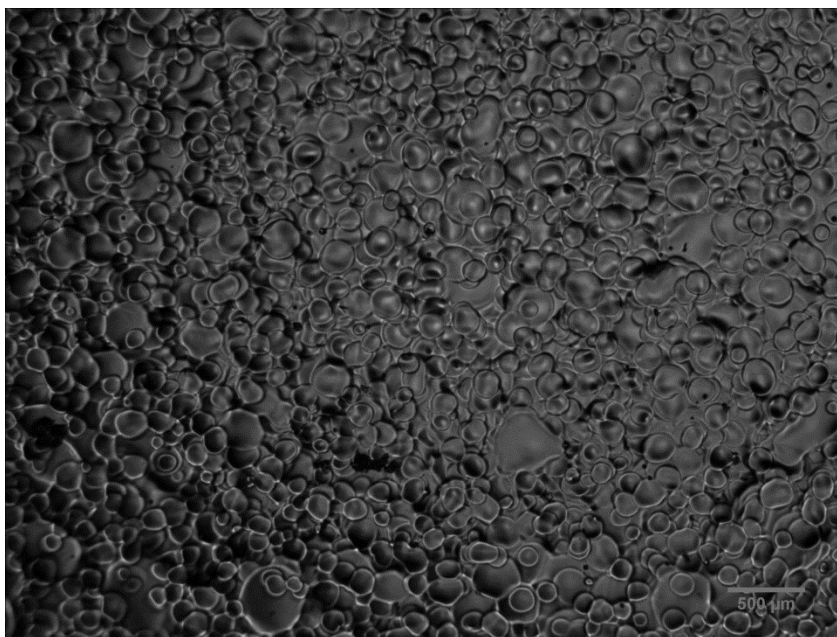


**Figure 34** 40X image of the 2% film (46% energy, 45°C, 150μL/min)



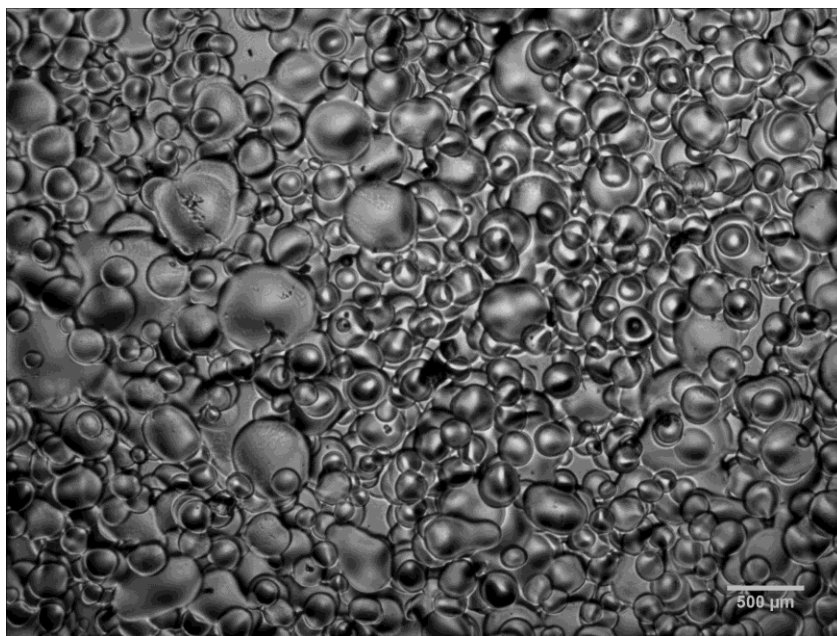


**Figure 35** 40X image of the 4% film (37% energy, 45°C, 50μL/min)

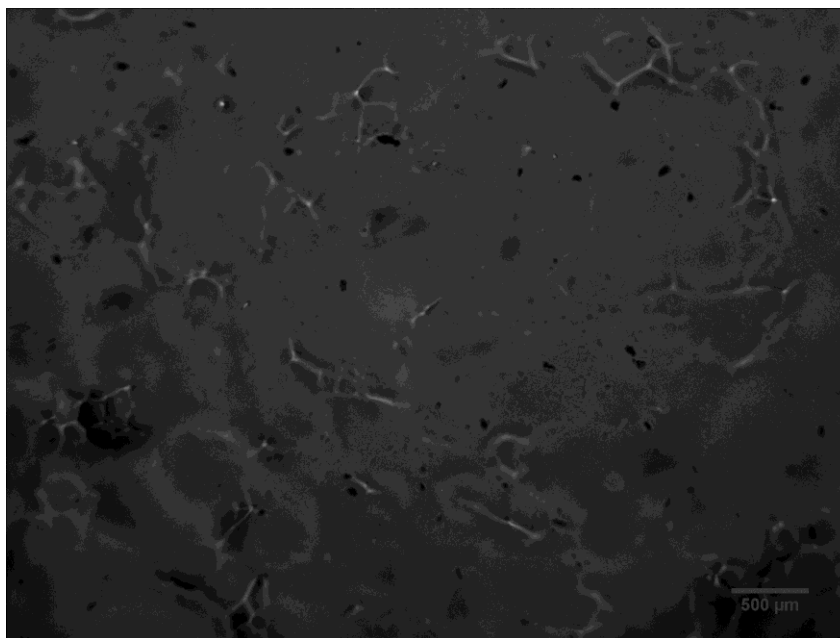


**Figure 36** 40X image of the 4% film (37% energy, 45°C, 150μL/min)

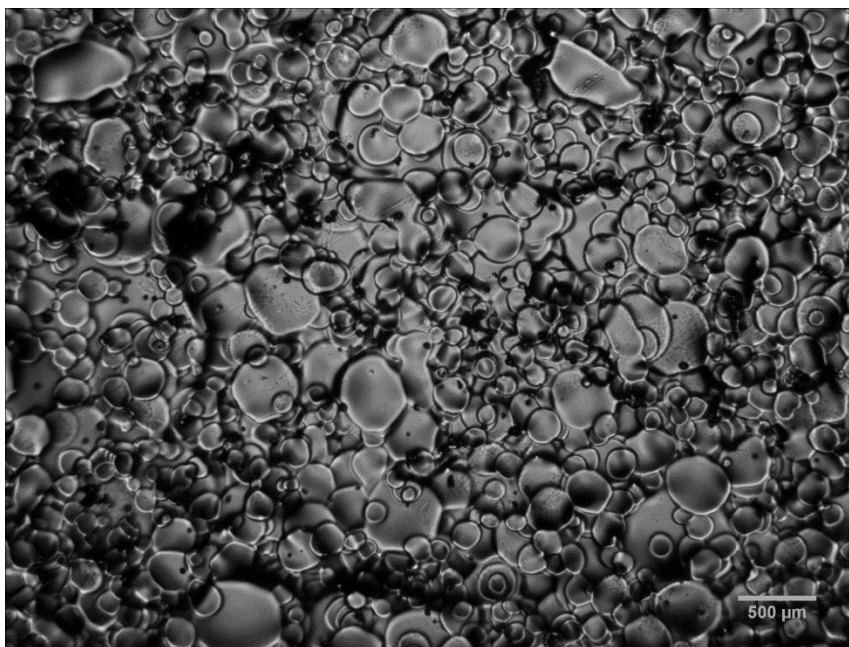


**Figure 37** 40X image of the 4% film (37% energy, 80°C, 150μL/min)

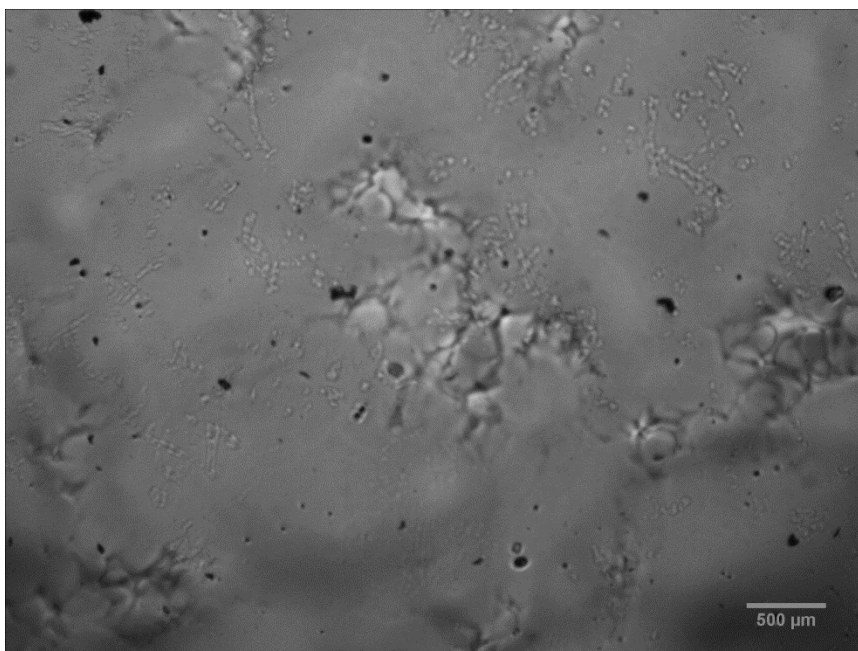


**Figure 38** 40X image of the 4% film (46% energy, 45°C, 150μL/min)

flow rate seemed to impact 0.2 and 2% more than 4%. Figure 32 was an image of a sample made at 80°C and at a flow rate of 150 $\mu$ L/min. This sample resembled some of the 0.2% film images in the sense that more number of smaller droplet type impressions was visible. Such a response was not entirely surprising as at 80°C, the chances of the solvent evaporating before extensive coalescence took place was more than in the case of the 45°C film. Figures 33 and 34 were images of the samples fabricated at progressively higher energies of atomization of 37% and 46%. All other conditions such as flow rate (150 $\mu$ L/min) and temperature (45°C) were the same. Compared to Figure 31, there were more incidences of larger droplets having coalesced with smaller droplets. This implied that for the same surface tension of the polymer solution, an increase in the energy increased the droplet diameter. The increasingly violent outbursts of the capillary wave that sheared the liquid film had a wavelength larger than the ones for the minimum energy case.

Figures 35-38 depict the 4% film images. Figures 35 and 36 were the cases of two different flow rates of 50 $\mu$ L/min and 150 $\mu$ L/min with the temperature (45°C) and energy of atomization being the same. Figure 35 displays a microstructure with more incidences of larger droplets than any of the other solution weight percents displaying clearly the combined influence of surface tension (being higher for surfaces to form) and higher viscosity (requiring a capillary wave of larger wavelength to destabilize the liquid film. In Figure 36 at 150 $\mu$ L/min, the sample surface approaches that of a surface devoid of any droplet type impressions. This is likely a result of a large population of larger droplets that take more time to dry. A featureless surface was also the case in Figure 38, even at the higher energy of 46%. Interestingly, Figure 37, which was 80°C, flow rate

150 $\mu$ L/min and energy of 37% was equivalent to the lower flow rate (Figure 38, 50 $\mu$ L/min) sample image. Over a long period of time, 150 $\mu$ L/min was just too high a flow rate for droplet impressions to remain on the surface.

## Chapter 6.

### THIN FILM MATERIAL CHARACTERIZATION

#### 6.1 Mechanical Test Results

##### 6.1.1 Cast THF Films

Representative plots of the stress-strain curves have been shown in Figure 39 for the case of 2% THF based TPU films tested at 5 mm/min. All of the film responses have a small elastic region beyond which they began to yield and at a strain of about 1.8, there was observed tendencies for the films to strain harden [68]. Finally, as the film deformed towards fracture, the overall failure event was in the form of tearing. Figures 40-42 show the observed trends in the fracture strains, fracture strengths and fracture toughness values at two different strain rates of 5mm/min and 10 mm/min. The datasets indicated that with increase in the ultrasound exposure time to 30 minutes, the fracture strains initially reduced in value, but as the time of exposure increased to 60 and 90 minutes, the strain values increased further. The fracture strength on the other hand showed a similar initial reduction in value but showed an increase for 60 and 90 minutes resulting in the same value as that of an unsonicated film. Again, any improvements were marginal. The fracture toughness showed a trend where the values increased gradually with increase in the sonication time. There was a possibility that exposure to ultrasound changed the H and S segment length distributions and the nature of the phase mixed microstructure [68]. Also, the H domains may be getting aligned in the direction of tensile testing resulting in the strain hardening behavior.

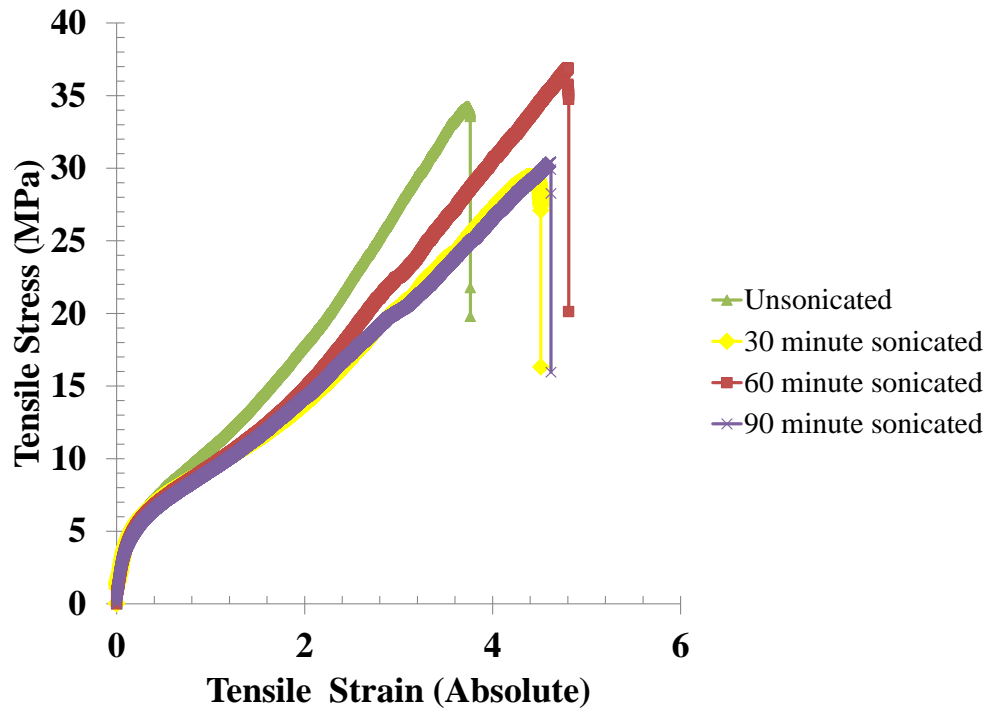


**Figure 39** Bath sonication dependent trends in the tensile response

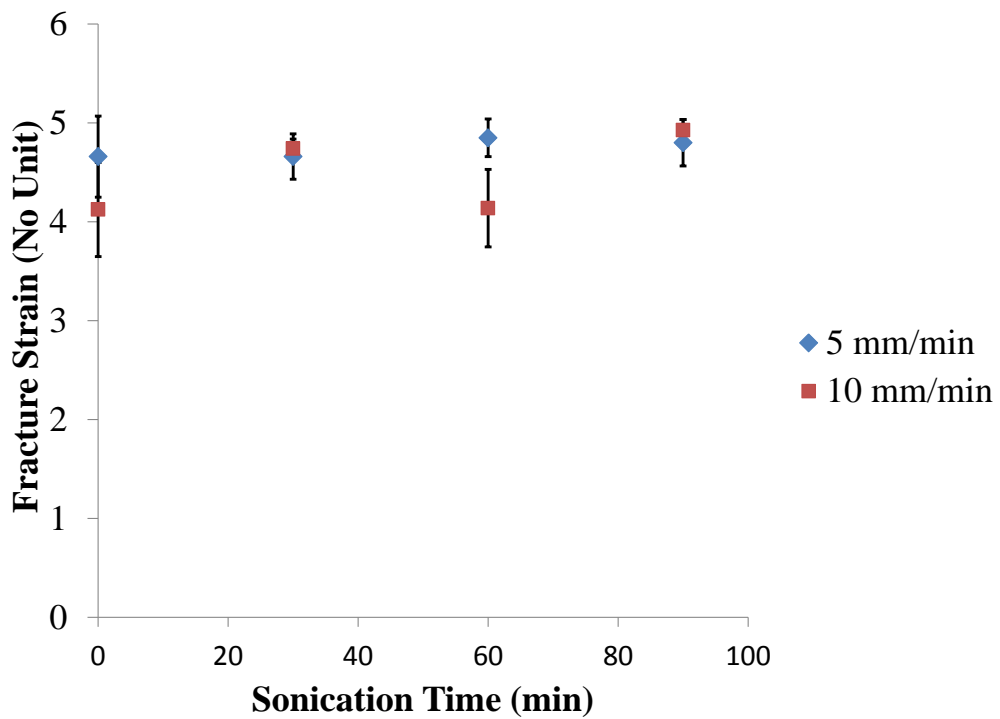


**Figure 40** Fracture strain as a f(sonication time)

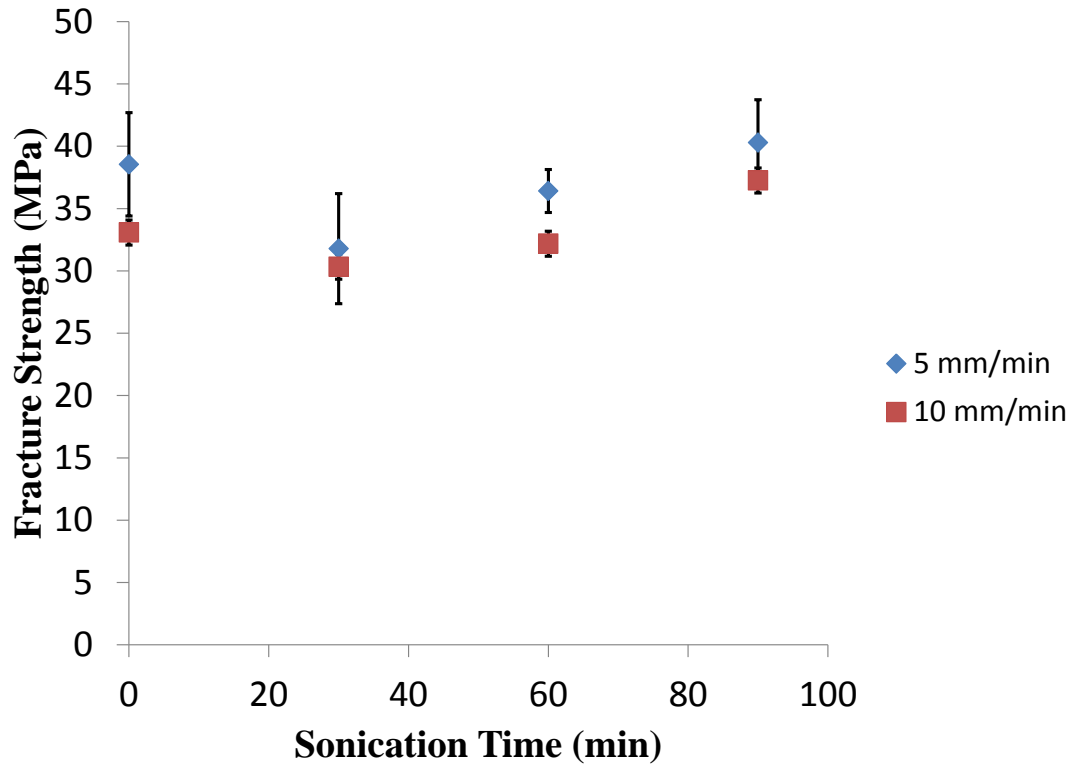


**Figure 41** Fracture strength as a f(sonication time)

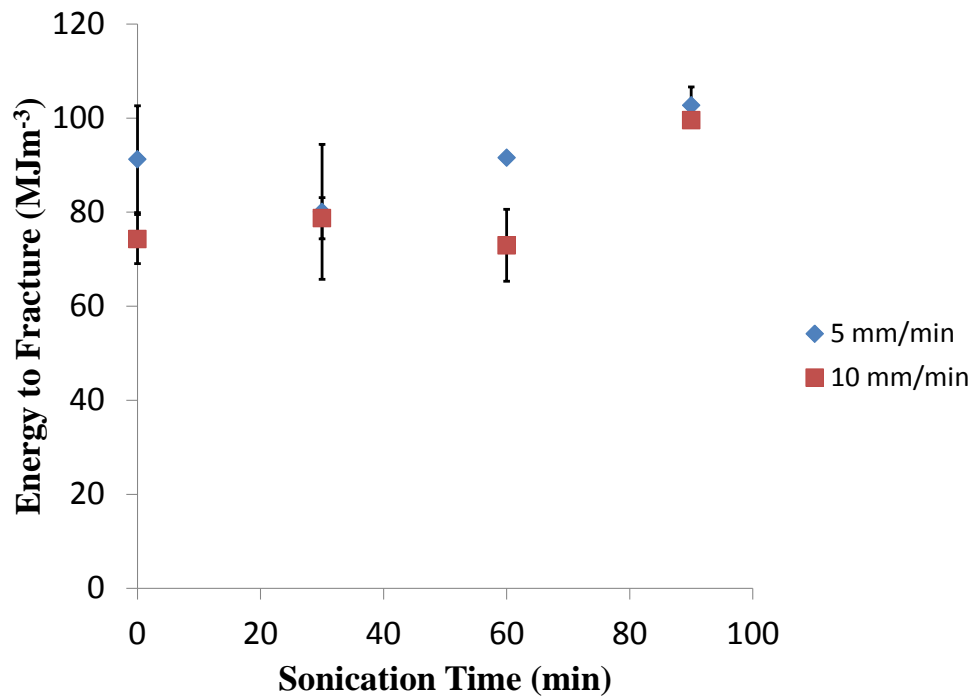


**Figure 42** Fracture toughness as a f(sonication time)

Further, 10 mm/min responses were slightly lower than the 5 mm/min responses implying that the 5mm/min films had greater time to strain harden than the 10 mm/min samples. In all of these tensile tests, care was taken to achieve failure at the gage. This was dependent on loading the films carefully into the grips without kinking or distorting them due to misalignment. The mica film rig helped in resolving these issues. Further, since the grips were screw actuated, care was taken to turn the screws by the same number of revolutions on either sides. Despite these protocols, some samples did fail outside of the gage, however their mechanical properties were comparable to those that failed in the gage.

### **6.1.2 Cast and Atomized DMAC/Atomized THF Films**

Sample stress strain curves have been shown in Figure 43 for a 2%, 45°C, 150 $\mu$ L/min sample. These curves were typical of the shape of the tensile stress-strain curve that was observed for almost all of our samples. They have a tiny elastic region followed by an almost linear increase in the stress for a given strain. The only different responses have been shown in Figure 44 and they fractured at low strengths. Fracture strains, fracture strengths and fracture toughness values for 5mm/min tested films have been averaged with standard deviation bars and plotted in Figures 45-47. The number of samples tested for each type (N) has been shown in the figures. In cases where repeatability was an issue, at least five samples were tested to determine the accurate responses. Sample types 1 and 2 were the samples generated at the two different flow rates of 50 and 150 $\mu$ L/min and 45°C. Sample type 3 was the sample generated using THF. Sample types 4 were the solution-cast controls and sample type 5 was the set of films manufactured at 80°C, 150 $\mu$ L/min. Sample types 6 and 7 were both generated at



150 $\mu$ L/min, 45°C. In Samples 6 and 7, the atomization energy amplitude was increased to values higher than their minimum energy of atomization (23% for the 0.2% sample, 29% for the 2% sample, 37% for the 4% sample).

For the 0.2% samples, as a function of energy of atomization, there was no specific increase or decrease in the fracture strengths, fracture strains and toughness values. However, a dramatic drop in the fracture strength, fracture strain and fracture toughness occurs at the higher temperature of 80°C. For the 2% samples, we see a progressive increase in fracture strength, fracture strain and fracture toughness values. While the property values for the 2% samples were comparable between the two different flow rates used; as a function of temperature, their strengths, strains and toughness values increased. For the 4% films, similar to the 0.2% films, there was a decrease in the properties of the films as a function of test temperature. As a function of flow rate, these property values were very comparable. As a function of energy, there was an increase in the toughness values but not with the strengths or strains.

Also shown in Figures 48-50 are the 50mm/min responses for a selected set of samples. Again, the number of samples tested for each type (N) has been shown in the figures. Especially, we were interested in the influence of temperature and energy of atomization. In all cases, we see an increase in the fracture strength and slightly reduced strains due to the higher strain rate of testing. Just as in the 5mm/min samples, the strengths, strains and toughnesses were reduced as a function of test temperature for the 4% films. Also, as a function of energy of atomization, similar trends in the improvements in strengths, strains and toughnesses were seen for the 2 and 4% samples. But for the 0.2% samples,

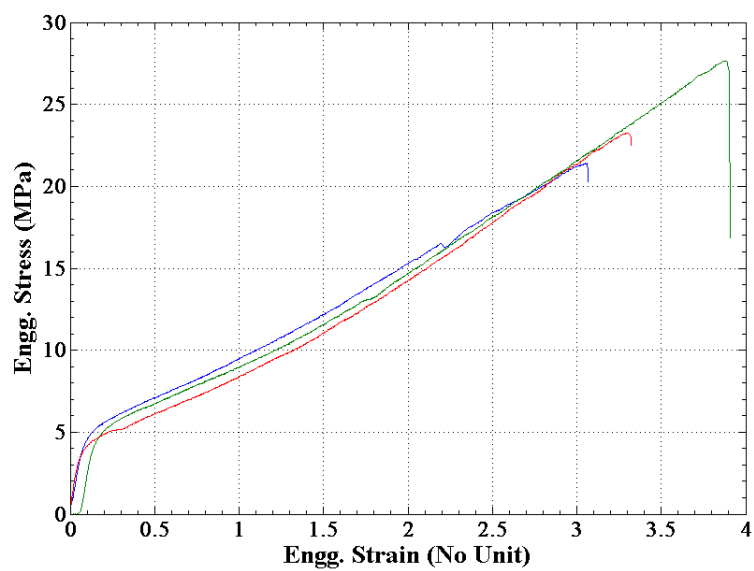


**Figure 43** Example stress-strain plots for the case of a 2% atomized film made at 45°C, 150 $\mu$ L/min and 29% energy

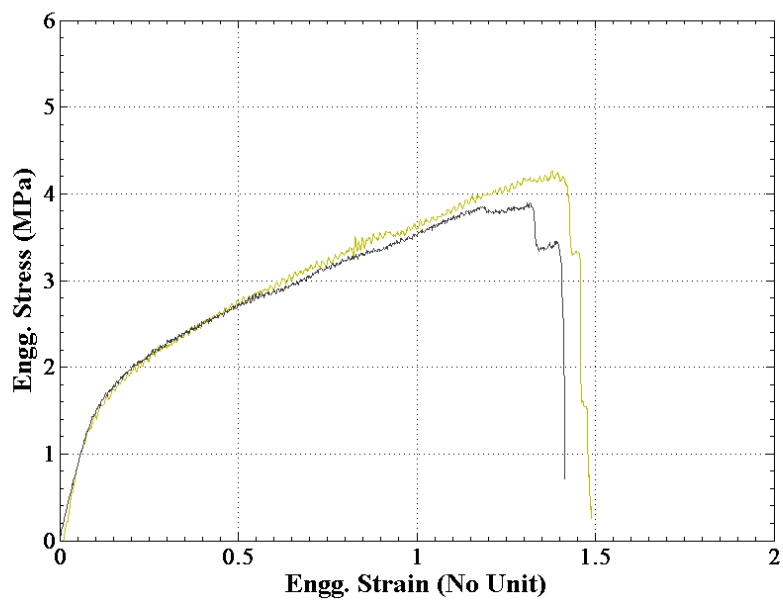


**Figure 44** Example stress-strain plots for the case of a 2% atomized film made from THF at 45°C, 350 $\mu$ L/min and 23% energy

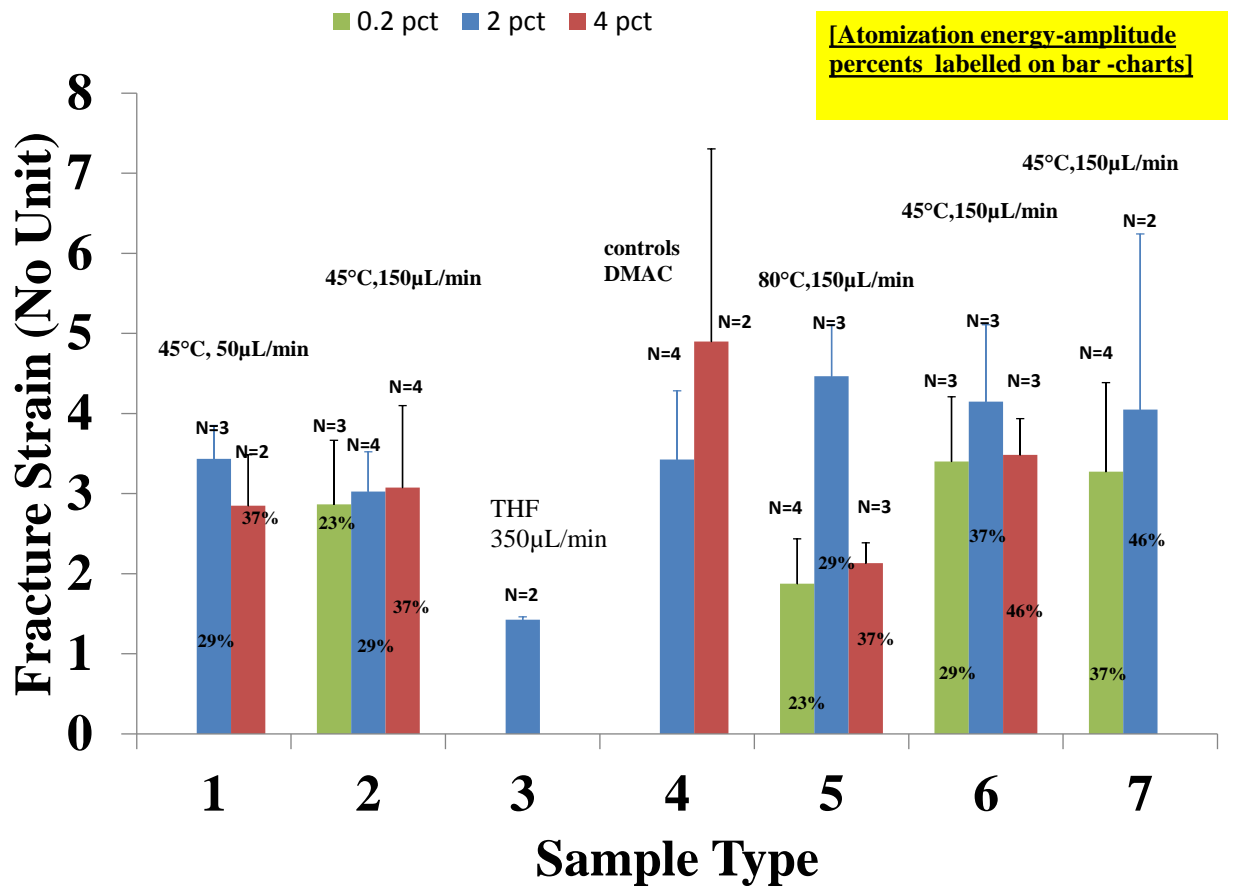
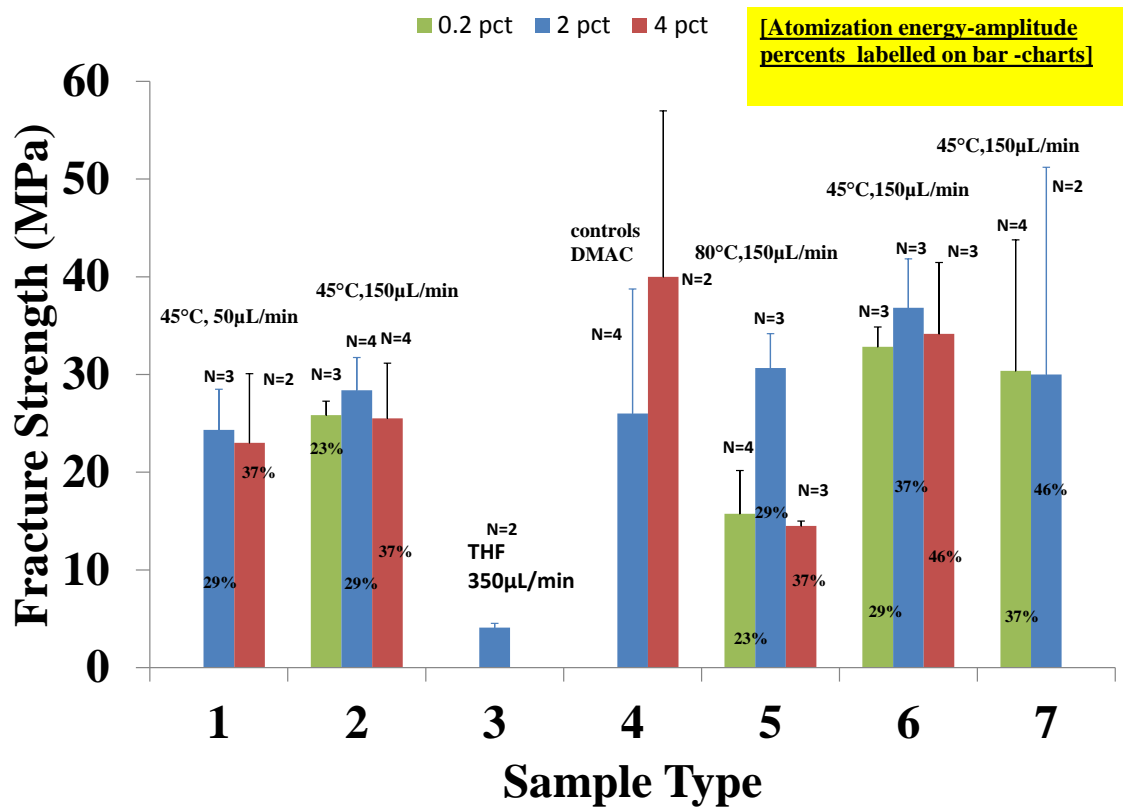


Figure 45 Computed fracture strains for all samples tested at 5mm/min



**Figure 46** Computed fracture strengths for samples tested at 5mm/min

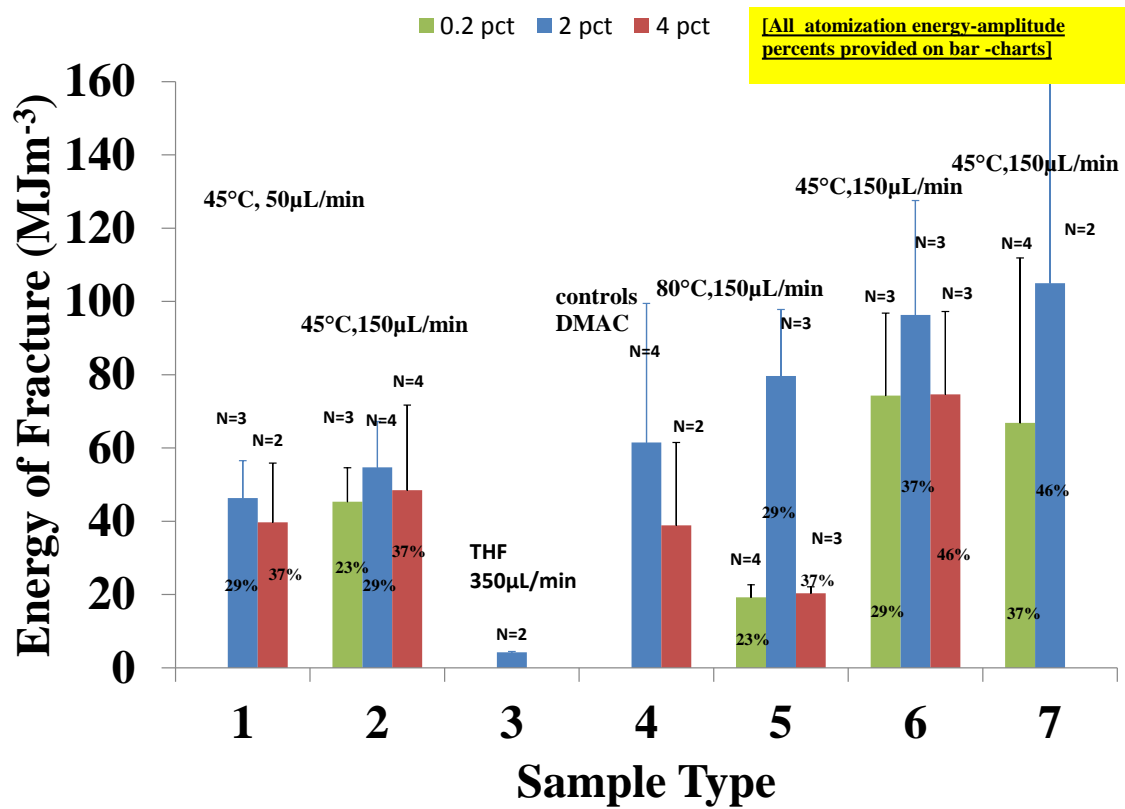


Figure 47 Computed energies of fracture values for samples tested at 5mm/min

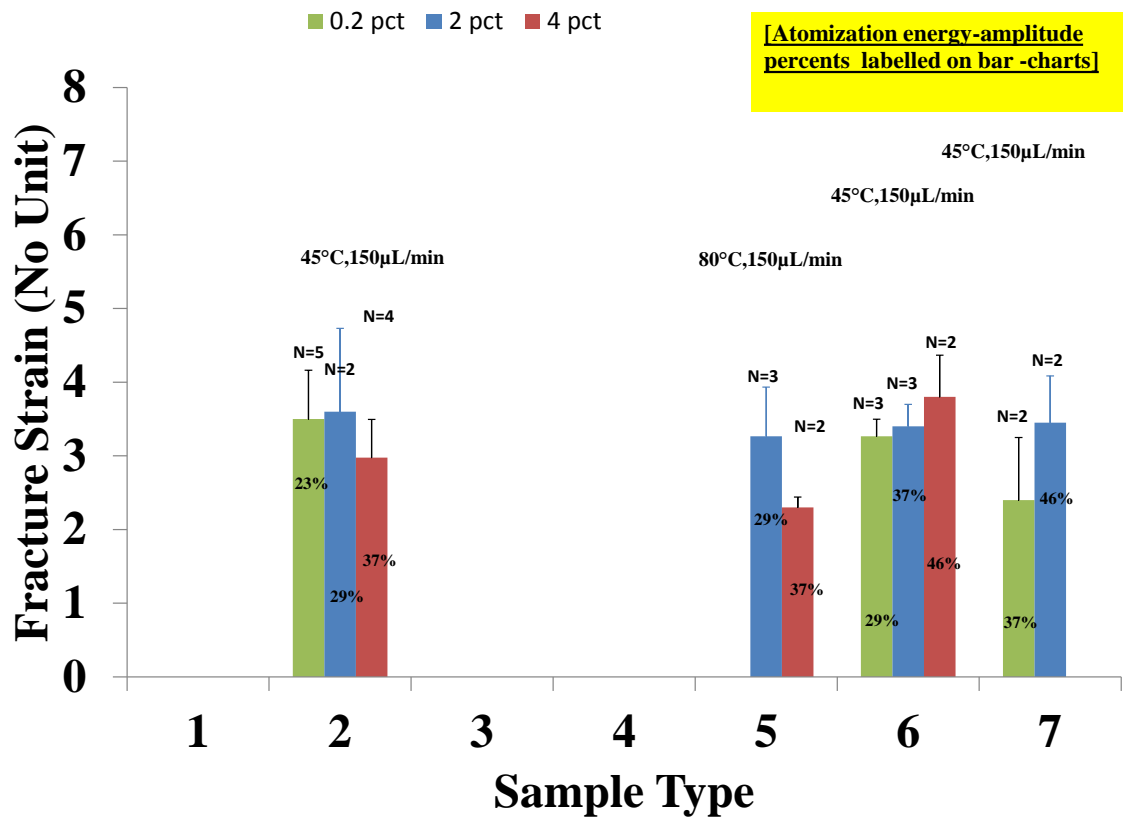
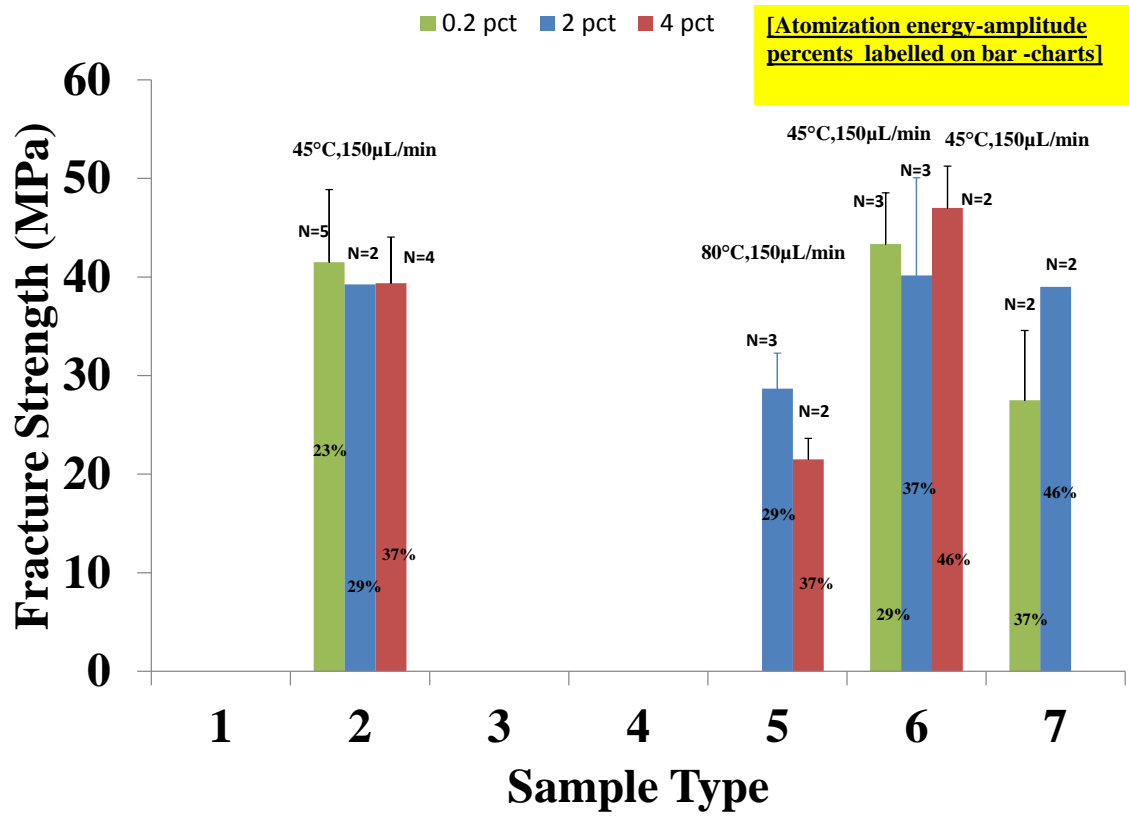


Figure 48 Computed fracture strains for all samples tested at 50 mm/min



**Figure 49** Computed fracture strengths for all samples tested at 50 mm/min

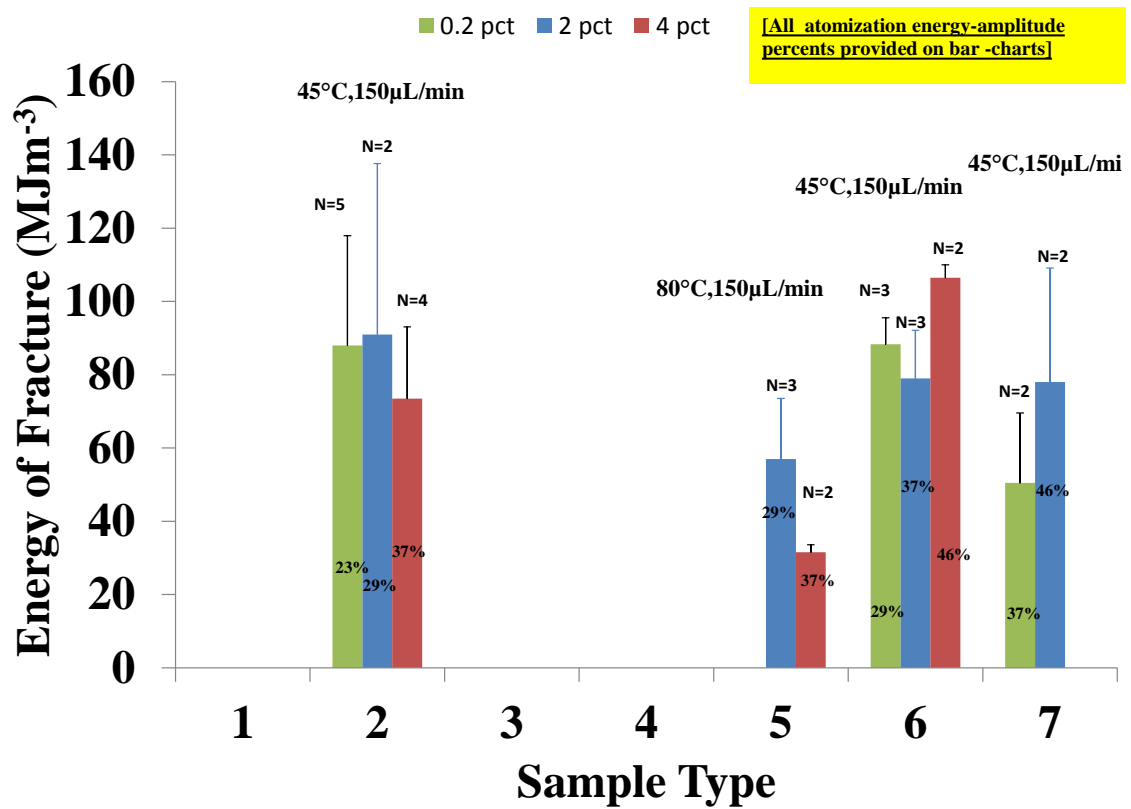


Figure 50 Computed energies of fracture for all samples tested at 50 mm/min



these properties actually decreased as a function of energy of atomization. Relating these property responses to the processing conditions, there seems to be an overall trend where the atomization energy either increased properties or provided films with comparable properties. As a f(temperature), the time of exposure of the film (for a 0.2% samples versus a 4% film) had a negative effect on the sample's properties.

## 6.2 Differential Scanning Calorimetric Data

For the sake of attaching meaningful legends to the DSC data and other datasets to follow, a naming convention has been adopted.

*<wt%><energy E> <temperature T>S<number of layer of deposition>*. E1=minimum energy of atomization for that weight percent film. (for 0.2% this was 23%, for 2% this was 29% and for 4% this was 37%). E2= the next highest energy of atomization considered. These values were 29% energy for 0.2%, 37% energy for 2% and 46% energy for 4%. E3=the atomization energy tested was 37% for 0.2% and 46% energy for 2%. T2=45°C, T4=80°C. The word S just indicated that the substrates were spun continuously by the spin coater at 100 RPM and the number following S was indicative of the number of layers deposited.

A sample DSC curve has been shown in Figure 51. Glass transition is a second order transition that manifests itself in a step-change in the heat capacity. As shown in Figure 52, the glass transition temperature itself was taken as the average of the onset and final temperature of the step-change in heat capacity. Melt transitions are first-order transitions that appear in the form of a peak in the heat capacity curve. The area under

Sample: M-DSC-iv-2  
Size: 1.2000 mg  
Method: Tg scan twice  
Comment: junk

DSC

File: C:\...DSC 2012\Repeats\M-DSC-iv-2.001  
Operator: Brian Grady  
Run Date: 07-Apr-2012 17:26  
Instrument: DSC Q1000 V8.1 Build 261

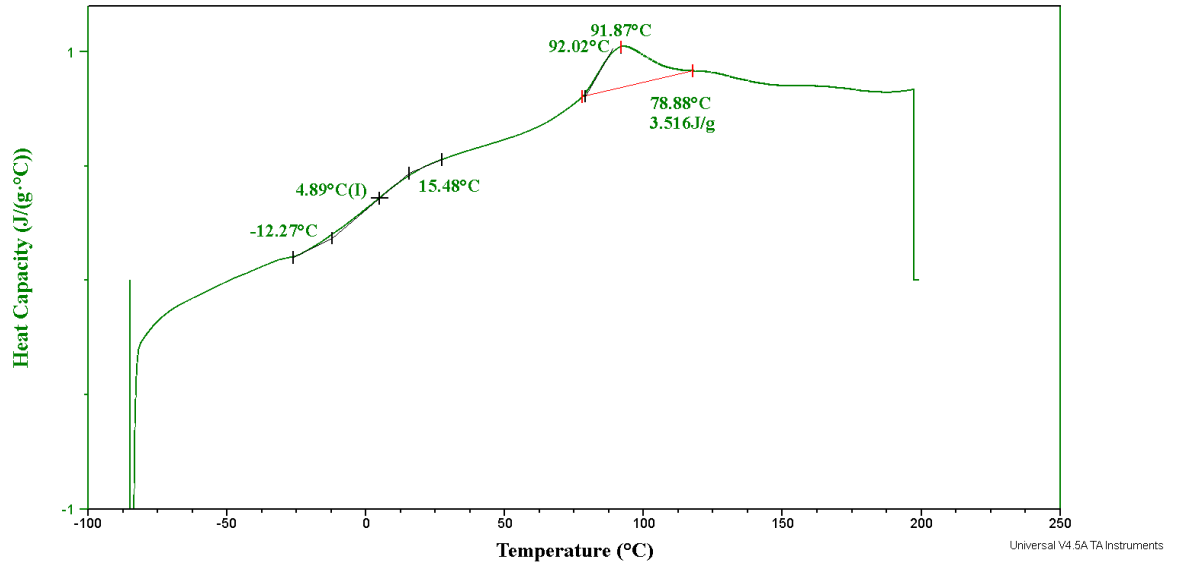


**Figure 51** Sample DSC Curve for a 45°C, 4%, 37% energy, 150µL/min film

**Table 8:** Glass and melt transitions for all the DMAC based samples from this work

Process Condition	$T_g$ (°C)						$T_m$ (°C)	$\Delta H_{\text{fusion}}$ (J/g)	$T_m$ (°C)	$\Delta H_{\text{fusion}}$ (J/g)	$T_c$ (°C)	$\Delta H_{\text{crystal}}$ (J/g)
	Onset	Mid	End	Onset	Mid	End						
2E1T250S11	-13.3	-7.3	9.4	-	-	-	85.6	3.6	134.1	0.4	-	-
2E1T2150S12	2.2	14.1	27.8	-	-	-	89.8	4.2	122.9	0.5	-	-
2E1T4150S11	-0.4	5.9	15.0	-	-	-	89.8	2.6	-	-	-	-
2E2T2150S10	-3.4	-3.5	13.4	-	-	-	87.7	3.4	120.6	0.4	-	-
2E3T2150S10	-8.7	2.2	18.0	-	-	-	87.4	2.8	125.8	0.2	-	-
2T2-Control-Cast	4.7	16.0	27.1	65.2	67.6	82.3	110.4	4.7	-	-	-	-
4E1T250S4	-6.8	-6.5	8.2	-	-	-	87.7	3.5	-	-	-	-
4E1T2150S4-1	1.0	1.5	10.8	-	-	-	89.3	5.7	-	-	-	-
4E1T2150S4-2	-17.4	-5.6	14.7	-	-	-	92	3.3	-	-	-	-
4E1T4150S4	-4.9	1.5	7.5	-	-	-	89.1	3.1	-	-	-	-
4E2T2150S4	-11.4	-2.0	16.6	-	-	-	88.4	4.9	-	-	-	-
4E1T2-Control-Cast	-7.4	5.2	17.2	-	-	-	114	2.9	-	-	-	-
0.2E1T2150S116	-1.8	7.5	22.0	-	-	-	86	3.8	118.2	0.4	-	-
0.2E1T4150S120	-11.1	-5.6	2.9	-	-	-	86	2.7	112.2	1.2	-	-
0.2E1T4150S121	-12.9	-5.2	3.1	-	-	-	85.7	2.5	136.6	1.5	-	-
0.2E2T2150S120	-12.2	-3.0	18.4	-	-	-	90.2	3.1	131.4	1.4	-	-
0.2E3T2150S138	-7.1	-0.8	9.1	-	-	-	86.5	2.1	-	-	145.9	3.2
Pellet-1-As-is	-	-	-	-	-	-	80.1	3.9	-	-	-	-
Pellet-2-As-is	-	-	-	-	-	-	78.7	5.6	-	-	-	-

**Table 9:** Glass and melt transitions for all the THF based samples from this work

Process Condition	$T_g$ (°C)						$T_m$ (°C)	$\Delta H_{\text{fusion}}$ (J/g)	$T_m$ (°C)	$\Delta H_{\text{fusion}}$ (J/g)	$T_c$ (°C)	$\Delta H_{\text{crystal}}$ (J/g)
	Onset	Mid	End	Onset	Mid	End						
2-Control-Cast-THF-1	-8.2	8	20.4	66.7	73.7	80.2	-	-	130.8	4.1	-	-
2-Control-Cast-THF-2	-13.3	8	25	66.1	73.4	79.9	-	-	137.2	6.4	-	-
2-Son-30-Cast-THF-1	-11	3.8	16.8	64.7	73.7	81	-	-	138.9	6.4	-	-
2-Son-30-Cast-THF-2	-11.4	7.7	23.2	65.7	71.5	79	-	-	137.4	4	-	-
2-Son-60-Cast-THF-1	-12	7.8	21.7	68.8	74.3	79.2	-	-	140.6	2.6	-	-
2-Son-60-Cast-THF-2	-9.2	-0.5	15.6	66.8	70.3	77.3	-	-	142.1	6.4	-	-
2-Son-90-Cast-THF-1	-13	0.5	17.2	67.9	74.2	80.2	-	-	140.7	0.2	-	-

the peak was obtained after fixing a straight line joining the onset and end points of the melt transition part of the curve and integrating the difference between this line and the peak. The area under the peak is the energy required for the crystallites present in the sample to melt and become amorphous. Transitions below  $-40^{\circ}\text{C}$  could not be successfully resolved with a degree of clarity. There was one glass transitions measured corresponding to a mixed hard-soft segment phase and one to two melt transitions observed depending on the sample. All transition temperatures and enthalpies of fusion are found in Tables 7 and 8. The as-received pellets showed no glass transitions but instead a single melting point at  $79^{\circ}\text{C}$ . The transition of the material at the lower temperatures is ascribed to rotation of the flexible soft segments due to their “reversible” elasticity owing to intermolecular hydrogen bonding [55]. The pure soft segment melting point of PTMG is about  $45^{\circ}\text{C}$ . Yet no such transition is measured indicating a large H segment composition  $> 0.3$  and also indicating mixing of segments [55, 69]. The transitions that take place at around  $80^{\circ}\text{C}$  are due to the dissociation of the intermolecular hydrogen bonds [55, 69]. These hydrogen bonds are between the soft and hard segments. Transitions that occur at higher temperatures between  $110\text{-}150^{\circ}\text{C}$  are due to the increased packing of the urethane domains and happen due to the dissociation of the bonds between them [55,69]. Further, the ordering of the urethane domains is essentially described as a pseudo crystalline behavior [55, 69].

Almost all of the samples (2%,4%) showed a melting point (mp) between  $88\text{-}90^{\circ}\text{C}$ . Only the 0.2% atomized films showed a mp between  $100\text{-}120^{\circ}\text{C}$ . Besides the wt%, the major difference between the 0.2% , 2% and 4% samples were the amounts of time it took for sample fabrication. While it took 28 hours to fabricate a 0.2% sample and all the while

the samples were in the deposition chamber at a set temperature. This was not the case for the 2% and 4% samples. While 2% samples on an average took 6 hours to synthesize, the 4% took about an hour. This leads one to think that the crystallites in dilute 0.2% samples have more time to get to equilibrium. That could potentially explain the existence of two first order transitions in the 0.2% sample. Since ultrasound energy was supplied for atomization, it was desirable to see if it had an influence on the sample preparation. The supplied energy depended on the physicochemical properties (f(wt%)) yet its influence on the values of the transitions was subtle if not noticeable. However, it seems that the high temperature transitions ( $>80^{\circ}\text{C}$ ) for the 4% samples do not exist and this could be because the urethane domains are completely disrupted. This is not the case with the THF samples. They have higher high temperature transitions between  $130\text{-}150^{\circ}\text{C}$  indicating a progressive increase in the ordering.

### 6.3 SAXS/WAXS Results

All of the SAXS results have been shown in Figures 52 through 54. The collimated X-rays in a SAX experiment get scattered by the nanometer to sub-nanometer phases in the sample. The extent of scattering depends on the electron density within the sample. Thus any maxima in the spectra imply the presence of electron rich phases such as H domains with H segments in a TPU sample. SAXS datasets show maximums corresponding to the largest domain sizes. Using Bragg's law, the hard domain size could be computed from the peak of the SAXS curves:

$$d_{domain} = \frac{q}{2\pi} \quad (25)$$

The rest of the signal has a constant scattering background (attributed to the machine itself) that needs to be subtracted before doing any analysis. Thus the drop in the signal after the maximum point represents the transition from an electron rich H to electron poor S domains. The nature of this drop in the intensity is quantified by Porod's Law [53]. The extent of phase mixing could be quantified by fitting the datasets to Porod's law where B, K and E are fit parameters and intensity to q relationship is stated as

$$I(q) = B + (K/q^4) * (1 - 2E^2q^2/3) \quad (26)$$

Knowing this relationship, the invariant Q can be found from the following equation

$$Q = \int_0^{\infty} q^2 \left( \frac{I}{I_e V} \right) dq = 2\pi^2 v_1 (1 - v_1) (\rho_1 - \rho_2) \quad (27)$$

Figures 55 and 56 show sample plots for this analysis using the Porod fit. The invariant Q is a function of sample composition v (subscript 1 for H domains and 2 for S domains and electron density  $\rho$  of a pure S (2) and pure H (1) segment. Q has been computed and tabulated but no further analysis has been determining the composition of H,  $v_1$  and S segments  $v_2$  have not been done. The tabulated data shows that the domain spacings vary between 9-12 nm. There are no specific trends within each sample group (0.2%, 2% and 4%). However between them, the invariants are generally higher for the 0.2% samples and the 2% samples relative to the 4% samples. The domain sizes are also larger for the 0.2 and 2% samples. These indicate more mixing of phases in the 4% samples than in the 2 and 0.2% samples. One of the samples is the MA THF (manually atomized THF sample using a syringe) shows lower invariant and domain spacing implying pronounced

phase mixing. The domain sizes are also lower indicative of lower levels of phase separation.

WAXS showed no evidence of major crystalline planes. No reflections were seen for the PTMG crystal (conforms with the DSC observation). No peaks were seen corresponding to the urethane domain ordering either. Other workers have reported such peaks only on oriented samples [57, 59]. So the ordering causing the melting transitions at 80°C and above was pseudo crystalline [55,69]. As a reminder, since the -NH, -C=O and -O-R all compete for H-bonding, there probably was a set number of overall bonded and unbonded urethanes that resulted in domain ordering (from an energy perspective).

#### **6.4 AFM Results**

The results of the AFM studies have been shown from Figures 57 through 84. Topographical and phase images have been shown for each case. We have reported AFM images for all samples except the 4% DMAC control and 0.2% films. All of our AFM images were analyzed using the open source software called Gwyddion [64]. The images were initially obtained as 1 μm x1 μm scans. All of these images were also subject to filtering to remove artifacts such as horizontal and vertical scars, background noise. They were then cropped into 0.6μm x 0.6μm scans to remove the edges. From the topography images, we then computed the root mean square roughness (RMS)  $R_q$  of these films in a row-wise (row) and column (col) wise fashion considering each pixel of the image as an element of a matrix. RMS roughness  $R_q$  is defined as follows.

$$R_q = \sqrt{\left(\frac{1}{N} \sum_{i=1}^N r_i^2\right)} \quad (28)$$



Basically, an average of all the height deviations  $r_i$  from the mean line is taken over a specified length. This was done over every row and every column using the statistical row/column function of Gwyddion [64]. For the phase images, we chose specific regions of the image and resolved them to a 50 nm scale without losing pixel clarity. This was done via interpolation. Once interpolated, the images were then examined carefully for the presence of H and S domains. The rules for this identification was based on the idea that a phase image shows force dependent responses of the tip-sample interaction. Thus softer parts of the sample were darker and harder parts bright. In addition, such images have been reported by other workers and our images are very similar to their images [70-72]. Once the H domains are identified, we see them aggregated together and suspended in a phase mixed matrix. These H domains were then quantified for their width. All of the topography and phase images including the roughness plots are shown in all cases. Example images are also shown for each sample identifying the H domains/aggregate of H domains with dark black lines.

In all of these images, we see that the phase image for the most part mirrors the topographic image. This was where our analysis got challenging as the actual compositional information was present in the phase image together with many of the topographic features. One of the other issues with gathering phase image data had to do with obtaining the correct set-point to free oscillation amplitude settings. Also, we could not convert the voltages in the phase image into an angle. Such a conversion would enable us to find the forces involved. Nevertheless, we were able to resolve the dimensions of the hard domains via our analysis. AFM hard domain measurements have been tabulated in Table 11. Of all the workers who investigated polyurethanes via AFM,

only Aneja and Wilkes have actually shown exceptionally clear images of the hard segments within a domain suspended in a soft segment matrix. The hard domains were carefully identified by visual inspection of the image and dark black lines represent these domains. It was only possible to measure the width of these domains with any degree of precision and these widths are in the same range as those measured using SAXS. The length of these domains was not possible to be resolved as there was evidence of significant phase aggregation.

At the microscopic level, the surface tends to get smoother as the energy of atomization was increased (2% samples: ~3nm to 0.45 nm , 4% samples: ~0.5 nm to 0.45 nm). With increase in test temperature from, 45°C to 80°C, we either see comparable or slightly higher roughness's (2% samples: ~3nm to 2 nm (4-5 nm locally rough spots also present) , 4% samples: ~0.5nm to 0.55 nm). However, the 2% control DMAC films showed a surface roughness of ~1.25 nm. The THF atomized film showed a surface where certain regions had root mean square roughness's about 1.2-1.6 nm in both row and column wise measurements. In comparison, the control unsonicated THF films showed a roughness of 1.5 nm. With increasing bath sonication time, these control THF films showed an increase in roughness up to ~4.5 nm for 30 minute films and ~3.5 nm for 60 minute films. The 90 minute films were 0.65 nm rough and smoother than the unsonicated control which was 1.5 nm. These roughness values provide us with reasoning for the trends we observed in the mechanical properties of the thin films. The films with higher roughness's had lower strengths, strains and energies to fracture.

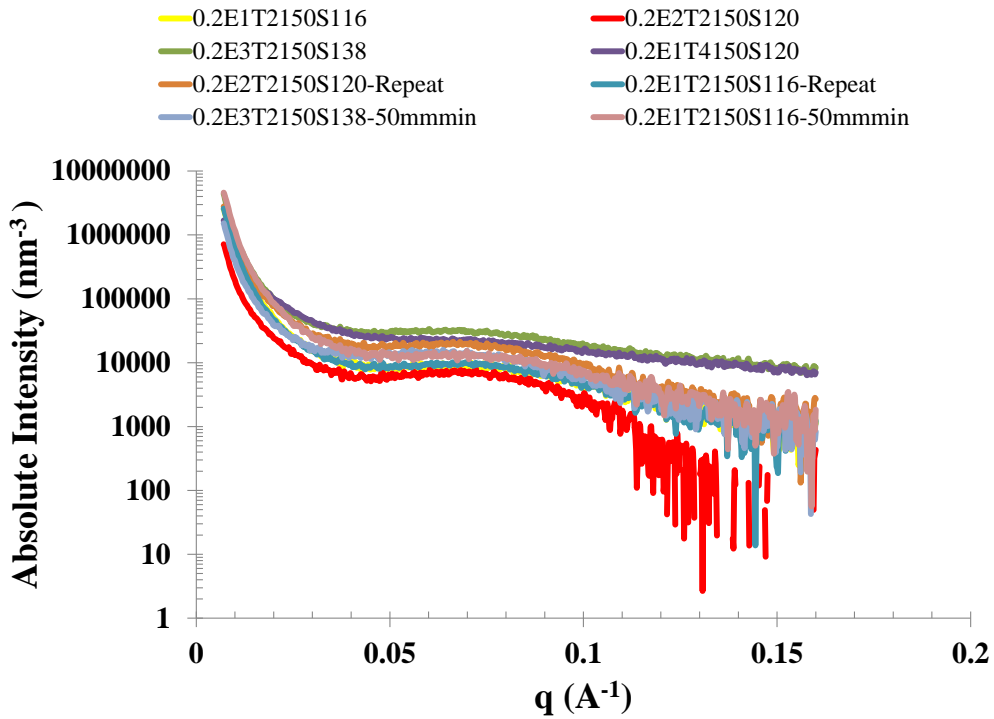


**Figure 52** SAXS intensities for 0.2% samples plotted as a function of scattering vector.

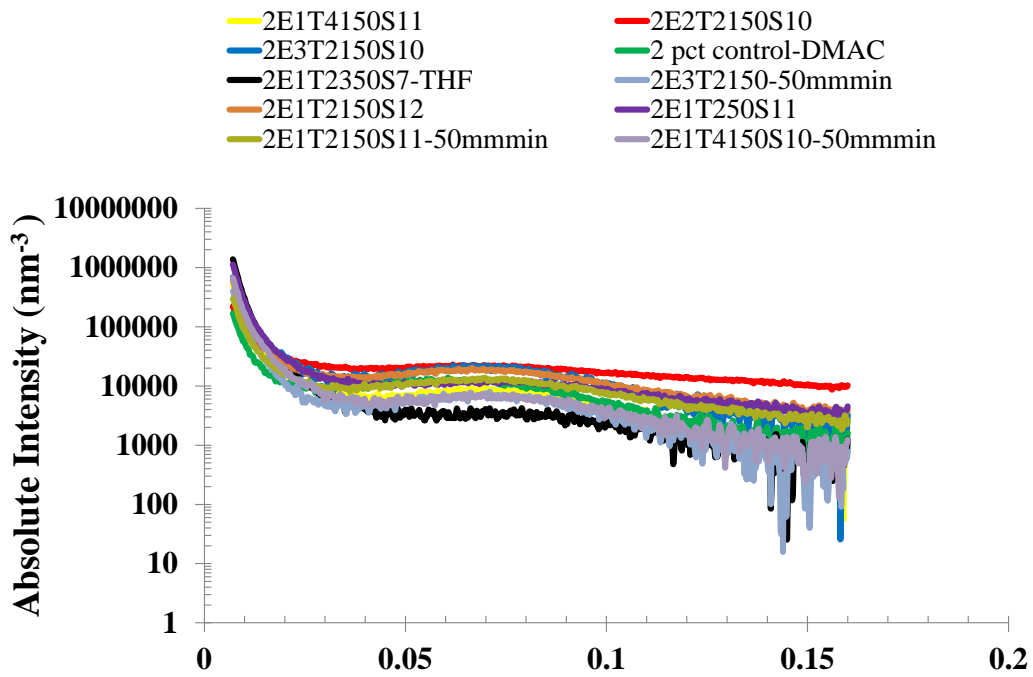


**Figure 53** SAXS intensities for 2% samples plotted as a function of scattering vector.

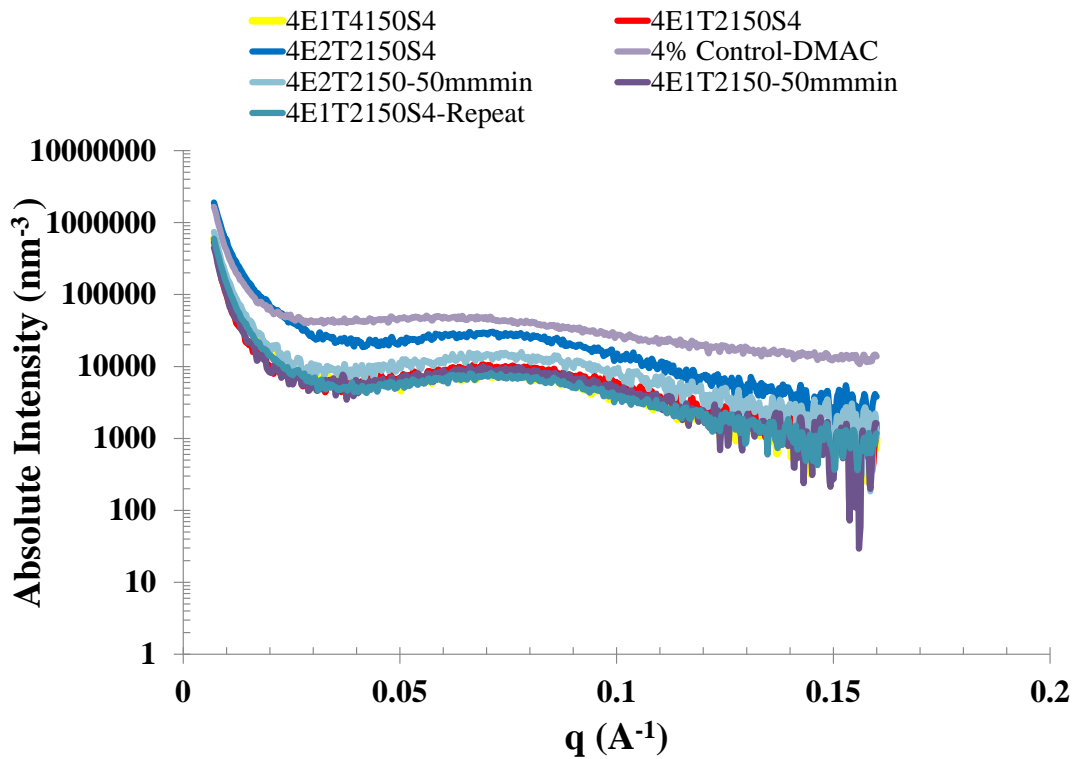


**Figure 54** SAXS intensities for 4% samples plotted as a function of scattering vector.

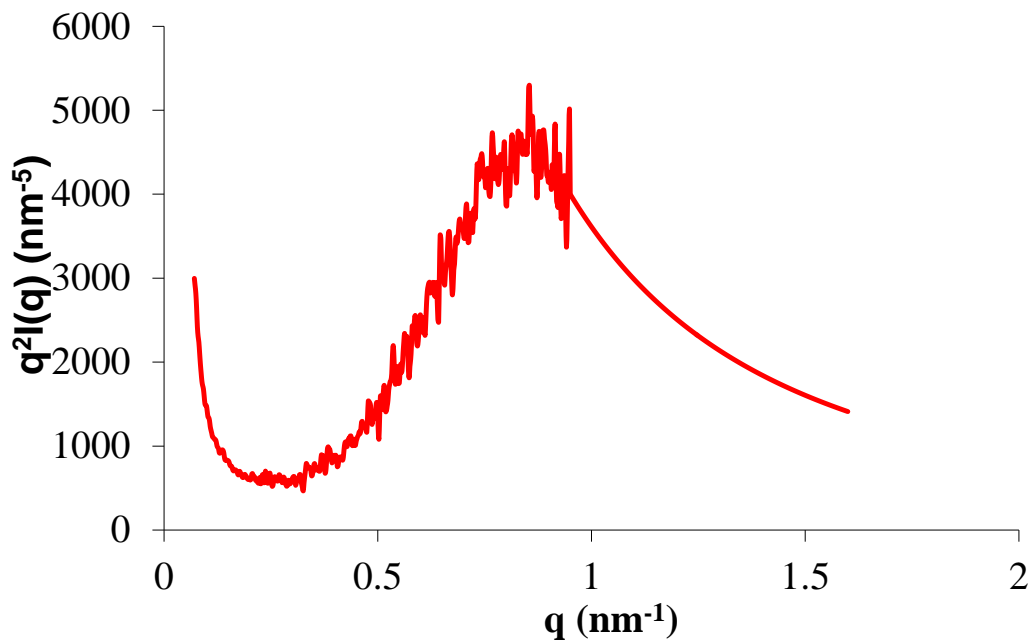


**Figure 55** Example plot of square of scattering vector times intensity as a function of scattering vector used to calculate the invariant.

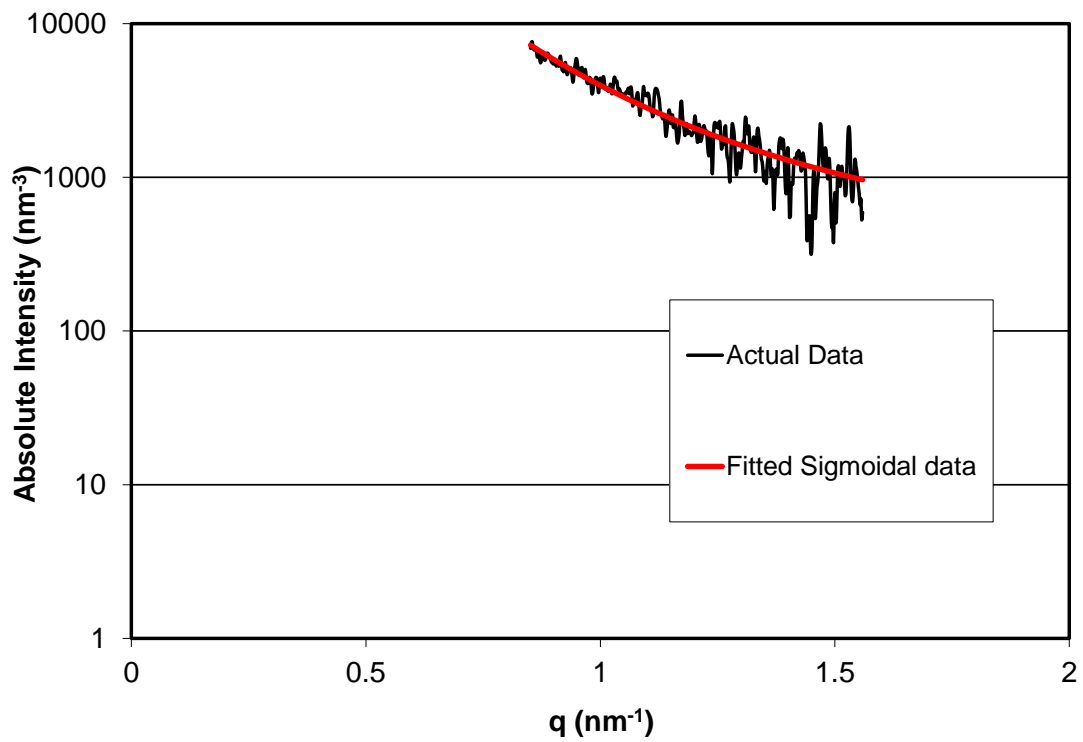


**Figure 56** Example plot of Porod law fit to the latter part of the SAXS profile corresponding to the H to S domain transitional region.

**Table 10: SAXS Datasets for All Samples Fabricated in this Work**

Process Condition	Sample #	Scattering Vector at Peak Intensity (nm <sup>-1</sup> )	Bragg Long Period (nm)	Porod Law Sigmoidal Fit Constants			Invariant ,Q (nm <sup>-6</sup> )
				B	K	s (nm)	
0.2E1T2150S116	1	0.56	11.2	357	4082	-1.37E-03	5129
	2	0.66	9.5	-39	4389	-1.06E-06	5407
0.2E2T2150S120	1	0.72	8.7	-1166	3629	-8.25E-02	3906
	2	0.68	9.2	104	8374	2.37E-02	9672
0.2E3T2150S138	1	0.60	10.4	7607	10457	-1.07E-03	12204
0.2E1T4150S120	1	0.59	10.7	7423	7160	-2.12E-04	8176
0.2E1T2150S116-50mmmin <sup>-1</sup> tested	1	0.70	9	537	5988	1.25E-06	7869
0.2E3T2150S138-50mmmin <sup>-1</sup> tested	1	0.64	9.8	284	5656	2.90E-01	6079
2% Control THF	1	0.65	9.6	197	6462	1.39E-02	6532
2% 90 min US THF	1	0.62	10.1	5624	18103	-1.78E-05	16419
2% Control DMAC	1	0.61	10.4	334	4644	0	4802
2E1T2350S7 THF	1	0.79	8	420	17176	0	2138
MA THF	1	0.64	9.8	153	1435	-1.29E-04	1596
MA-5mN/min tested THF	1	0.64	9.8	87	1762	-2.30E-03	2002
2E1T250S11	1	0.67	9.4	3362	4626	-1.44E-06	4664
2E1T2150S12	1	0.67	9.4	3106	7201	8.15E-06	7048
2E2T2150S10	1	0.62	10.2	10260	5923	3.30E-06	5568
2E3T2150S10	1	0.64	9.8	819	8825	-3.60E-06	8723
2E1T4150S11	1	0.70	9	236	3856	-1.70E-03	5823
2E1T2150S12-50mmmin <sup>-1</sup> tested	1	0.70	9	2090	5129	4.51E-05	16418
2E1T4150S12-50mmmin <sup>-1</sup> tested	1	0.71	8.9	-100	3170	-2.50E-03	3179
2E3T2150S12-50mmmin <sup>-1</sup> tested	1	0.70	9	225	3346	-1.76E-03	3361
4% Control DMAC	1	0.64	9.8	116484	14605	-3.62E-06	15206
4E1T250S4	1	0.72	8.7	4088	6546	1.09E-05	6190
4E1T2150S4	1	0.69	9.1	264	4803	3.02E-06	4502
	2	0.71	8.9	306	3425	-2.60E-02	3403
4E2T2150S4	1	0.72	8.8	907	2271..376	-1.18E-04	13039
4E1T4150S4	1	0.65	9.7	353	3611	-1.55E-03	3608
4E1T2150S4-50mmmin <sup>-1</sup> tested	1	0.69	9.1	14	4491	-8.70E-04	4231
4E2T2150S4-50mmmin <sup>-1</sup> tested	1	0.78	8.1	632	7082	-1.20E-06	6570

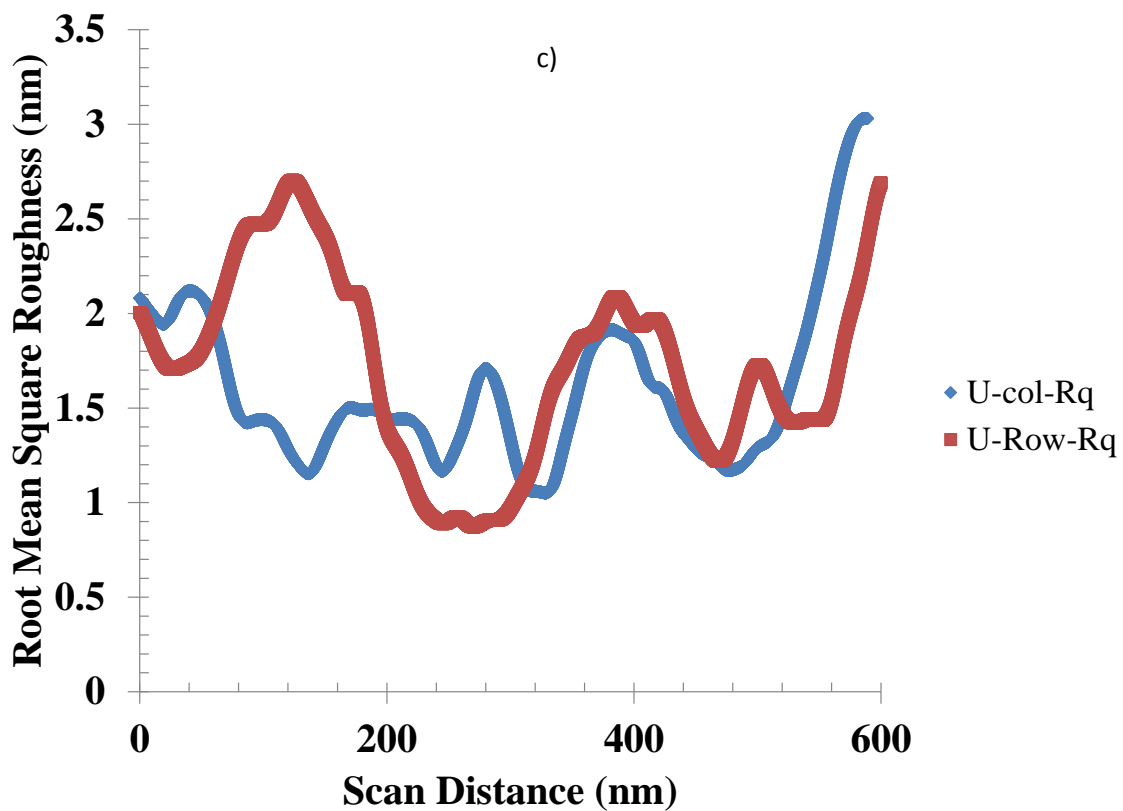
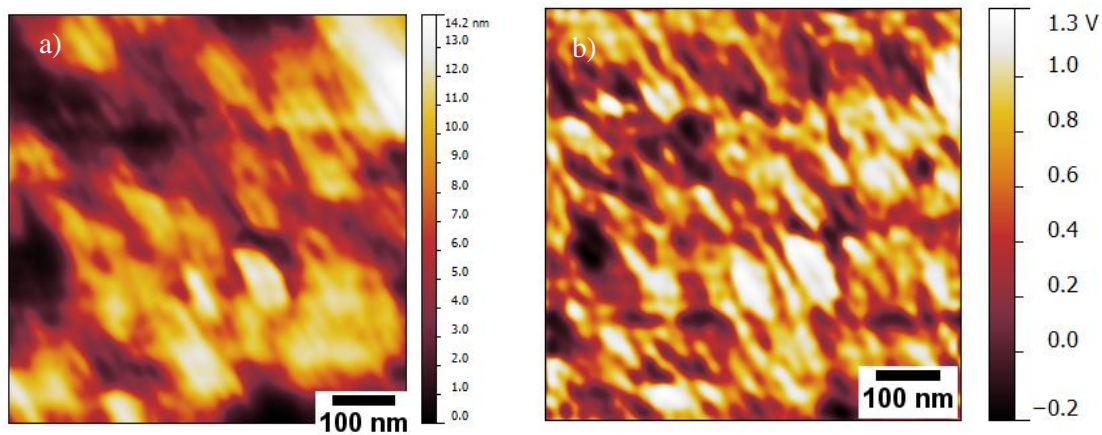


**Figure 57** a) Topographic and b) Phase images and c) RMS roughness's for unsonicated THF based cast TPU film.

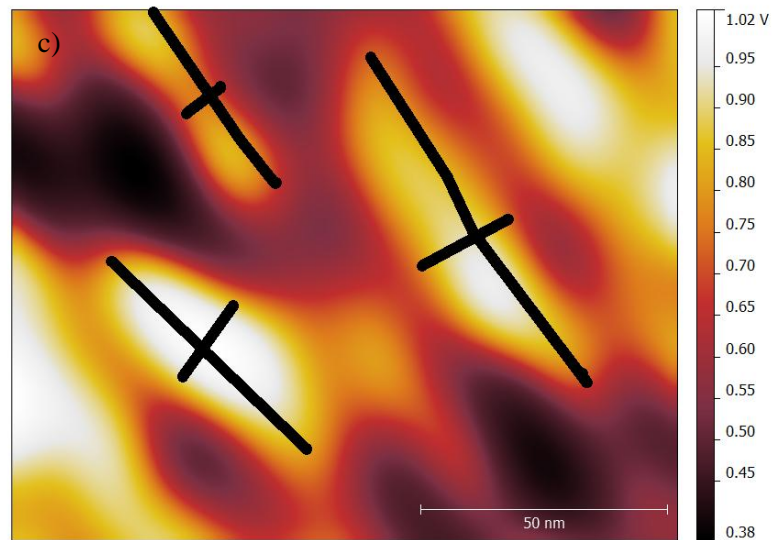
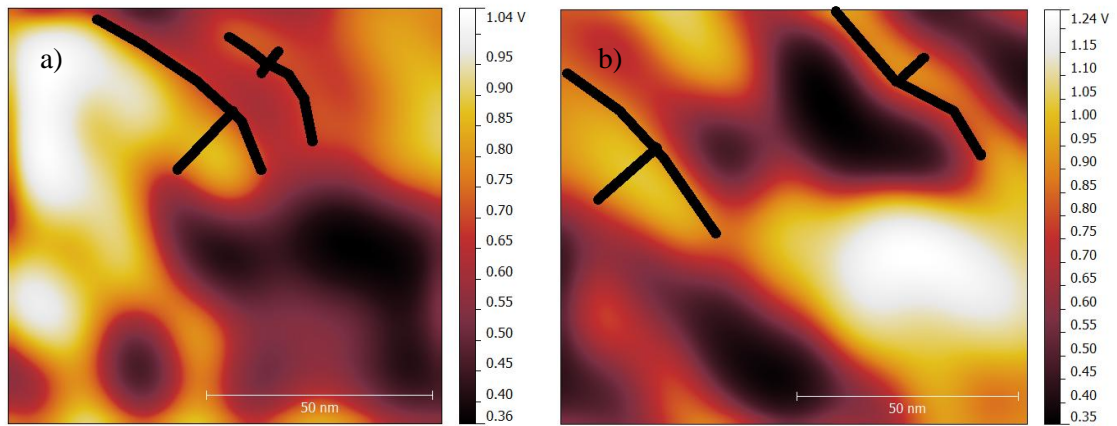


**Figure 58** a), b), c) are three sample images of selected regions within the phase image in Figure 57 b).



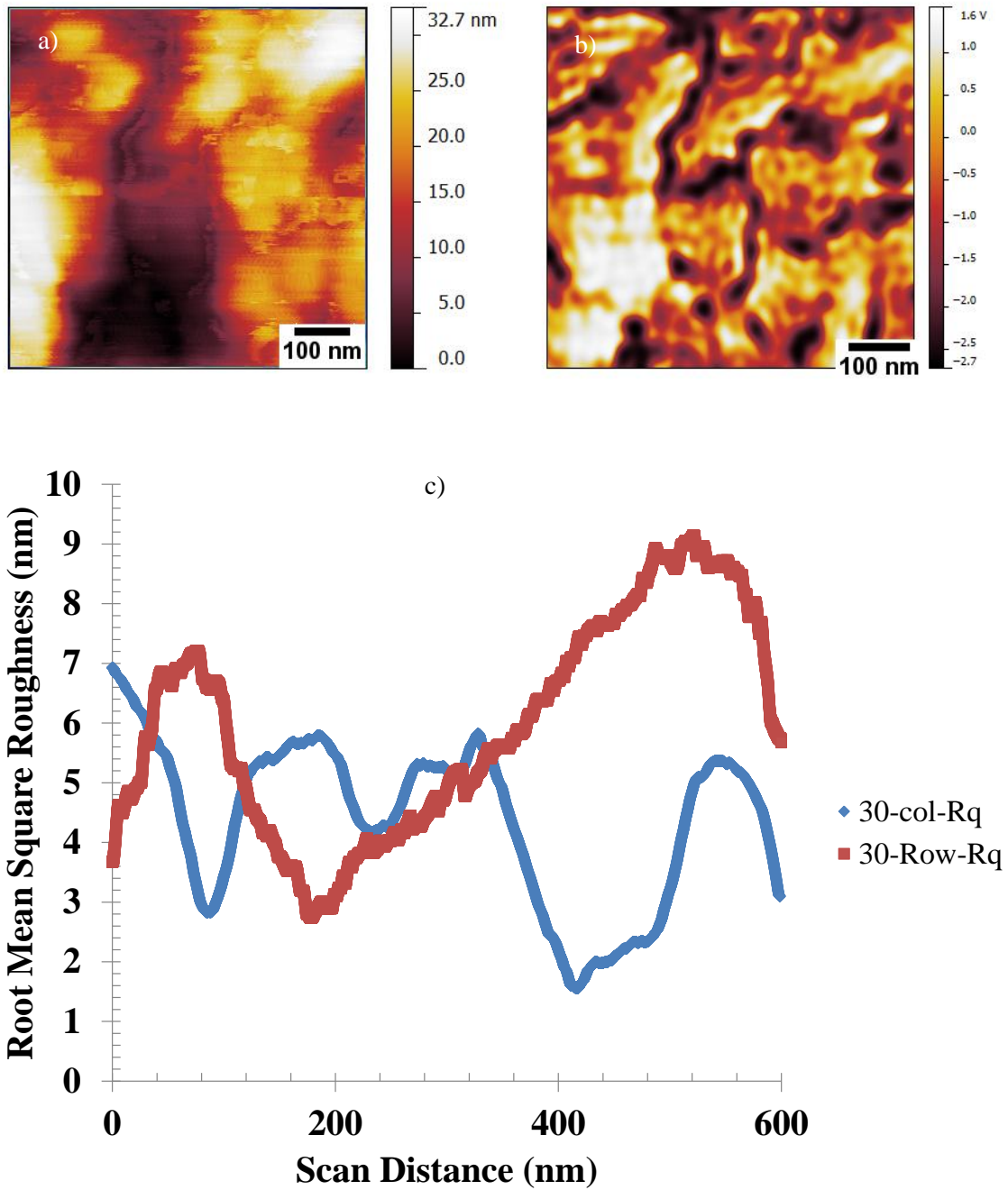


**Figure 59** a) Topographic and b) Phase images and c) RMS roughness's for 30 minute sonicated THF based cast TPU film.

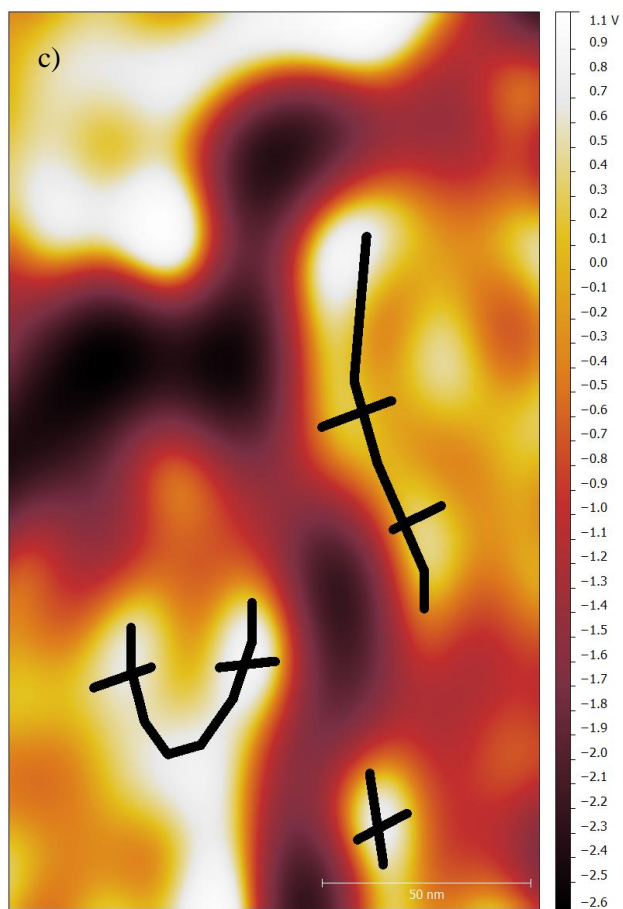
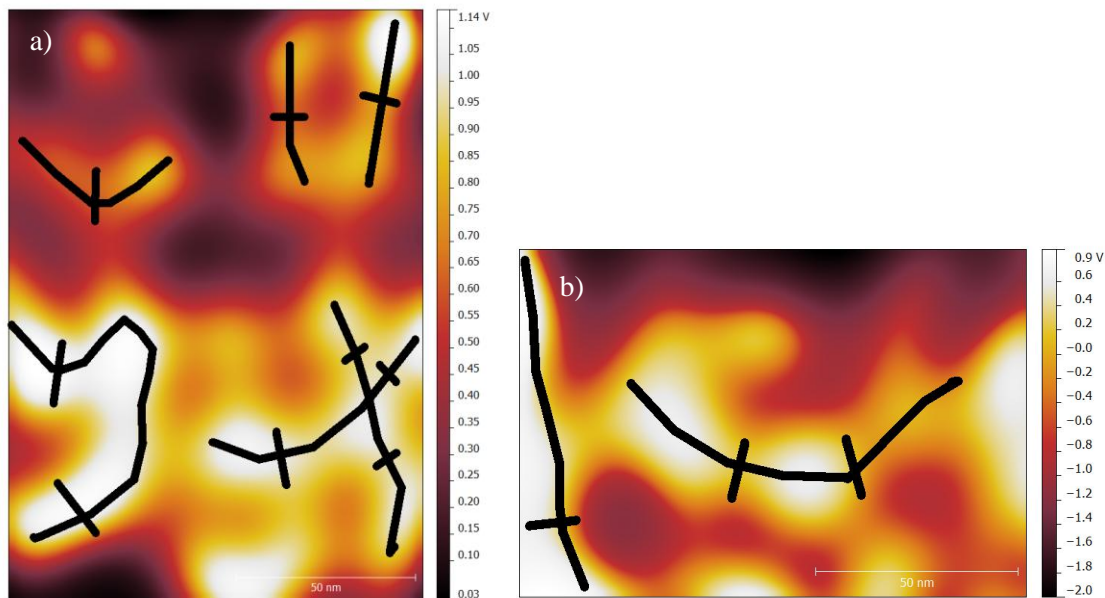


**Figure 60** a), b), c) are three sample images of selected regions within the phase image in Figure 59 b).

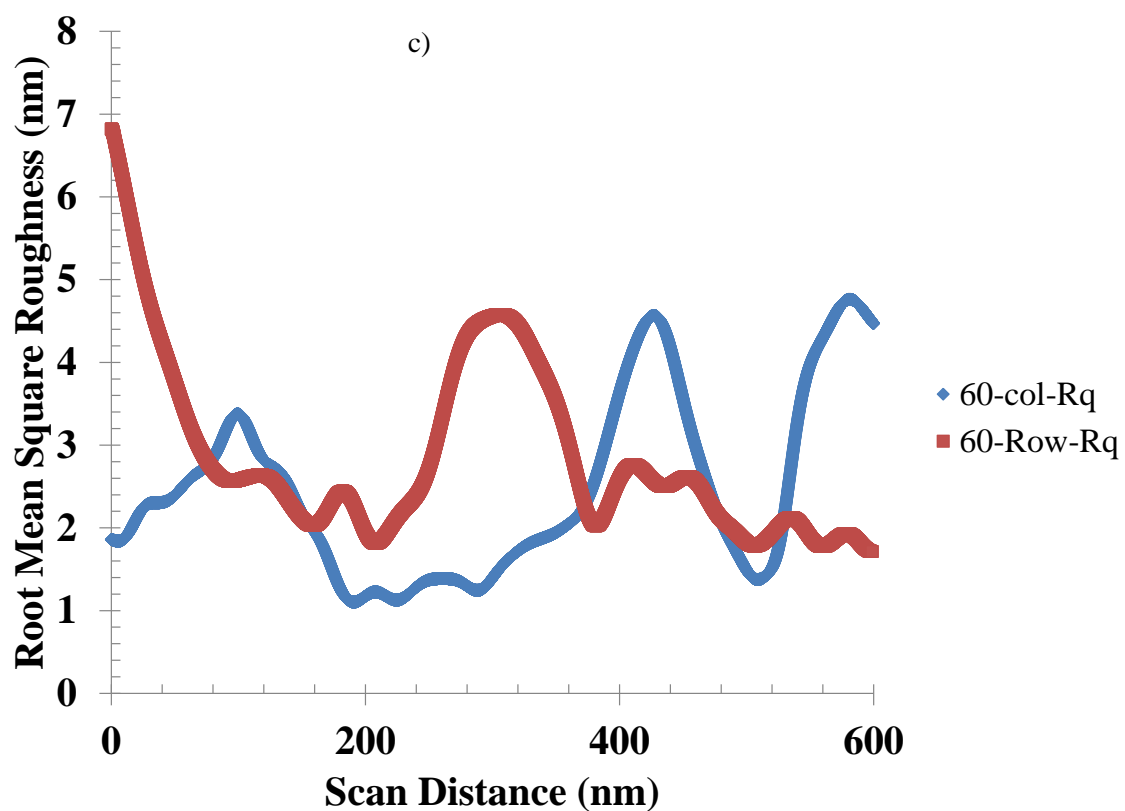
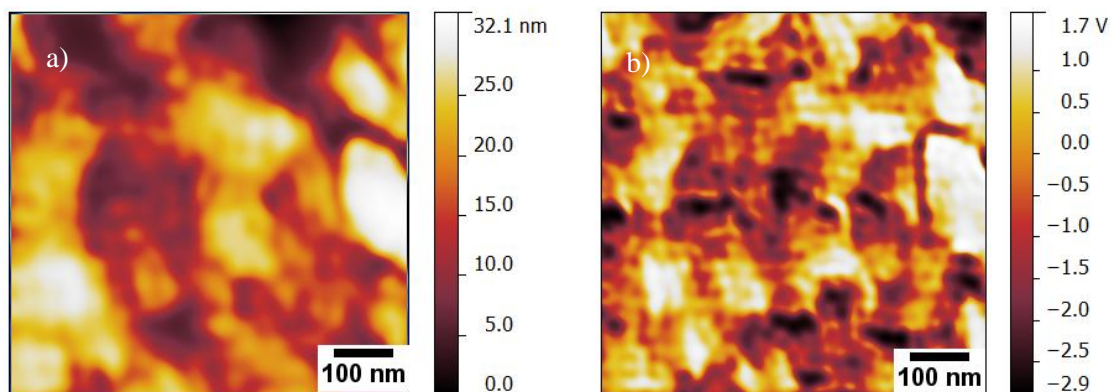


**Figure 61** a) Topographic and b) Phase images and c) RMS roughness's for 60 minute sonicated THF based cast TPU film.

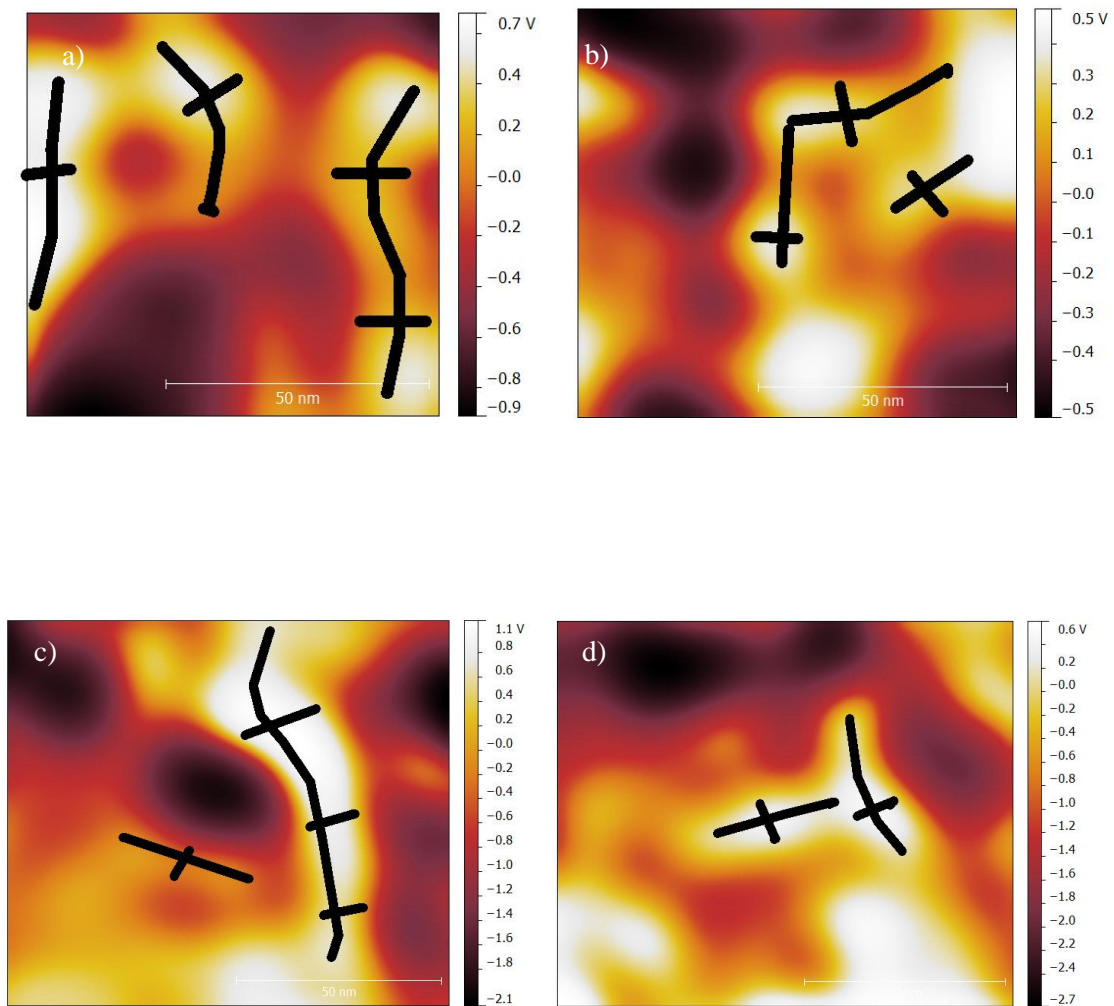


**Figure 62** a), b), c), d) are three sample images of selected regions within the phase image in Figure 61 b).

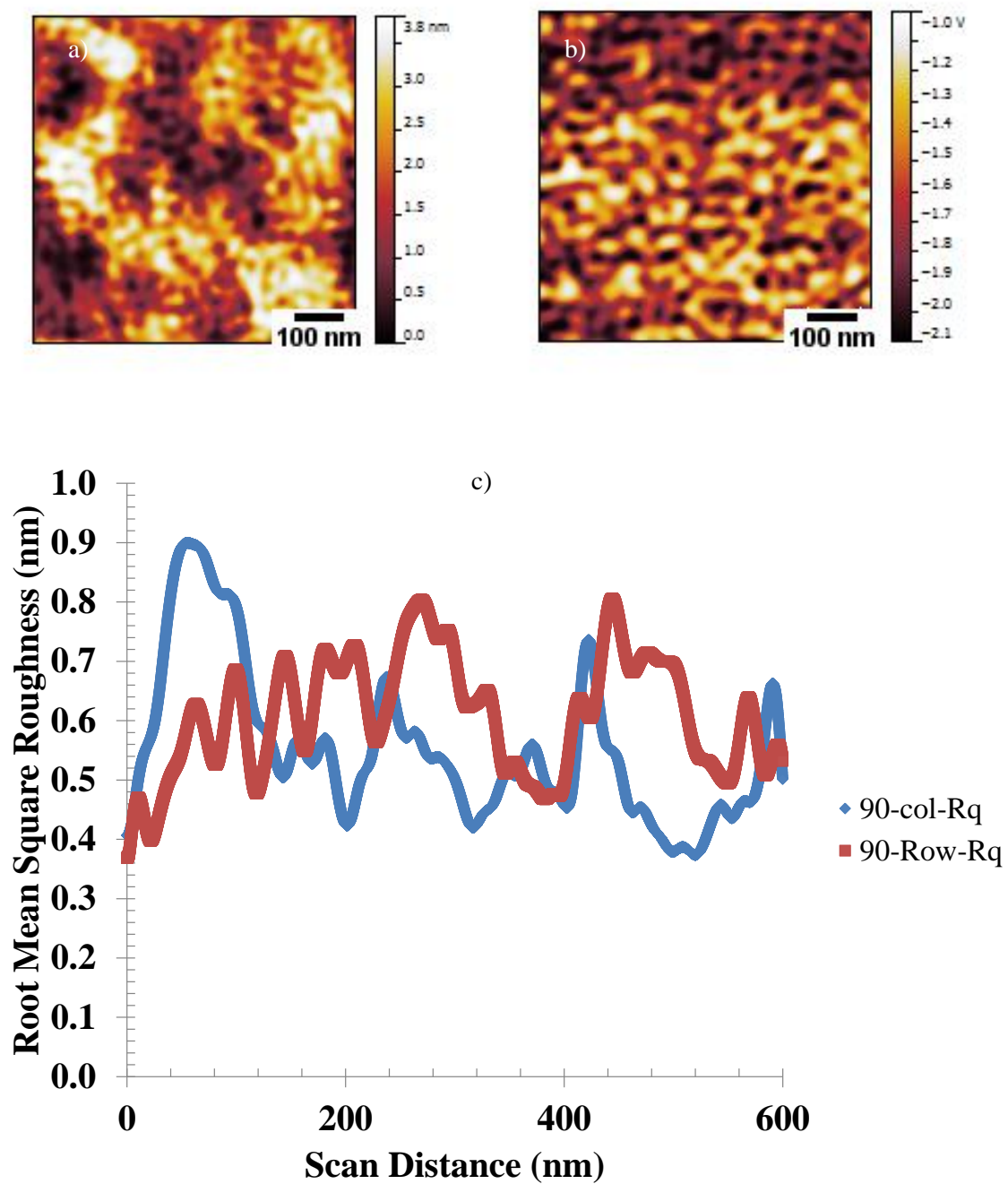


**Figure 63** a) Topographic and b) Phase images and c) RMS roughness's for 90 minute sonicated THF based cast TPU film

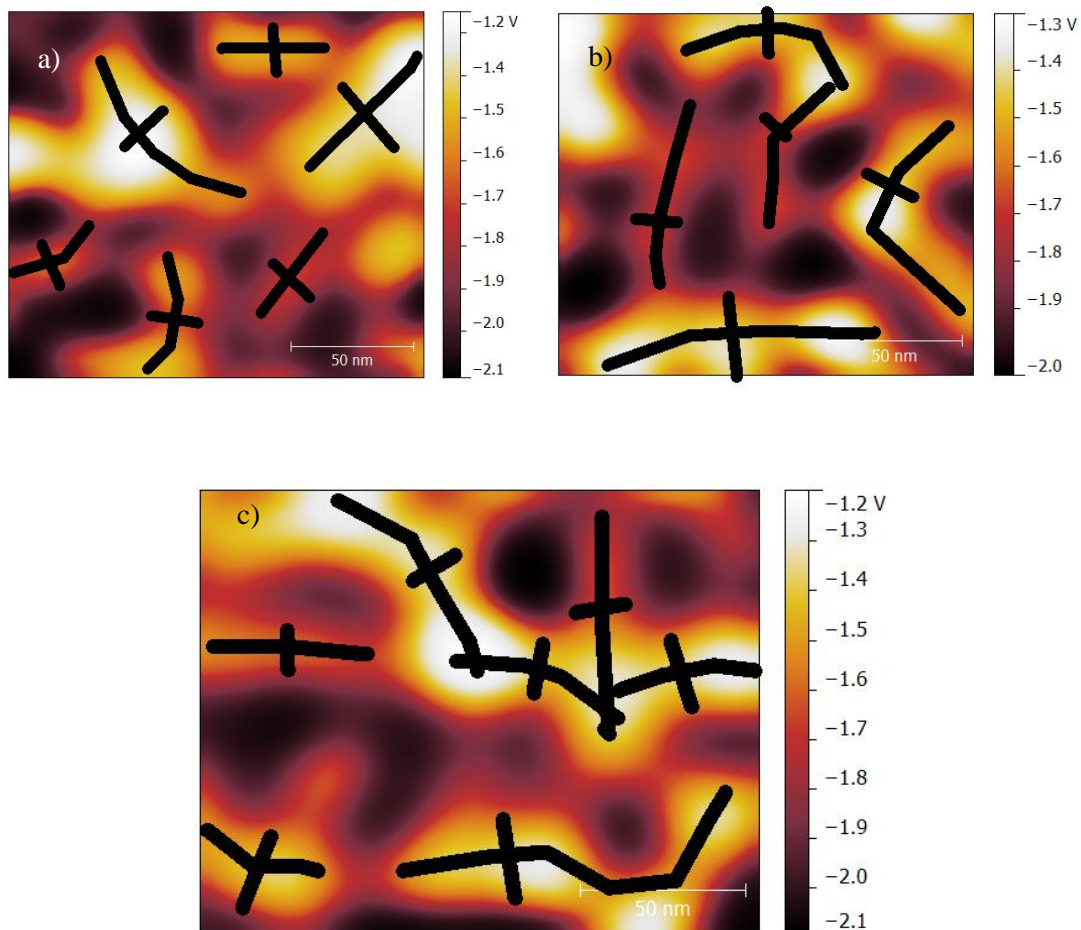


**Figure 64** a), b), c) are three sample images of selected regions within the phase image in Figure 63 b

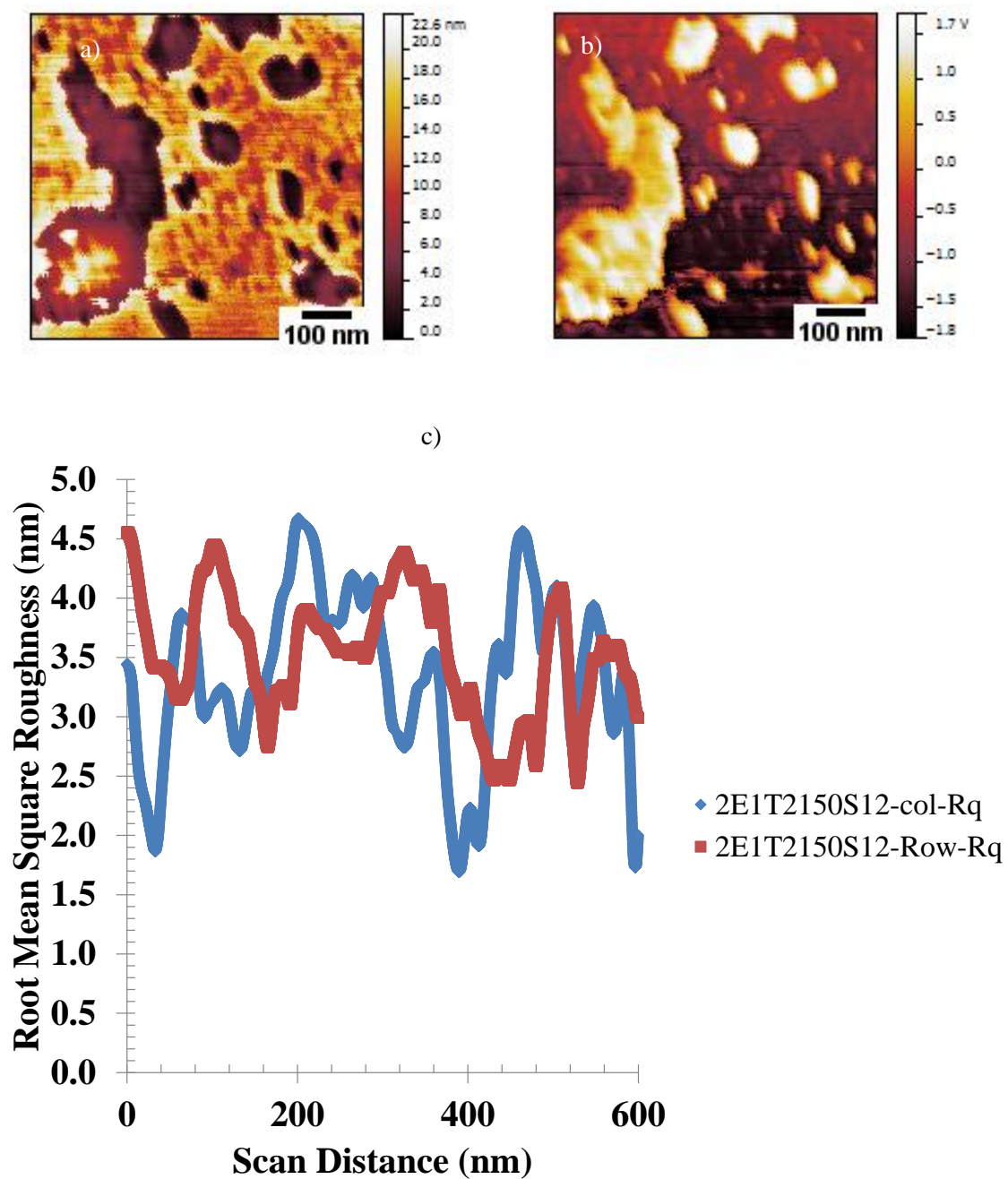


**Figure 65** a) Topographic and b) Phase images and c) RMS roughness's for a 2E1T2150S12 atomized DMAC based film

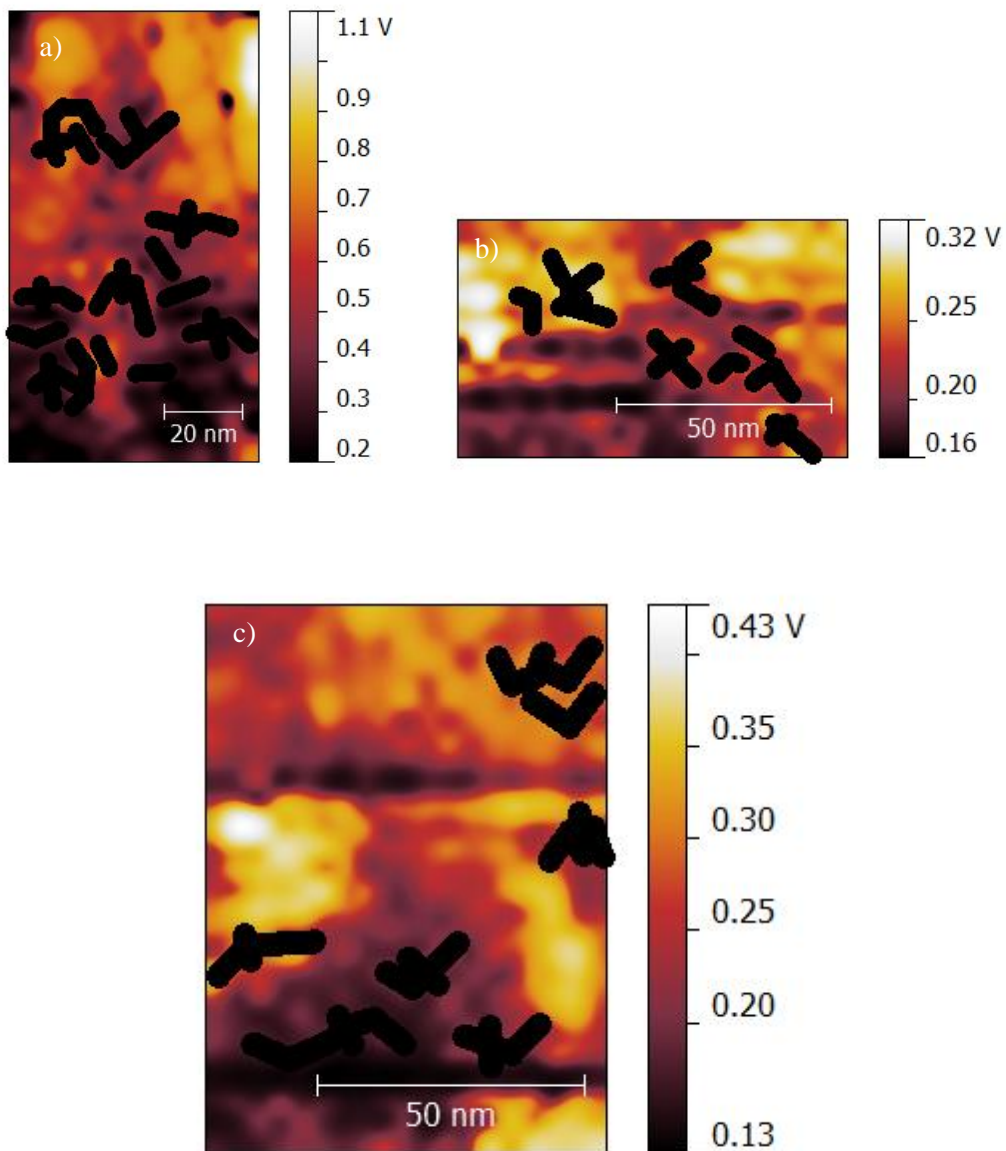


**Figure 66** a), b), c) are three sample images of selected regions within the phase image in Figure 65 b



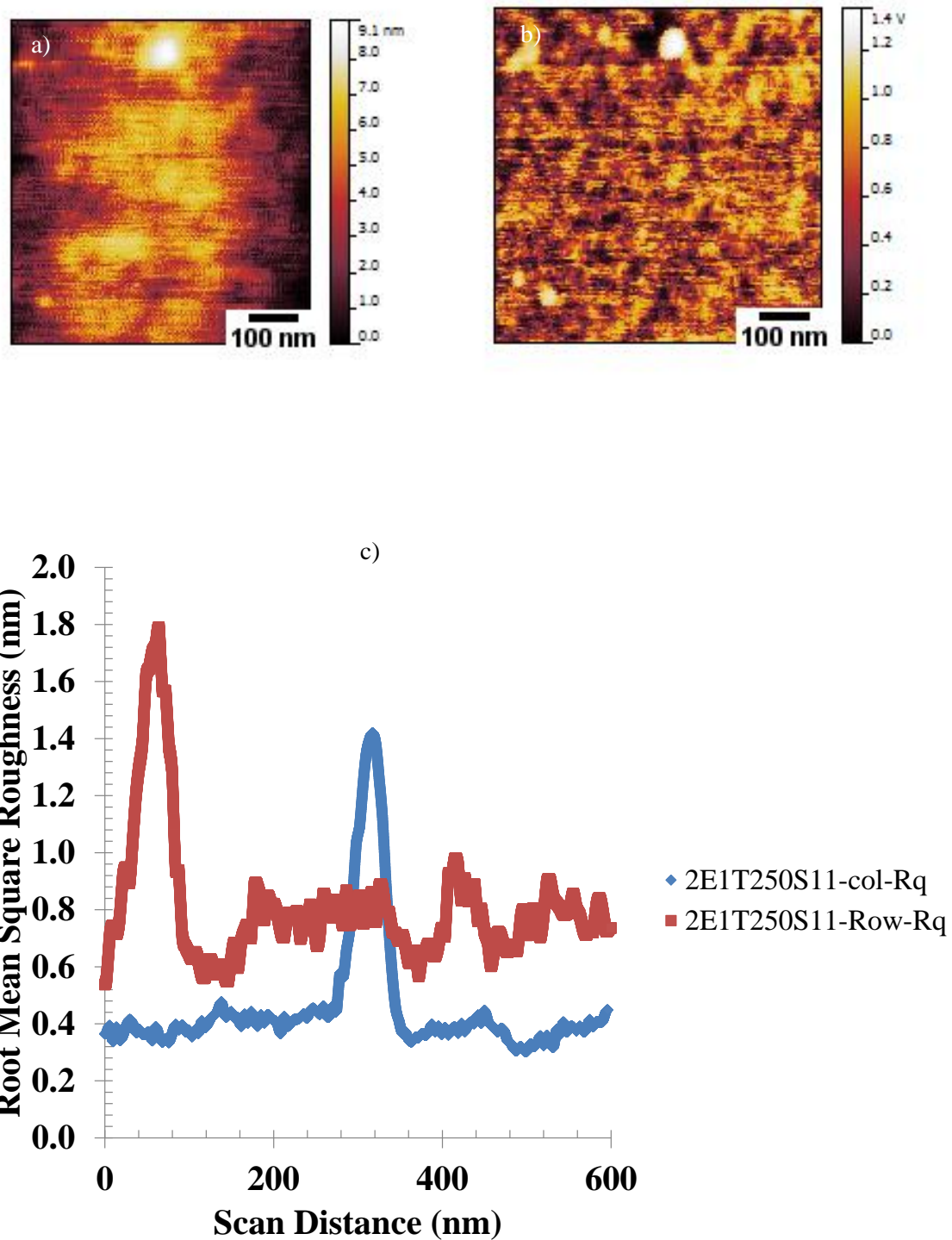


**Figure 67** a) Topographic and b) Phase images and c) RMS roughness's for a 2E1T250S11 atomized DMAC based film

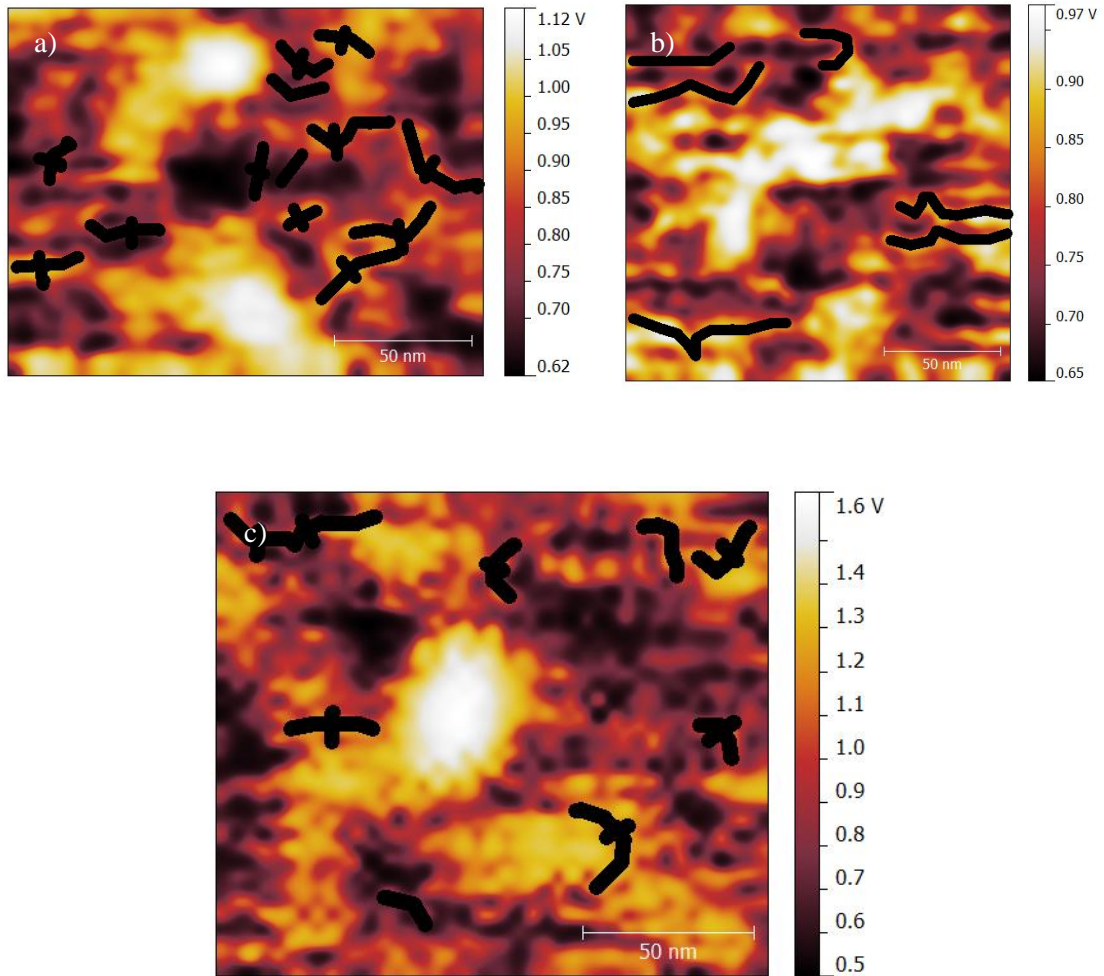


**Figure 68** a), b), c) are three sample images of selected regions within the phase image in Figure 67 b

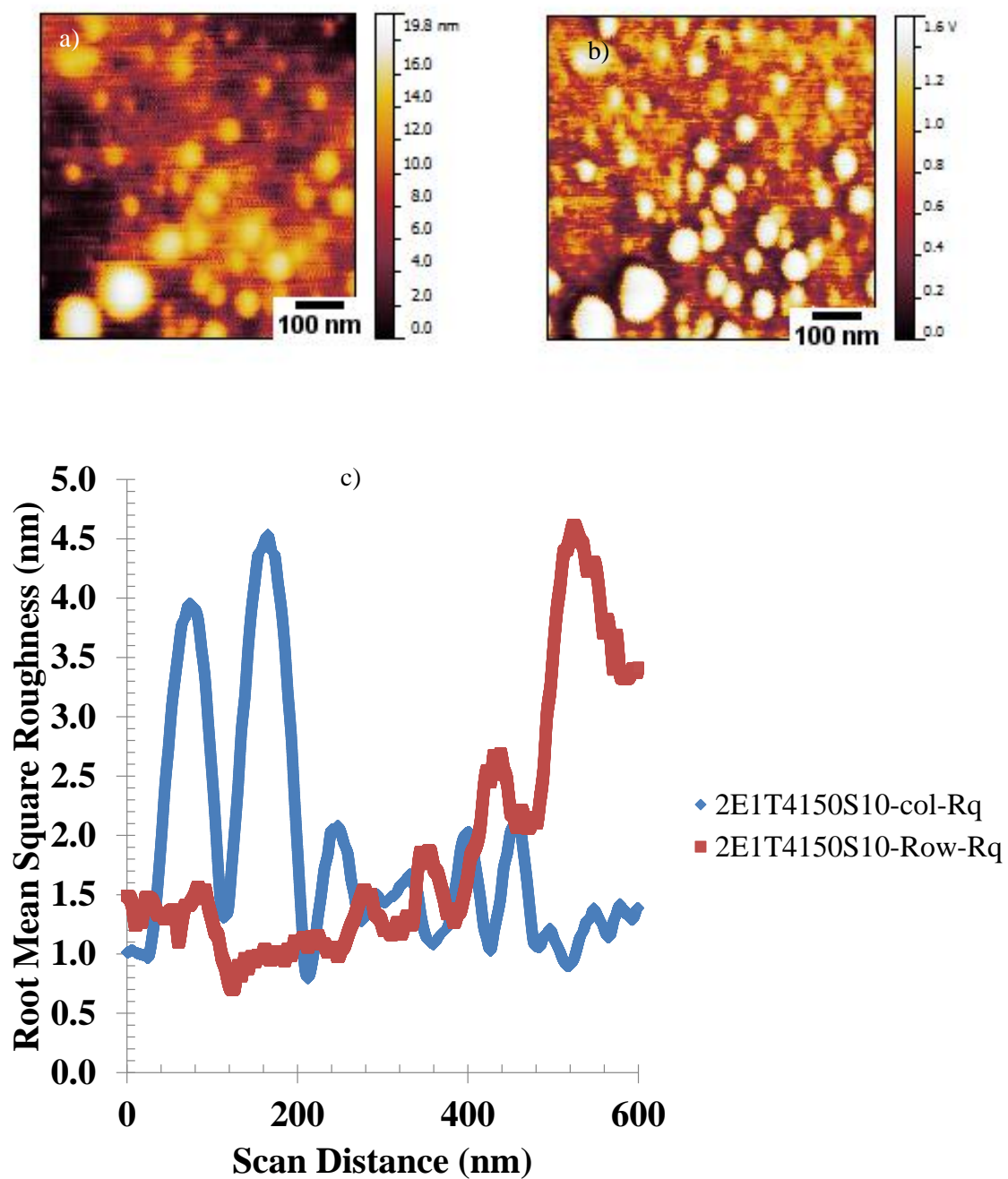


**Figure 69** a) Topographic and b) Phase images and c) RMS roughness's for a 2E1T4150S10 atomized DMAC based film

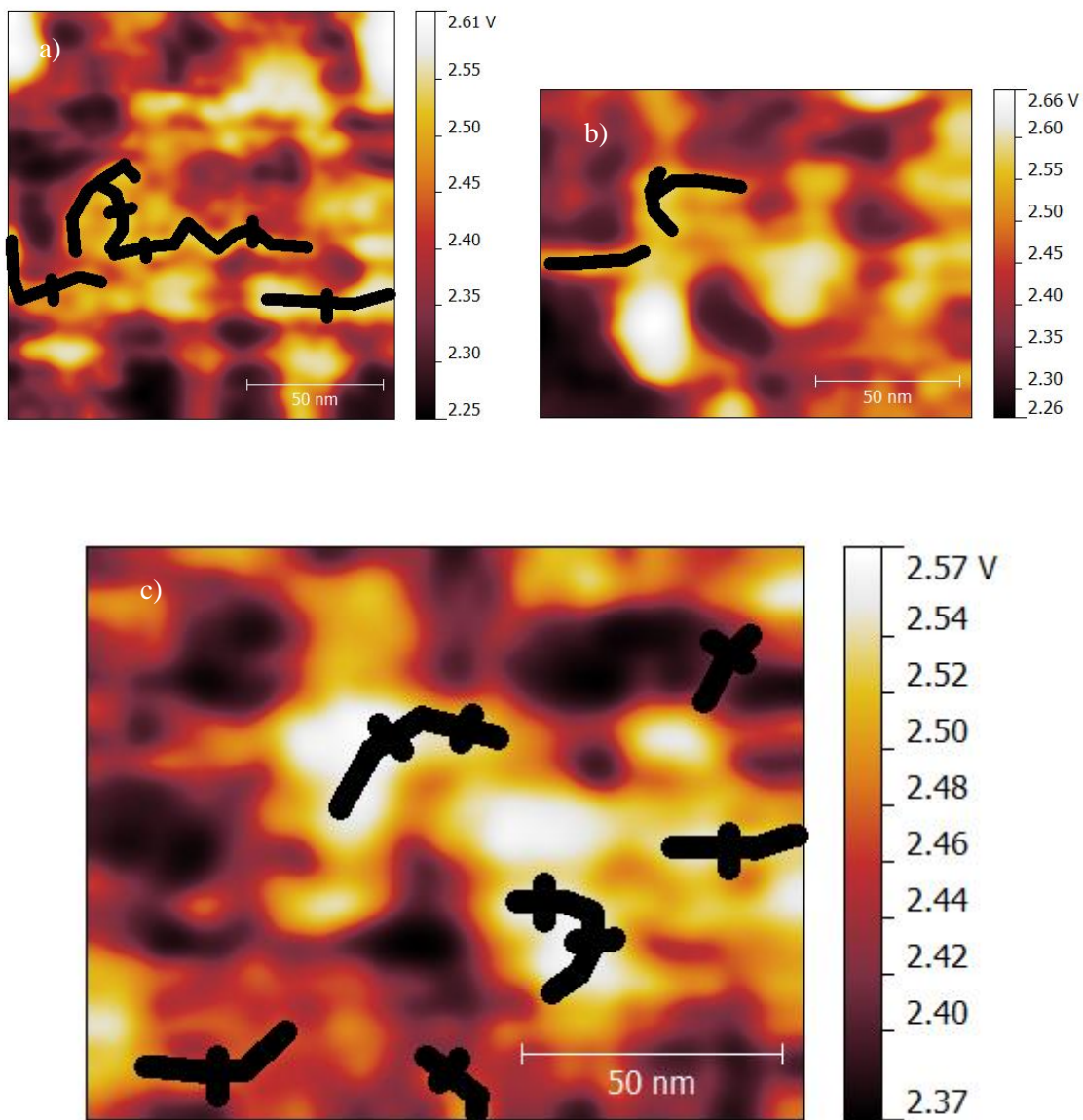


**Figure 70** a), b), c) are three sample images of selected regions within the phase image in Figure 69 b

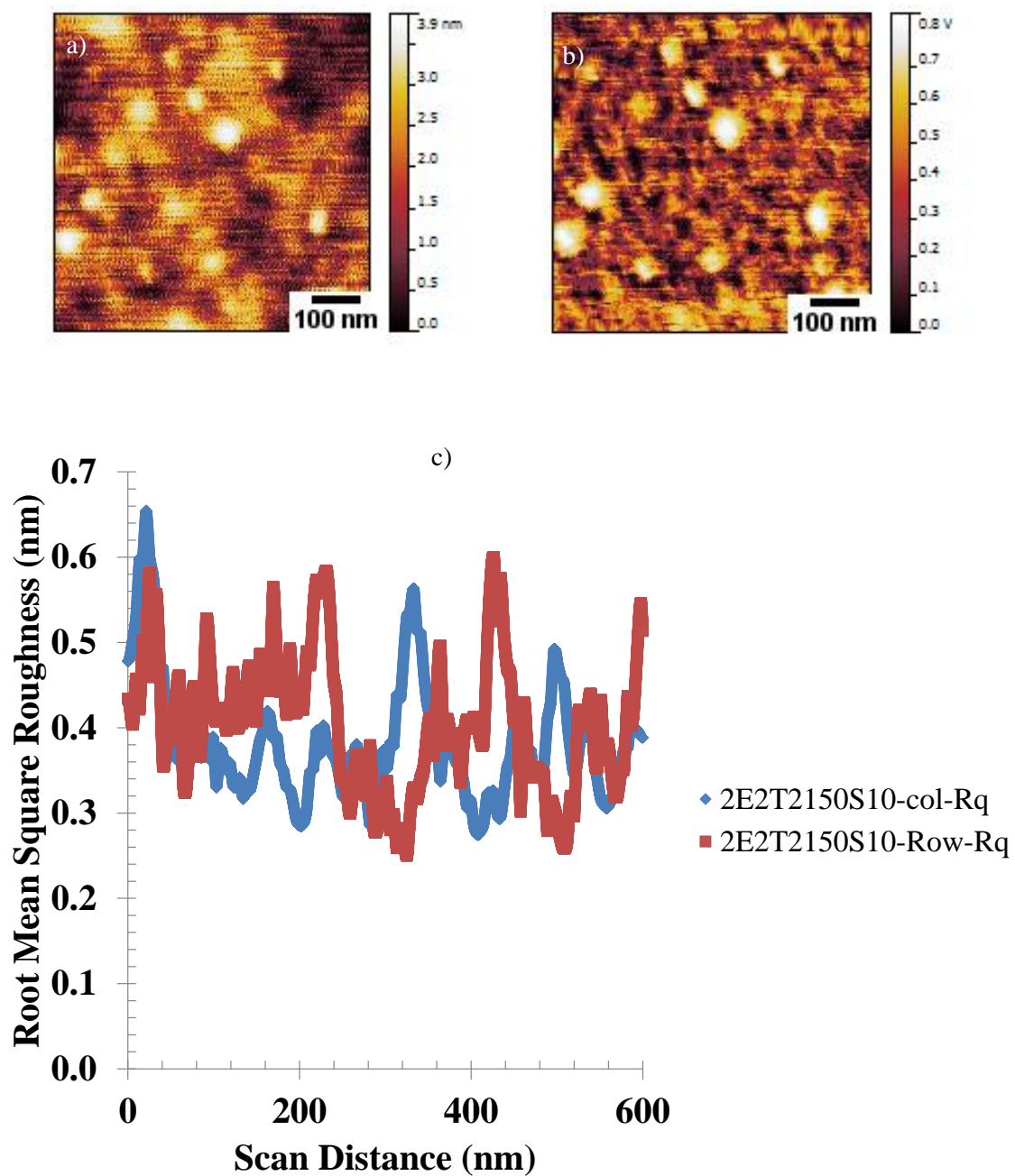


**Figure 71** a) Topographic and b) Phase images and c) RMS roughness's for a 2E2T2150S10 atomized DMAC based film

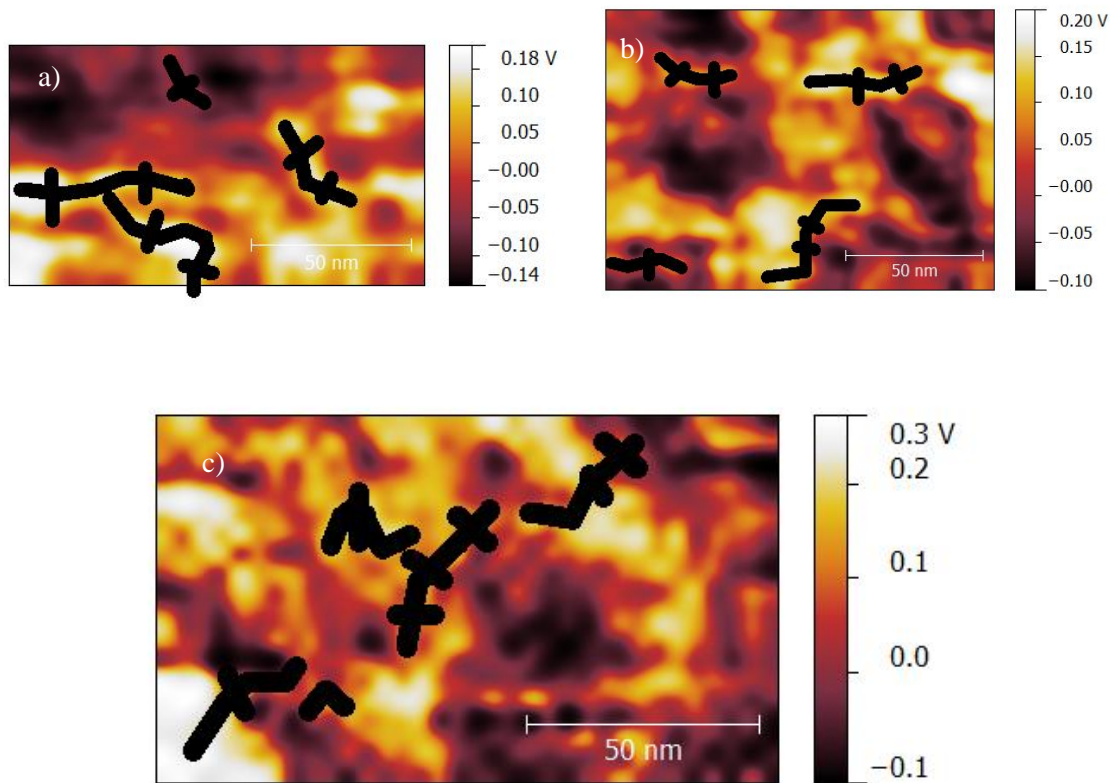


**Figure 72** a), b), c) are three sample images of selected regions within the phase image in Figure 71 b

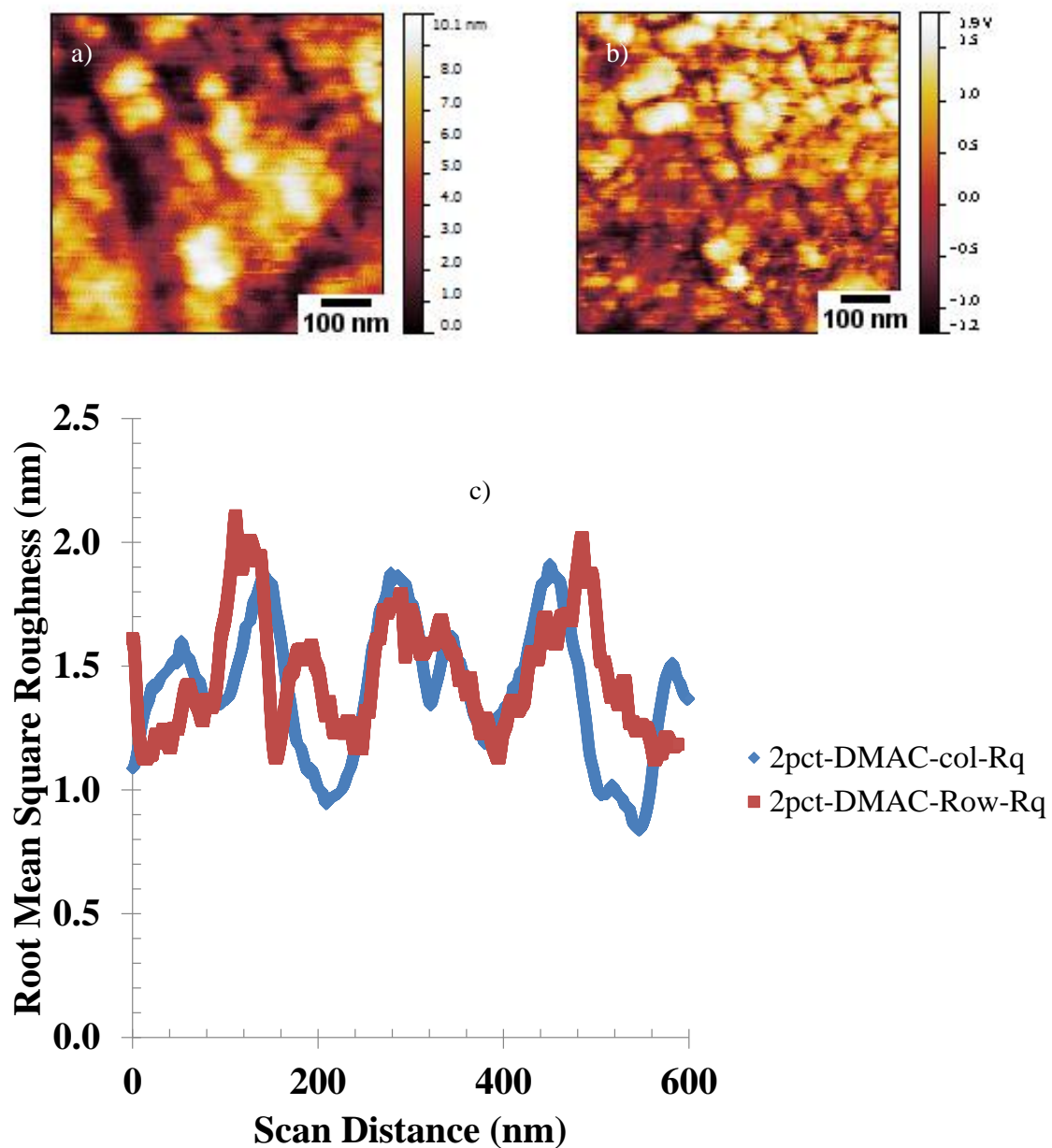


**Figure 73** a) Topographic and b) Phase images and c) RMS roughness's for a 2pct control cast DMAC film

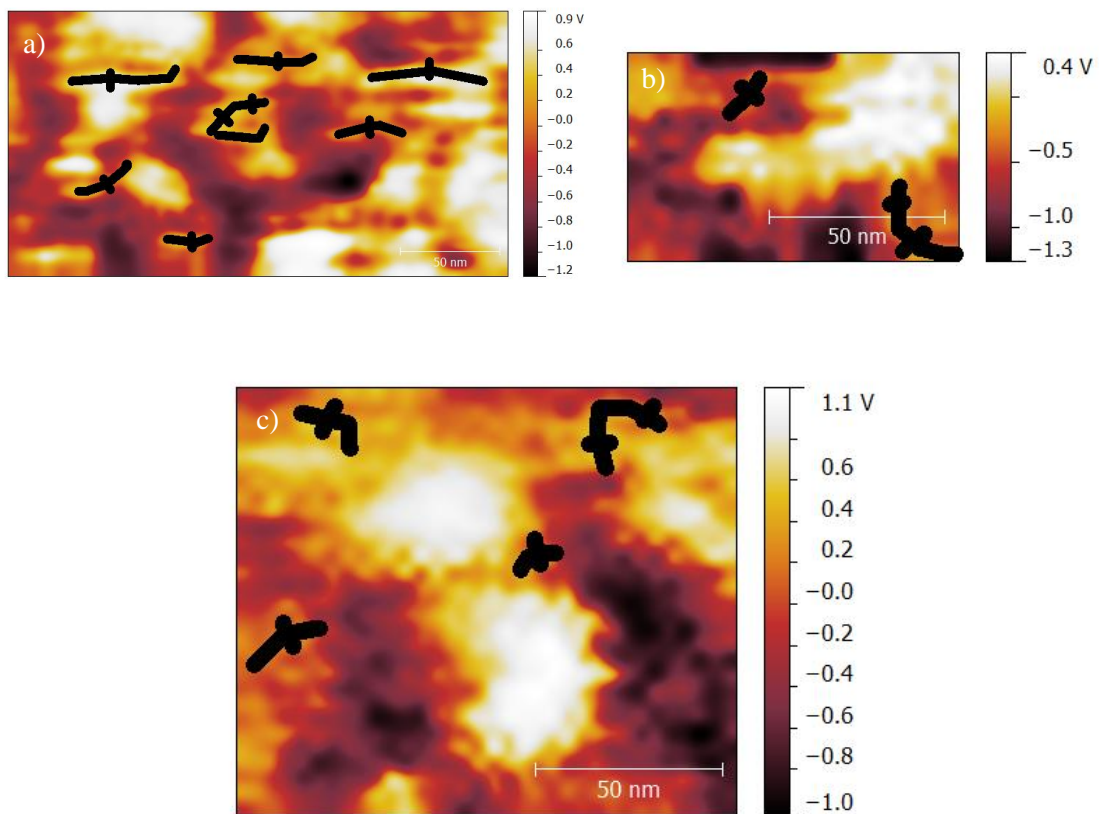


**Figure 74** a), b), c) are three sample images of selected regions within the phase image in Figure 73 b



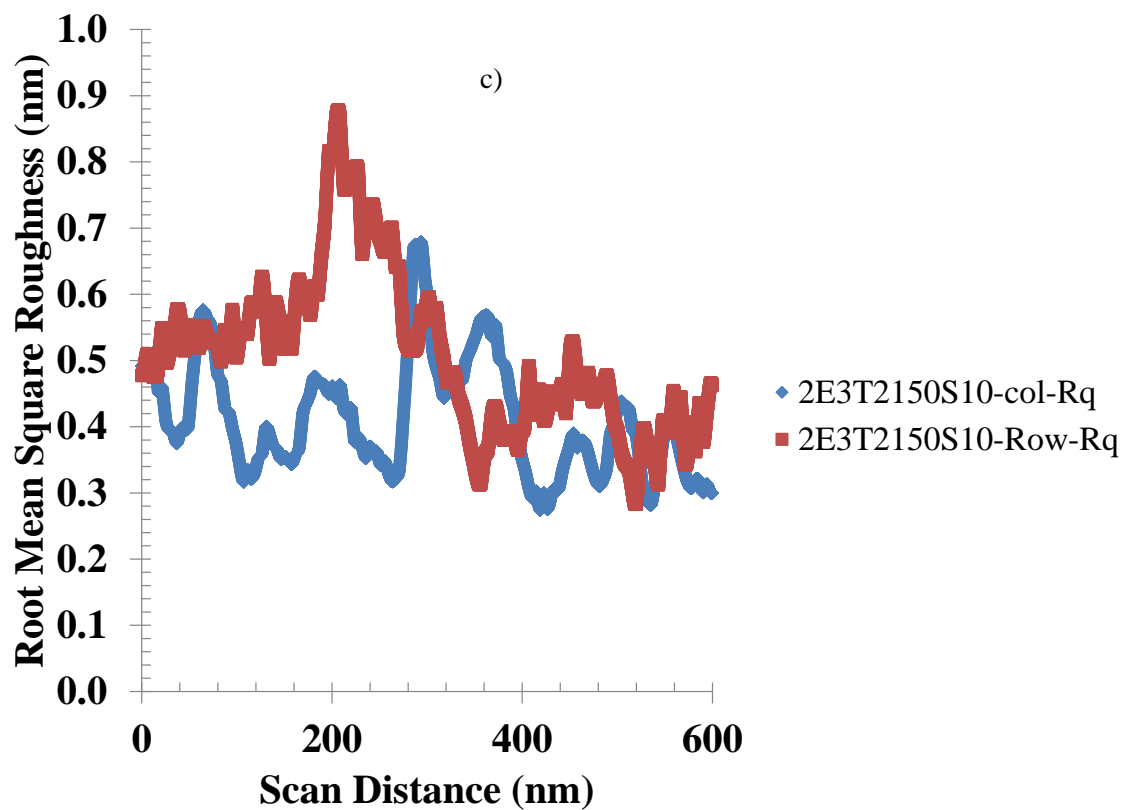
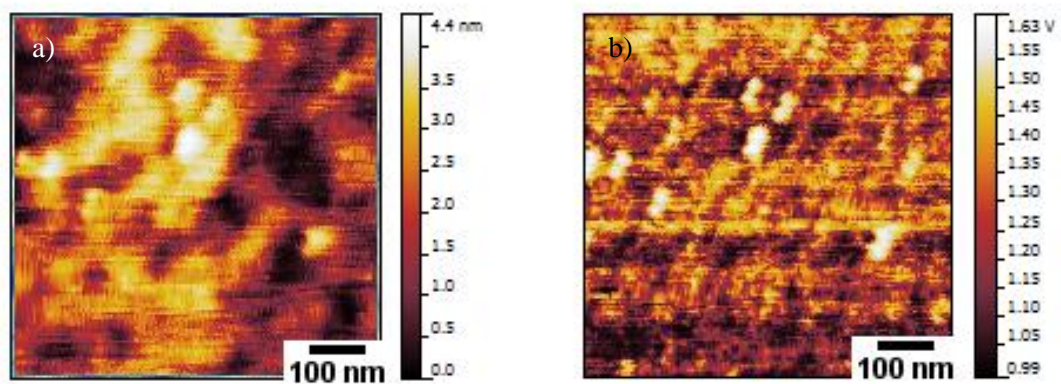


**Figure 75** a) Topographic and b) Phase images and c) RMS roughness's for a 2E3T2150S10 atomized DMAC film

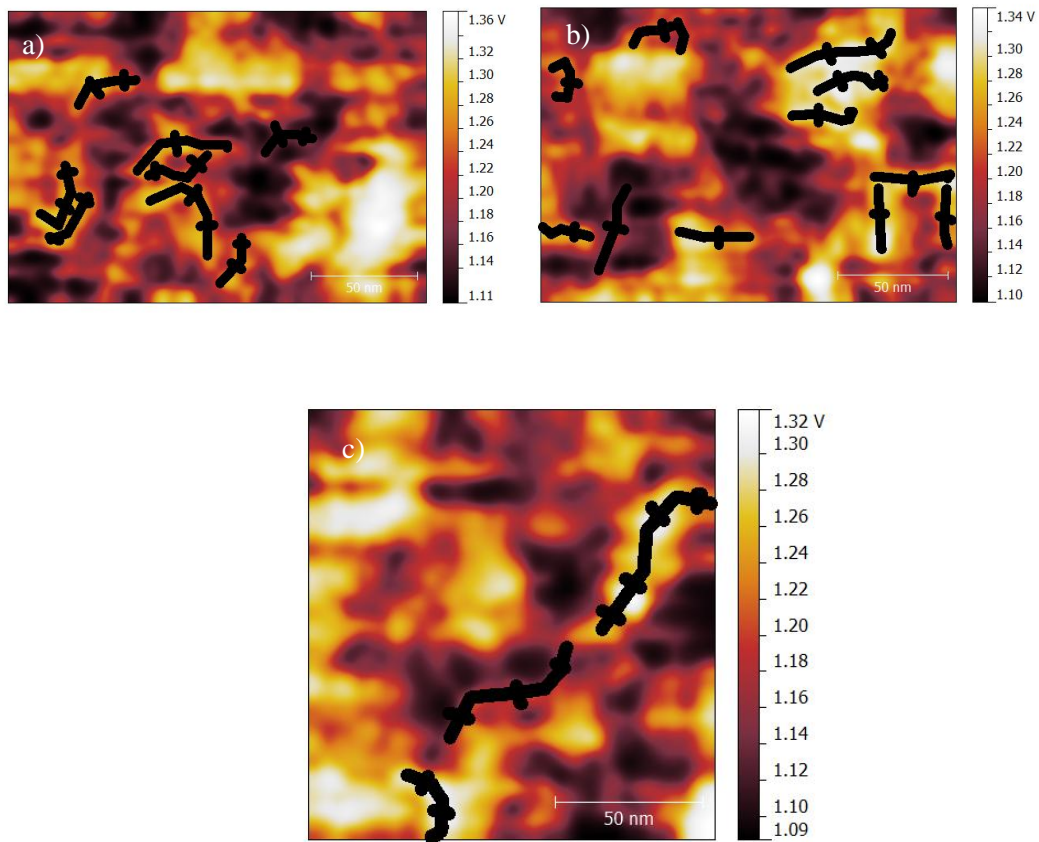


**Figure 76** a), b), c) are three sample images of selected regions within the phase image in Figure 75b

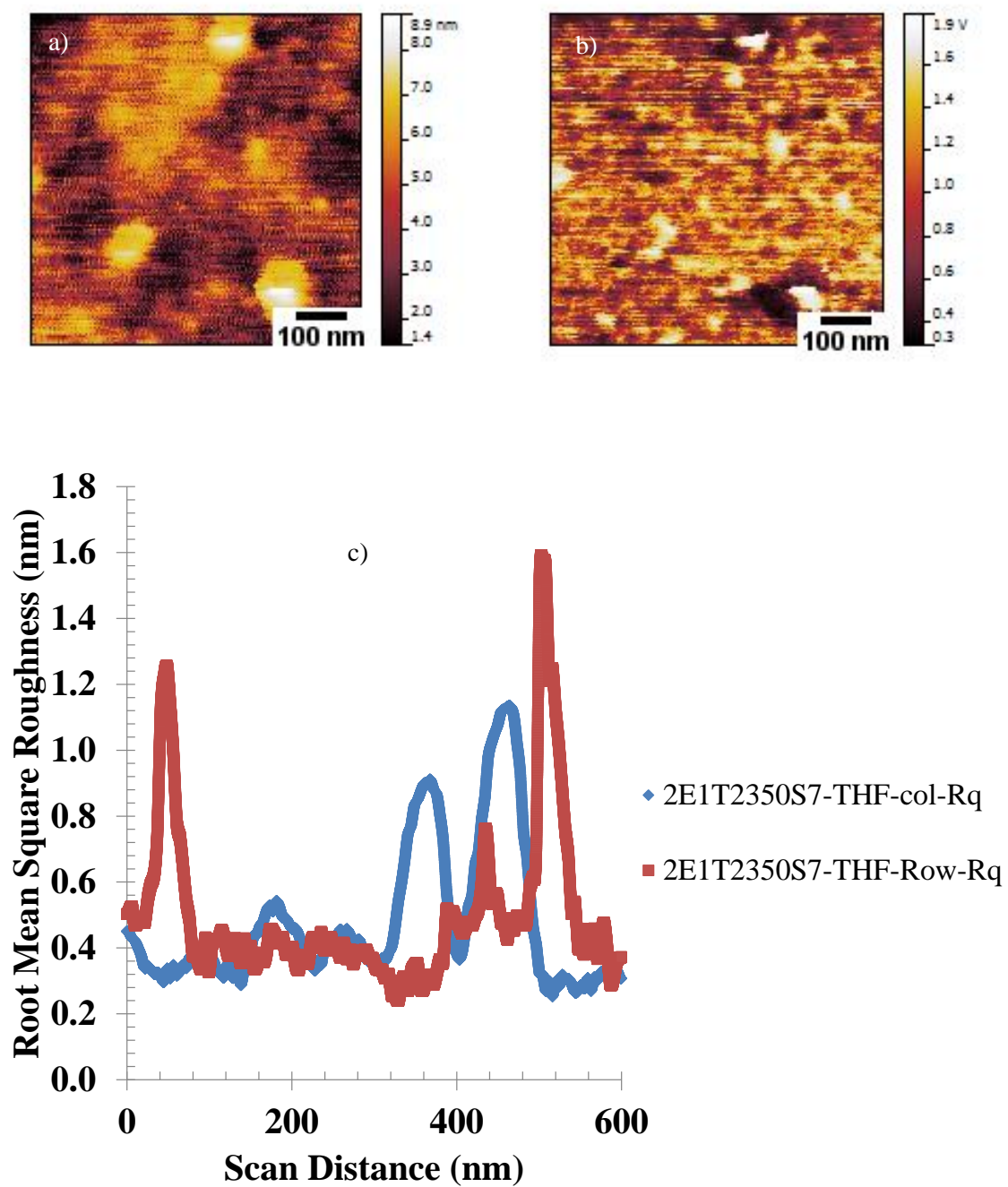


**Figure 77** a) Topographic and b) Phase images and c) RMS roughness's for a 2E1T2350S7 atomized THF film

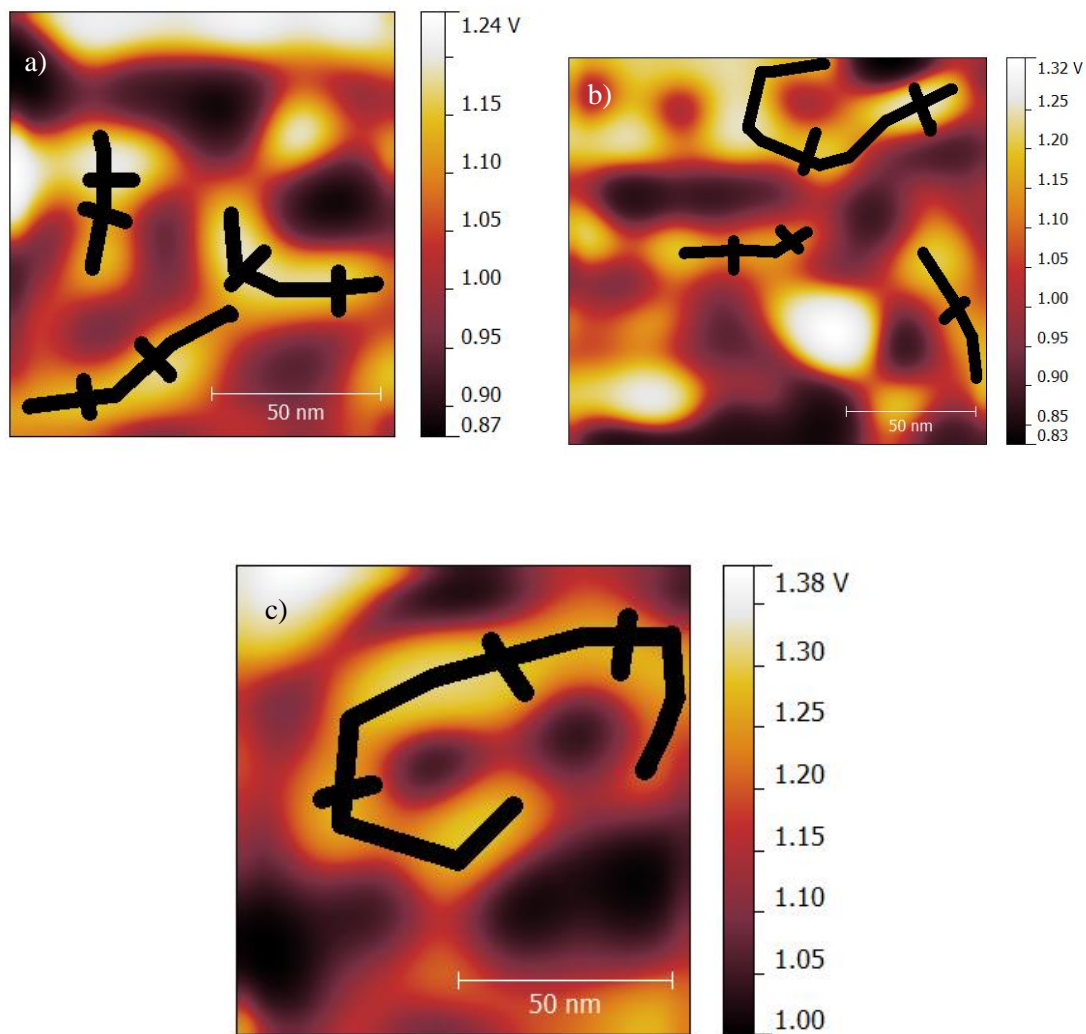


**Figure 78** a), b), c) are three sample images of selected regions within the phase image in Figure 77 b

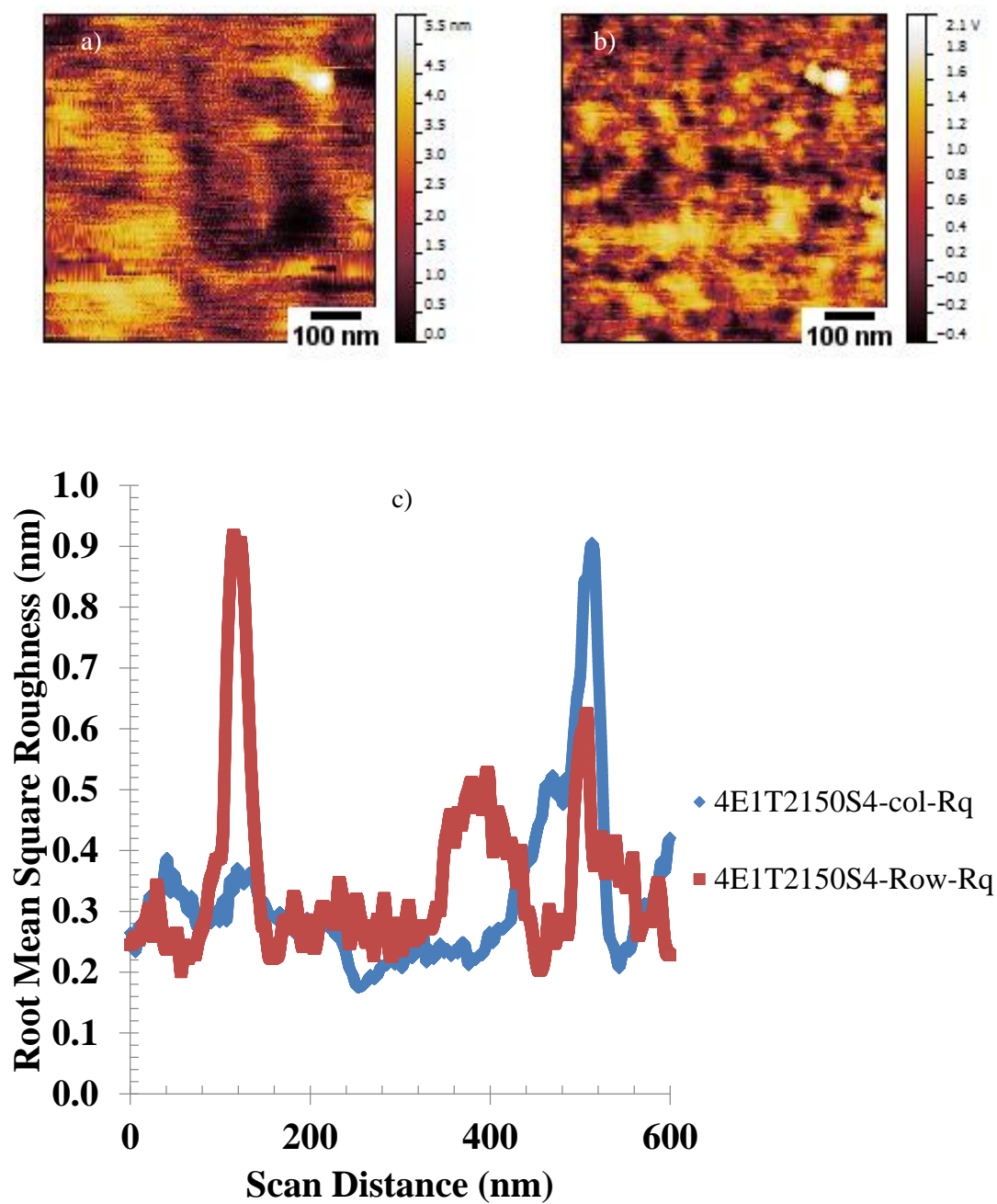


**Figure 79** a) Topographic and b) Phase images and c) RMS roughness's for a 4E1T2150S4 atomized DMAC film

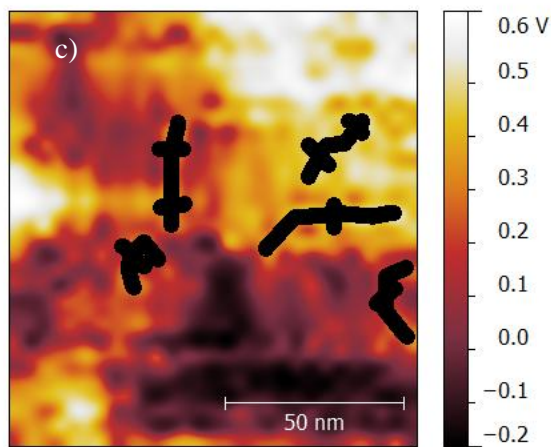
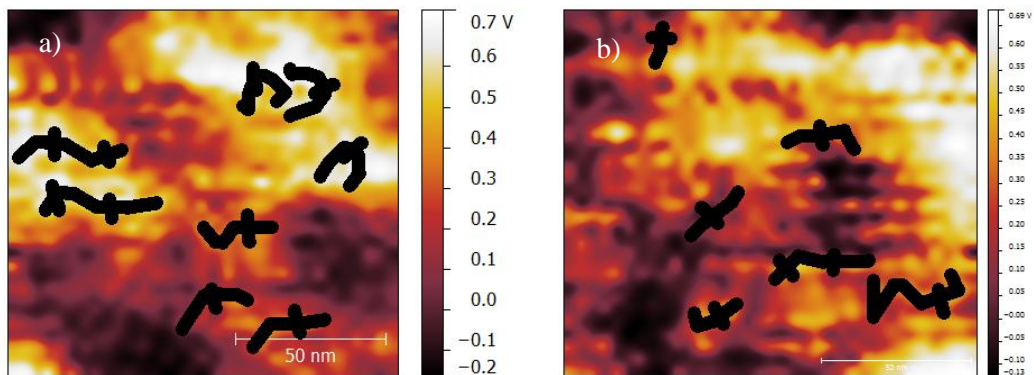


**Figure 80** a), b), c) are three sample images of selected regions within the phase image in Figure 79 b

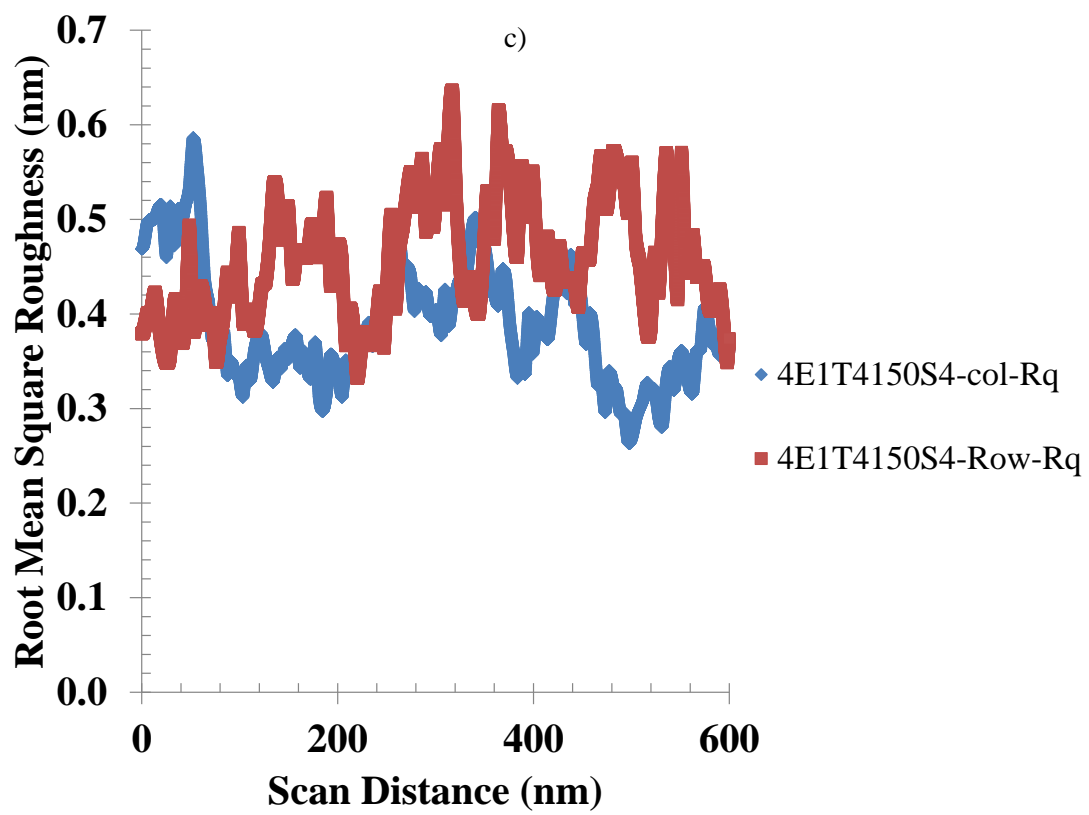
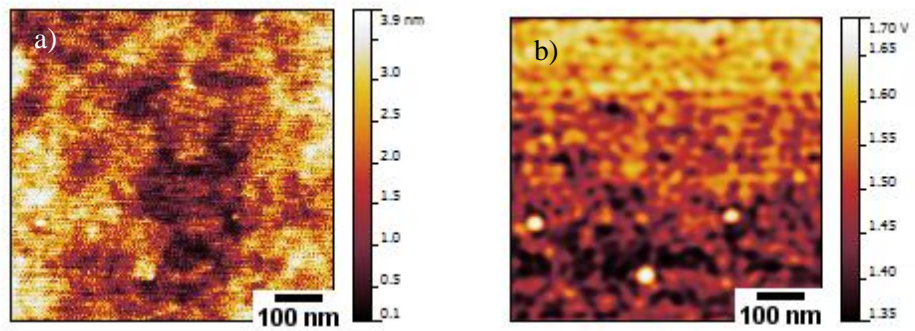


**Figure 81** a) Topographic and b) Phase images and c) RMS roughness's for a 4E1T4150S4 atomized DMAC film

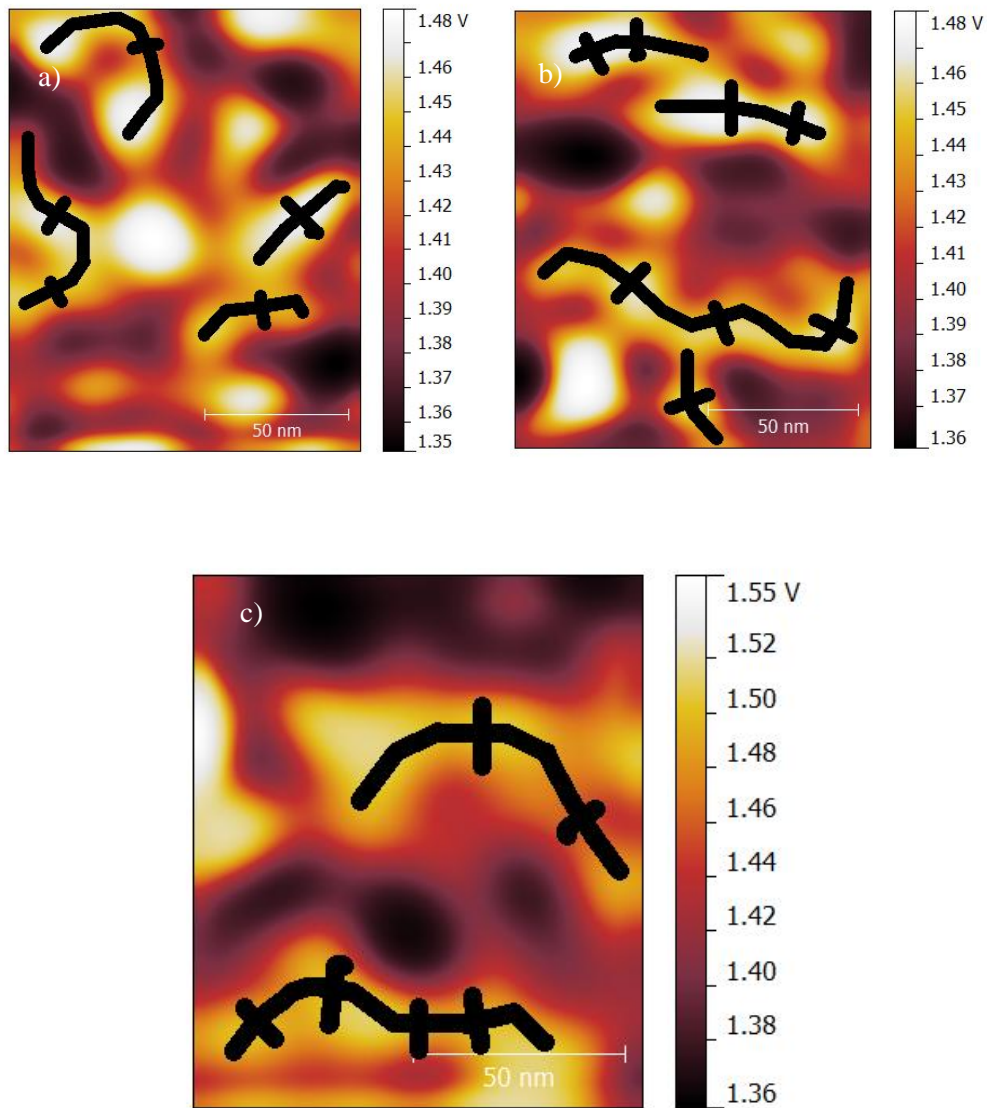


**Figure 82** a), b), c) are three sample images of selected regions within the phase image in Figure 81 b



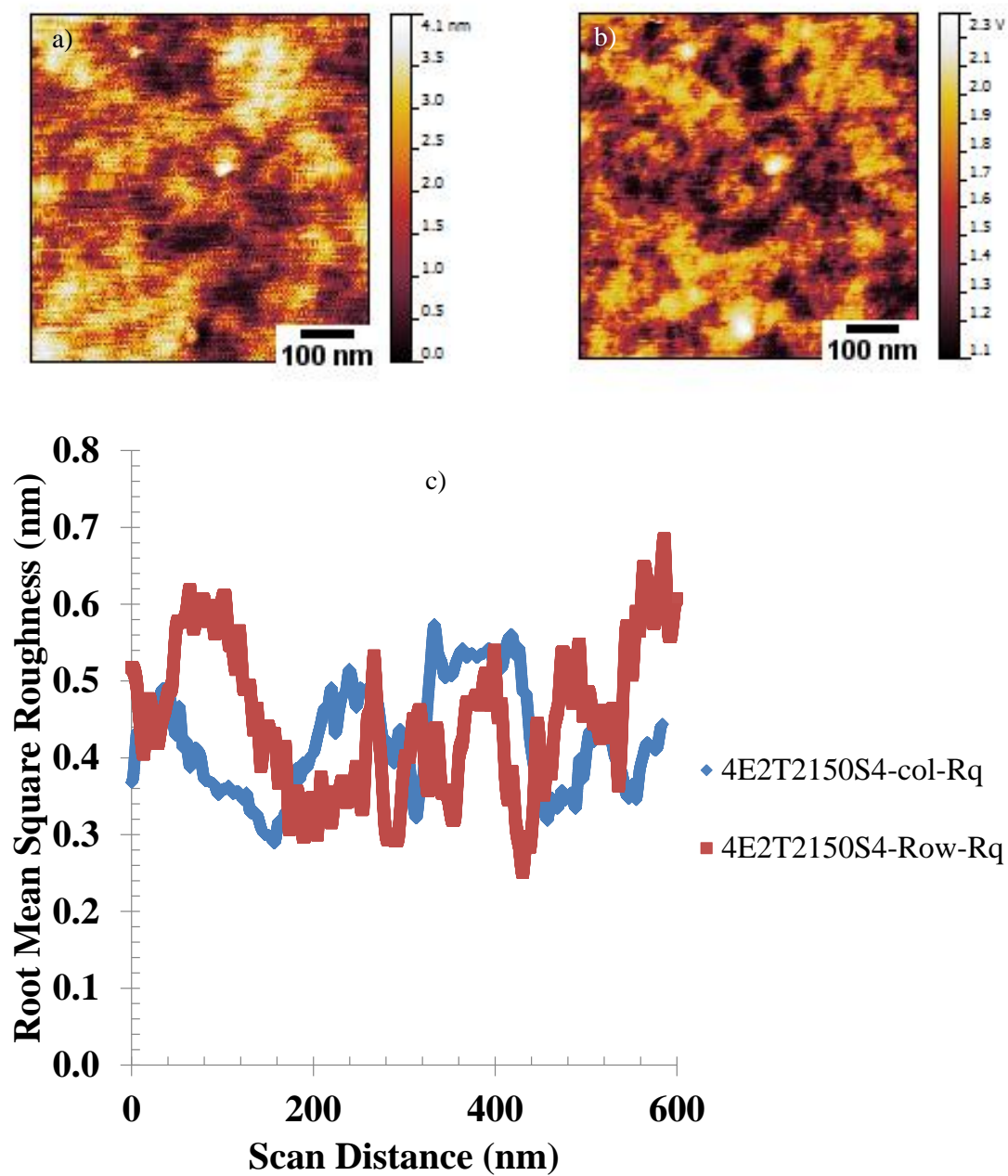


**Figure 83** a) Topographic and b) Phase images and c) RMS roughness's for a 4E2T2150S4 atomized DMAC film

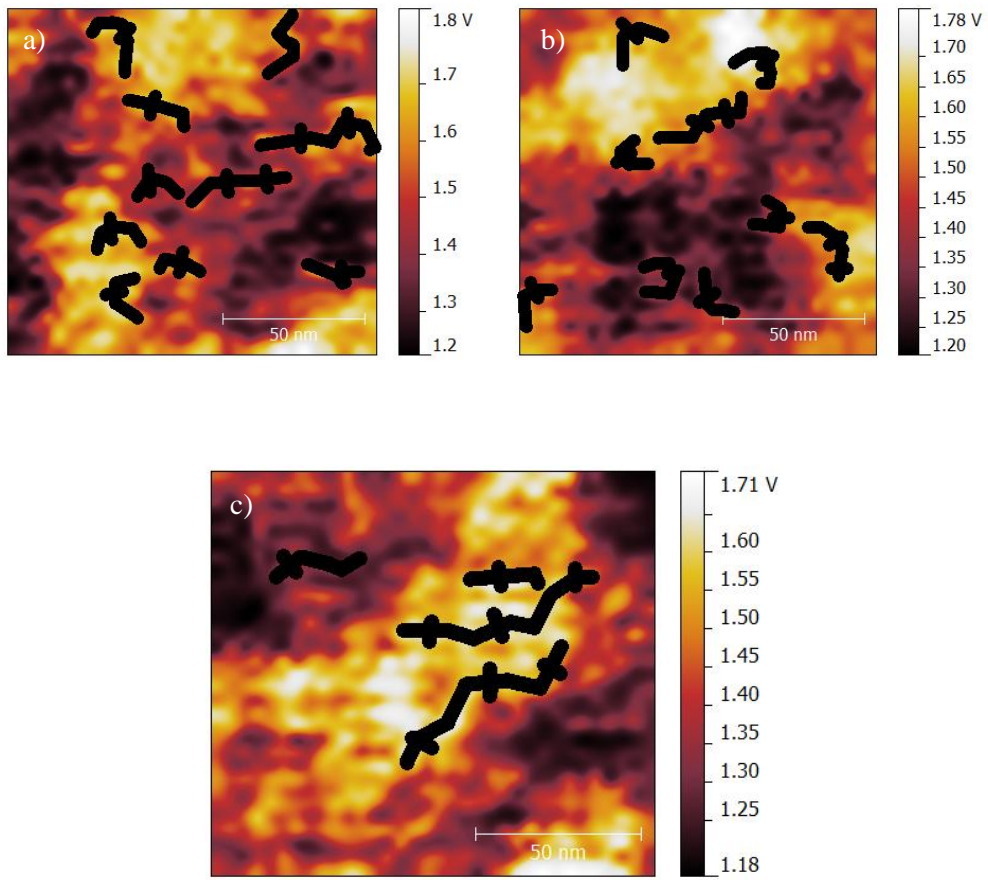


**Figure 84** a), b), c) are three sample images of selected regions within the phase image in Figure 83 b

**Table 11:** AFM Datasets for All Samples Fabricated in this Work

Process Condition	Phase Image Hard Domain Measurements
	Average Width (nm)
2% Control THF	12.5
2% 30 min THF	13.2
2% 60 min THF	11.1
2% 90 min THF	18.9
2% Control DMAC	7.1
2E1T2350S7 THF	12.8
2E1T250S11	8
2E1T2150S12	7.4
2E2T2150S10	9
2E3T2150S10	6.6
2E1T4150S11	7.3
4E1T2150S4	7.1
4E2T2150S4	6.5
4E1T4150S4	12.1

## Chapter 7.

### CONCLUSIONS

#### 7.1 Inferences

Here we map back to the research questions posed under sections 2.8 and 3.4 that each of the process parameters influence the microstructure and responses of the film in a subtle fashion. The degree of droplet coalescence is controlled significantly by the weight percentage of solution used. This together with the flow rate and temperature provides the process with a 'fine tuning' tool for controlling the film surface morphology. Further, the mechanical responses themselves are significantly influenced when a dilute 0.2% solution is used compared to 2% and 4% solutions. This happens because of extended annealing during UA assisted processing of the film itself (long times up to 2 days at 45 and 80°C). Our DSC data shows that this results in significant ordering in the material of the hard domains in the soft segment matrix. However, at the same time, the soft segment matrix has been unable to carry the load resulting in reduction of properties. A similar response is seen when the THF solvent is used to make atomized films. Here the matrix is much more phase mixed making it very soft resulting in premature failure. Thus, weight percentage, temperature and solvent are three critical parameters in this process.

Also, the effect of the capillary wave on the properties of these films is observed. Definitely for the 2% and 4% films as a function of energy, there are meager improvements in the strength, strains and toughness values. But this trend is not the same for 0.2% films. This is indicative of the capillary wave and its energy having more of an

influence when the viscosity of the solution is higher. Thus, capillary wave energy does have an influence but it is dependent on the viscosity of the solution used. While there is a possibility that some of the larger toughness values can be explained by phase mixing and break down of soft-segments, the degradation of the 0.2% film properties imply a degradation in the more significant hard segment molecular weight.

From the processing results in Chapter 4, we see that the air-draft controls the final droplet diameter and also provides for fabricating uniform films. There are also benefits with respect to energy and material usage. Further, there are no wide order of magnitude distributions in the final droplet diameter. For each case (wt% and flow rates), the droplet diameters all tend to one constant value between 50-100 $\mu\text{m}$ . This is again indicative of controlled coalescence with the aid of the draft. The air-draft attachment that is introduced to shape the sprays seemed to oscillate the sprays in different directions yielding uniform thin films of 20 $\mu\text{m}$  with the maximum standard deviation not exceeding 4 $\mu\text{m}$ . The air-draft also aided in the simultaneous drying of the spray droplets and provided some order to the random spray process. The degree of order was obvious with the uniform thicknesses that were obtained.

Without the air-draft attachment, a continual spray process was not feasible. Besides, the absence of the draft would obviously result in the flooding of the substrate. The physicochemical properties heavily influenced the spray process with surface tension increasing the median droplet diameter by about 50% relative to the 0.2% samples. Also evident was the fact that flow rate did not affect the final median droplet diameters of the 4% samples (due to the stabilizing nature of viscosity). It has also been shown that with decrease in the weight percents of solution, the process was exponentially longer.

Nevertheless, the repeatability of the process over time and across samples was evident from the uniformity in thickness and microstructure.

The DSC, SAXS and AFM data reveal that the microstructures of all these films have different degrees of phase mixing. There is evidence that this phase mixing is the most for the 4% sample and least for the 0.2% sample. Further, the DSC data again shows a solvent dependent trend where THF cast films show higher melting points (pseudo melting points due to ordering). The hard domain measurements from SAXS also show a trend where these values are higher for the 0.2% sample relative to the 4% samples. The AFM measured values match with these trends to that some extent, but reflect the heterogeneous nature of the microstructure (~10 nm). All of the topographical images suggest film surfaces were influenced definitely by i) increasing energies of atomization from 29%-46% of energy (decreased surface roughness from 3 nm to 2 nm for 2% films and 1 nm to 0.5 nm for 4% films) ; ii) increasing temperature of film fabrication from 45°C-80°C (increased roughness from 3nm to 4-5nm in local spots for 2% films and from 0.5nm to 0.6 nm for 4% films), iii) decreasing flow rate from 150 $\mu$ L/min to 50 $\mu$ L/min (comparable roughness for the case of the 2% films from 3nm to 2nm). These roughness evaluations could help explain our mechanical property results where increasing energies of atomization yield improvements whilst increasing temperature of film fabrication has yielded a decrease in mechanical properties.

## **7.2 Contributions**

An ultrasound based processing technology has been optimized for manufacturing thin thermoplastic polyurethane films. This has been done by incorporating UA onto the

traditional spin-coating platform making it a hybrid technology. The process results provide a basis for investigating other materials of engineering interest such as PVDF, nanoparticle based systems and even ceramics. The method itself is simple, robust, precise and easy to scale-up. The scale-up would involve the use of multiple atomizers in series or parallel with each other with discrete draft attachments for each case.

This process is also amenable to lithography type techniques providing flexibility for manufacturing for sensor/actuator type applications. Further, it has been shown conclusively that the process modifies the microstructure for certain cases of the independent variables. This provides for a route to obtain films/coatings of the desired microstructure and properties. As a matter of fact, the same set-up with slight modifications to the air draft pressures can also be used to manufacture nanoparticles and emulsions.

This work has also set-up a basis for modeling the droplet coalescence activity near and ahead of the nozzle tip. Fixed independent variables in these experiments and measured microstructures provide for a way to initiate comparisons to fluid mechanics based theory. That would go a long way in developing an understanding of the influence of ultrasound on viscoelastic sprays.

From a societal point of view, an advance in new manufacturing technologies such as the one dealt with in this dissertation will result in the development of new products and applications such as ultrasonic flossing/toothbrushes, soft polymer displays. All of these not only improve the overall health of the customers and their satisfaction but also the economy.

## 8. REFERENCES

- [1] Harsanyi, G. *Sensors in Biomedical Applications*. CRC Press LLC., Boca Raton, Florida, 1-33, 35-65, 65-96 (2000).
- [2] Harsanyi, G. Polymer Films in Sensor Applications. *Sensor Review* 20, 98-105 (2000).
- [3] Wang, J., Swain, M., G. Fabrication and Evaluation of Platinum/Diamond Composite Electrodes for Electrocatalysis: Preliminary Studies of the Oxygen-Reduction Reaction. *Journal of the Electrochemical Society* 150, E24-E32 (2003).
- [4] Chen, F.-C., Chu, C-W., He, J., Yang, Y., Lin, J-L. Organic Thin-Film Transistors with Nanocomposite Dielectric Gate Insulator. *Applied Physics Letters* 85, 3295-3297 (2004)
- [5] Sadaoka, Y., Sakai, Y., Xiaomei, W. Optical Properties of Fluorescent Dye-Doped Thin Film and it's Application to an Optochemical Sensor for Quantification of Atmospheric Humidity *Journal of Material Science* 29, 883-886 (1994).
- [6] de Gans, B.-J., Duineveld, P.C., Schubert, U. S. Inkjet Printing of Polymers: State of the Art and Future Developments. *Advanced Materials* 16, 204-213 (2004).
- [7] de Gans, B.-J. S., U. S. Inkjet Printing of Well-Defined Polymer Dots and Arrays. *Langmuir* 20, 7789-7793 (2004).
- [8] Krebs, C., F. Fabrication and Processing of Polymer solar Cells: A Review of Printing and Coating Techniques. *Solar Energy Materials and Solar Cells* 93, 394-412 (2009).
- [9] Krumdieck, S., Raj, R. Growth Rate and Morphology for Ceramic Films by Pulsed-MOCVD. *Surface and Coatings Technology* 141, 7-14 (2001).
- [10] Krumdieck, S., Raj, R. Conversion Efficiency of Alkoxide Precursor to Oxide Films Grown by an Ultrasonic-Assisted, Pulsed Liquid Injection, Metalorganic Chemical Vapor Deposition (Pulsed-CVD) Process. *Journal of American Ceramic Society* 82, 1605-1607 (1999).



- [11] Berger, H., L. Coating Drug-Eluting Arterial stents Using Ultrasonic Spray Nozzles. *ILASS Americas, 19th Annual Conference on Liquid Atomization and Spray Systems*, Toronto, Canada (2006).
- [12] Leiby, M., W. Chemical Vapor Deposition by Pulsed Ultrasonic Direct Injection of Liquid Precursors Produces Versatile Method for Creation of Thin film Circuits and Devices. *Application note, Sonotek Corporation* (2000).
- [13] Ye, Y., Jiang, Y., Wang, T., Wu, Z., Zeng, H. Ferroelectric Polymeric PVDF Films Prepared by Ultrasonic Atomization Method. *Journal of Materials Science: Electronic Materials* 17, 631-635 (2006).
- [14] Ye, Y., Jiang, Y., Wang, T., Yu, J., Wu, Z. Preparation and Characterization of Polymeric PVDF Films by Ultrasonic Atomization. *Integrated. Ferroelectrics*. 88, 27-32 (2007).
- [15] Ye, Y., Guo, T., L. Preparation and Characterization of Organic Ferroelectric Cathodes. *Integrated. Ferroelectrics*. 110, 108-114,(2009).
- [16] Ha, S., M., Yuan, W., Pei, Q., Pelrine, R., Stanford, S. Interpenetrating Networks of Elastomers Exhibiting 300% Electrically-Induced Area Strain. *Smart Materials and Structures* 16, S280-S307 (2007).
- [17] Pelrine, R., Sommer-Larsen, P., Kornbluh, R., Heydt, R., Kofod, G., Pei, Q., Gravesen, P. Applications of Dielectric Elastomer Actuators. *Proceedings of SPIE, Smart Structures and Materials 2001: Electroactive Polymer Actuators and Devices*, (Bar-Cohen, Y., Editor) 4329, 335-349 (2001).
- [18] Pelrine, R., Kornbluh, R., Eckerle, J., Jeuck, P., Oh, S., Pei, Q., Stanford, S. Dielectric Elastomers: Generator Mode Fundamentals and Applications. *Proceedings of SPIE, Smart Structures and Materials 2001: Electroactive Polymer Actuators and Devices*, (Bar-Cohen, Y., Editor) 4329, 149-156 (2001).
- [19] Carpi, F., De Rossi, D., Kornbluh, R., Pelrine, R., Sommer-Larsen, P. *Dielectric Elastomers as Electromechanical Transducers: Fundamentals, Materials, Devices, Models and Applications of an Emerging Electroactive Polymer Technology*, Elsevier, London, (2007).

- [20] Bar-Cohen, Y., Brezeal, C. Biologically Inspired Intelligent Robotics. *Optical Pattern Recognition* 5051, 14-20 (2003).
- [21] Wilbur, J., L., Jackman, R., J., Qhitesides, G., M., Cheung, E., L., Lee, L., K., Prentiss, M., G. Elastomeric Optics. *Chemistry of Materials* 8, 1380-1385 (1996).
- [22] Kawamura, K., Kano, T., Inoue, M., Matsuhita, Y., Kasahara, T., Fujita, M., Nakamura, S. A Facile Approach to the Fabrication of Ultrathin Polymr Films and Application to Optical Lenses. *Polymer* 51, 4562-4570 (2010).
- [23] Loh, K., J., Kim, J., Lynch, J., P., Kam, N., W., S., Kotov, N., A. Multifunctional Layer-by-Layer Carbon Nanotube-Polyelectrolyte Thin films For Strain and Corrosion Sensing. *Smart Materials and Structures* 16, 429-438 (2007).
- [24] Huang, H., Liu, C., Wu, Y., Fan, S. Aligned Carbon Nanotube Composite Films For Thermal Management *Advanced Materials* 17, 1652-1656 (2005).
- [25] Sohling, U., Jung, G., Saenger, D., U., Lu, S., Kutsch, B., Menning, M. Synthesis and Optical Properties of Mn<sup>2+</sup> -Doped ZnS Nanoparticles in Solutions and Coatings. *Journal of Sol-Gel Science and Technology* 13 (1998).
- [26] Saenger, D., U., Jung, G., Mennig, M. Optical and Structural Properties of Zns Nanoparticles Produced by a Sol-Gel Method. *Journal of Sol-Gel Science and Technology* 13, 635-639 (1998).
- [27] Guglielmi, M., Martucci, A., Menegazzo, E., Righini, G., C., Pelli, S., Fick, J., Vitrant, G. Control of Semiconductor Particle Size in Sol-Gel Thin Films *Journal of Sol-Gel Science and Technology* 8 (1997).
- [28] Grant, P., S., McShane, J., M. Development of Multilayer Fluorescent Thin Film Chemical Sensors Using Electrostatic Self-Assembly. *IEEE Sensors Journal* 3, 139-145 (2003).
- [29] Tipple, C., A., Lavrik, N., V., Culha, M., Headrick, J., Datskos, P., Sepaniak, M., J. Nanostructured Microcantilevers with Functionalized Cyclodextrin Receptor Phases: Self Assembled Monolayers and Vapor-Deposited Films *Analytical Chemistry* 74, 3118-3126 (2002).

- [30] Dimitrakopoulous, C., D., Mascaro D., J. Organic Thin Film Transistors: A Review of Recent Advances. *IBM Journal of Research and Development* 45, 11-27 (2001).
- [31] Liu, H. *Science and Engineering of Droplets*. Noyes Publications, Park Ridge, New Jersey, 19-119 (2000).
- [32] Jokanovic, V., Janackovic, D., Uskokovic, D. Size Distribution of Ultrafine Spherical Ceramic Powders Obtained by Ultrasonic Spray Pyrolysis. *Key Engineering Materials*, 132-136, 213-216 (1997).
- [33] Vivekchand, S., R., C., Cele, L., M., Deepak, F., L., Raju, A., R., Govindaraj, A. Carbon Nanotubes by Nebulized Spray Pyrolysis. *Chemical Physics Letters* 386, 313-318 (2004).
- [34] Ross, A., D., Gleason, K., K. The CVD of Nanocomposites Fabricated Via Ultrasonic Atomization. *Chemical Vapor Deposition* 12, 225-230 (2005).
- [35] Barba, A., D'Amore, M., Cascone, S., Lamberti, G., Titomanilo, G.,. Intensification of Biopolymeric Microparticles Production by Ultrasonic Assisted Atomization. *Chemical Engineering and Processing* 48, 1475-1481 (2009).
- [36] Kimoto, H., Ito, T., Hirose, T. Ultrasonic Atomization of some Polymer Solutions. *The Journal of the Acoustical Society of Japan* 34, 721-723 (1978).
- [37] Tsai, S., C., Luu, P. Ultrasound Modulated Two Fluid Atomization of Dilute Polymer Solutions. *Materials, Interfaces and Electrochemical Phenomena* 46, 1650-1661 (2000).
- [38] Gaikwad, S., G., Reddy, V., C., Pandit, A., B. Ultrasonic Atomization: A Novel Technique for Surface Coatings. *Surface Coatings International Part B: Coatings Transactions* 88, 189-197 (2005).
- [39] Berger, H., L. *Ultrasonic Liquid Atomization*. Partridge Hill Publishers, Partridge Hill, New York, 1-59, 99-103 (1998).

- [40] Ultrasonic Atomizers, Datasheet, *Sonics & Materials, Inc.* 53 Church Hill Road, Newtown, CT 06470-1614 USA.
- [41] Lord Rayleigh, On the Instability of Jets. *Proceedings of the London Mathematical Society*, 4-12 (1879).
- [42] Taylor, G., I. The Instability of Liquid Surfaces when Accelerated in a Direction Perpendicular to their Planes. I. *Proceedings of the Royal Society of London. Series A, Mathematical and Physical Sciences* 201, 192-196 (1950).
- [43] Lewis, D., J. The Instability of Liquid Surfaces when Accelerated in a Direction Perpendicular to their Planes. II. *Proceedings of the Royal Society of London. Series A, Mathematical and Physical Sciences* 202, 81-96 (1950).
- [44] Dombrowski, N., Fraser, R., P. A Photographic Investigation Into the Disintegration of Liquid Sheets. *Philosophical Transactions of the Royal Society of London. Series A, Mathematical and Physical Sciences*, 247, 101-130 (1954).
- [45] Antonevich. Ultrasonic Atomization of Liquids. *Battelle Memorial Institute* (1950).
- [46] Willard, G., W. Ultrasonically Induced Cavitation In Water: A step-by-Step Process. *The Journal of the Acoustical Society of America* 25, 669-686 (1953).
- [47] Lang, R., J. Ultrasonic Atomization of Liquids. *The Journal of the Acoustical Society of America* 34, 6-8 (1962).
- [48] Charles, G., E., Mason, S., G. The Coalescence of Liquid Drops with Flat Liquid/Liquid Interfaces. *Journal of Colloid Science* 15, 236-257 (1960).
- [49] Hinze, J., O. Fundamentals of the Hydrodynamic Mechanism of Splitting in Dispersion Processes. *A.I.ChE. Journal* 1, 289-295 (1955).
- [50] Peskin, R., L., Raco, R., J. *The Journal of the Acoustical Society of America* 35, 1378-1381 (1963).

- [51] Avaru, B., Patil, M., N., Gogate, P., R., Pandit, A., B. Ultrasonic atomization: Effect of Liquid Phase Properties. *Ultrasonics* 44, 146-158 (2006).
- [52] Rajan., R., Pandit., A., B. Correlations to Predict Droplet Size in Ultrasonic atomization. *Ultrasonics* 39, 235-255 (2001).
- [53] Petrovic, Z., S., Ferguson, J. Polyurethane Elastomers. *Progress in Polymer Science* 16, 695-836 (1991).
- [54] Cooper, S. L., Tobolsky, A. V. Properties of Linear Elastomeric Polyurethanes *Journal of Applied Polymer Science* 10, 1837-1844 (1966).
- [55] Clough, S., B., Schneider, N., S. Structural Studies on Urethane Elastomers. *Journal of Macromolecular Science, Part B* B2, 553-566 (1968).
- [56] Wilkes, C., E., Yusek, C., S. Investigation of Domain Structure in Urethan Elastomers by X-ray and Thermal Methods. *Journal of Macromolecular Science, Part B* B7, 157-175 (1973).
- [57] Koberstein., J., T., Russell., T., P. Simultaneous SAXS-DSC- Study of Multiple Endothermic Behavior in Polyether Based Polyurethane Block Copolymers. *Macromolecules* 19, 714-720 (1986).
- [58] Harrell, L., L., Jr. Segmented Polyurethans. Properties as a Function of Segment Size and Distribution. *Segmented Polyurethans* 2, 607-611 (1969).
- [59] Lee, S., H., Yoo, R., S., Seo, S., W. Domain and Segmental Deformation Behavior of Thermoplastic Elastomers Using Synchrotron SAXS and FTIR Methods. *Journal of Polymer Science: Part B: Polymer Physics* 37, 3233-3245 (1999).
- [60] Finnigan, B., Martin, D., Halley, P., Truss, R., Campbell, K. Morphology and Properties of Thermoplastic Polyurethane Nanocomposites Incorporating Hydrophilic Layered Silicates. *Polymer* 45, 2249-2260 (2004).

- [61] Bisticic, L., Leskovac, M., Baranovic, G., Blagojevic, S., L. Mechanical Properties and Linear Infrared Dichroism of Thin films of Polyurethane Nanocomposites. *Journal of Applied Polymer Science* 108, 791-803 (2007).
- [62] Tecoflex TPU Datasheet, *Lubrizol Thermedics Inc.*, 29400 Lakeland Boulevard Wickliffe, Ohio 44092.
- [63] Abramoff, M., D., Magalhaes, P., J., Ram, S., J. Image Processing with ImageJ. *Biophotonics International*, 11(7), 36-42 (2004).
- [64] Nečas, D., Klapetek, P. Gwyddion: An Open-Source Software for SPM Data Analysis, *Central European Journal of Physics*. 10(1), 181-188 (2012).
- [65] Balakrishnan, A., Saha, M., C. Processing and Characterization of Thermoplastic Polyurethane Nanocomposite Thin Films. *Journal of Engineering Materials Technology*, 133, 011012-1-011012-7, (2010).
- [66] Balakrishnan, A., Saha, M., C. Influence of air-Draft on Fabrication of Polyurethane Thin Films via Ultrasonic Atomization. *Atomization and Sprays*, 23-35, (2012).
- [67] Yaws, C., L., Narasimhan, P., K., Gabbula, C. *Yaws' Handbook of Antoine Coefficients for Vapor Pressure, 2nd ed. (Electronic Edition)*, Knovel, New York.
- [68] Balakrishnan, A., Saha, M., C. Effect of Ultrasound and Strain Rate on Tensile Mechanical Behavior of Thermoplastic Polyurethane Thin Films. *Journal of Engineering Materials Technology*, 133, 041008-1-041008-8, (2011).
- [69] Kazmierczak, M., E., Fornes, R., E., Buchanan, D., R., Gilbert, R., D., Investigations of a Series of PPDI based Polyurethane Block Copolymers. I. General Morphology. *Journal of Polymer Science: Part B: Polymer Physics*, 27, 2173-2187 (1989).
- [70] Christenson, E., M., Anderson, J., M., Hiltner, A., Baer, E. Relationship Between Nanoscale Deformation Processes And Elastic Behavior of Polyurethane Elastomers. *Polymer* 46, 11744-11754 (2005).

[71] Aneja, A., Wilkes, G.,L. A Systematic Series of 'Model' PTMO-Based Segmented Polyurethanes Reinvestigated Using Atomic Force Microscopy *Polymer* 44, 7221-7228 (2003).

[72] Furukawa, M., Kojio, K., Kugumiya, S., Uchiba, Y., Mitsui, Y. Microphase Separation of Bulk and Ultrathin Films of Polyurethane Elastomers. *Macromolecular Symposia* 267, 9-15 (2008).